March 2019

Design and Integration of a High-Powered Model Rocket – III

Connor Mcmahon Murphy
Worcester Polytechnic Institute

Jean Patrick Furter
Worcester Polytechnic Institute

Justin Tavares
Worcester Polytechnic Institute

Mason Douglas Handy
Worcester Polytechnic Institute

Nicholas Jordan Songer
Worcester Polytechnic Institute

See next page for additional authors

Follow this and additional works at: https://digitalcommons.wpi.edu/mqp-all

Author

Connor Mcmahon Murphy, Jean Patrick Furter, Justin Tavares, Mason Douglas Handy, Nicholas Jordan Songer, Nicolas Lucena Farias, Steffany Paige Halfrey, and Vanessa Ann Legere

JB3-1901

Design and Integration of a High-Powered Model Rocket - III

A Major Qualifying Project Report
Submitted to the Faculty of the
WORCESTER POLYTECHNIC INSTITUTE
in Partial Fulfillment of the Requirements for the
Degree of Bachelor of Science
in Aerospace Engineering

by

_____

Jean Furter

_____

Steffany Halfrey

_____

Mason Handy
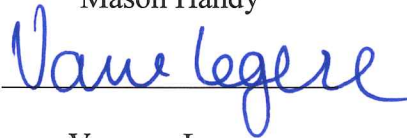
_____

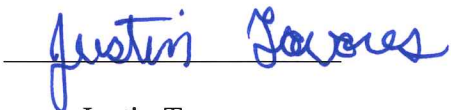Vanessa Legere

_____

Nicolas Lucena Farias

_____

Connor Murphy

_____

Nicholas Songer

_____

Justin Tavares

March 20, 2019

Approved by: _____
John J. Blandino, Advisor
Associate Professor, Aerospace Engineering Program
WPI

Approved by: _____
Jagannath Jayachandran, Co-Advisor
Assistant Professor, Aerospace Engineering Program
WPI

Abstract

The paper describes a project to design, assemble, and test propulsion, stage separation, and recovery systems for a high-powered model rocket. A first-principles model was used to evaluate the pressurization produced by the CO_2 separation system. A prototype system was fabricated and tested. Circuit and coil design for the electromagnetic booster separation system was used to minimize the capacitance, reducing vehicle mass. Results of this analysis are presented. Two models were used to evaluate rocket motor performance, one to estimate the thrust and specific impulse, and the other the heat transfer rates in the motor. Descriptions of these models are presented. Finally, an autorotation recovery system was designed based on turbine, helicopter blade, and blade element momentum theories.

Acknowledgements

We would like to thank the following individuals and groups for their help and support throughout the entirety of this project.

Table of Authorship

Section	Author
Abstract	SH
1.1.1 Overview of Model Rocket Systems - Propulsion	JT
1.1.2 Overview of Model Rocket Systems - Stage Separation	SH
1.1.3 Overview of Model Rocket Systems - Recovery	CM
1.2 HPR Program Goals	All three HPMR Teams: JB3-1901, NAG-1901 [1], and MAD-1901 [2]
1.3 HPMR Program Design Requirements, Constraints, Standards, and Other Considerations	
1.4 HPMR Program Management and Budget	
1.5 MQP Objectives and Methods	VL
1.6 MQP Tasks and Time Table	SH
2.1.1 Propulsion Background – Engine Clustering	JT
2.1.2 Propulsion Background – Ignitor System	VL
2.1.3 Propulsion Background – Static Motor Testing	MH
2.1.4 Propulsion Background – 0D Motor Modeling	MH, JT
2.1.5 Propulsion Background – Heat Flux Modeling and Simulations	JT
2.2.1 Propulsion Methodology – Engine Clustering	JT
2.2.2 Propulsion Methodology – Ignitor Systems	VL
2.2.3 Propulsion Methodology – 0D Motor Modeling	MH, JT
2.2.4 Propulsion Methodology – Heat Flux Modeling and Simulations	JT
2.3.1 Propulsion Results & Analysis – Ignitor Systems	VL
2.3.2 Propulsion Results & Analysis – 0D Motor Modeling	MH, JT
2.3.3 Propulsion Results & Analysis – Heat Flux Modeling and Simulations	JT
3.1.1 Stage Separation Background - CO_2 Stage Separation	SH
3.1.2 Stage Separation Background - Electromagnetic Separation	NLF
3.2.1 Stage Separation Methodology - CO_2 Stage Separation	SH, NS
3.2.2 Stage Separation Methodology - Electromagnetic Separation	NLF
3.3.1 Stage Separation Results & Analysis - CO_2 Stage Separation	SH, NS
3.3.2 Stage Separation Results & Analysis - Electromagnetic Separation	NLF
4.1 Autorotation Background	JF
4.2 Methodology	CM
4.2.1 Recovery Methodology - Autorotation	JF
4.2.2 Recovery Methodology - Autorotation Analysis	JF
4.2.3 Recovery Methodology – Parachute Analysis	CM
5.1 Summary	NS
5.2 Conclusions and Recommendations for Future Work	SH, NS, CM, JT, MH
5.3 Overall Project Broader Impacts	NS

Table of Contents

Table of Tables & Figures

Chapter 1: Introduction

Model rockets are identified as belonging to different levels: low power, medium power, Level-1, -2, and -3 based on the total impulse range of the motor(s), weight, materials, and other factors [3, 4]. Any rocket motor greater than Class-H, meaning it has a total impulse above 320 N-s, is classified by the National Association of Rocketry (NAR) or Tripoli Rocketry Association (TRA) as Level-1 or above. An individual must have a certification in Levels I-III to launch rockets of that specific size and impulse. The full classification of motors by impulse will be described in Section 1.1.1.

This Major Qualifying Project (MQP) team was part of the High-Powered Model Rocket (HPMR) Program consisting of two additional MQP teams. The goal of the Program was to design, integrate, and test fly a high-powered model rocket capable of reaching an altitude of 457.2 m (1500 ft). The rocket design and built for the HPMR is a Class-2, based on mass, with design options that included two Level-1 motor configurations.

The objectives of this MQP team were to: design, fabricate, and test the propulsion, staging, and recovery subsystems of the HPMR. The HPMR is shown in its final configuration in Figure 1.1.

Figure 1.1. SOLIDWORKS® rendering of the HPMR (left) and physical rocket (right) [1].

1.1 Overview of Model Rocket Systems

We performed a literature search to learn about the current practice of propulsion, stage separation, and recovery in HPMR. We also researched novel methods for each system that have been attempted or successfully completed by other universities and rocketry clubs.

1.1.1 Propulsion

Rocket propulsion systems utilize Newton's third law of motion which states that every action has an equal and opposite reaction. A typical model rocket propulsion system uses a motor to accelerate exhaust gas downward out of the tail end of the rocket. The accelerated gas produces a thrust force to accelerate the rocket upward. The motor is ignited at launch using an ignition system, and as the propellant burns inside the motor, the chemical reaction (combustion) produces hot gases that are accelerated through the nozzle. Model rocket motors use solid, liquid, and hybrid propellants [5]; however solid propellants are more commonly used. Propellants are made up of a fuel and an oxidizer, which react in a process called combustion. Most solid propellant motors use either black powder propellant or composite propellants. Black powder propellants have been used since the beginning of model rocketry. Black powder has a similar chemical formulation to gunpowder and is typically made from about 75% potassium nitrate, 10% sulfur, and 15% charcoal [6]. This propellant is still used in lower power motors today, while composite propellants are used in high-powered model rocket motors. Composite propellants are a homogenous solid mixture consisting of a fuel and an oxidizer mixed with a rubbery binder. A typical composite propellant consists of about 70% of an oxidizer such as ammonium perchlorate, 20% of a high-energy fuel such as aluminum, and 10% of binder such as HTPB (hydroxyl-terminated polybutadiene) [7]. Composite propellants are a more efficient fuel source because they provide more than three times the amount of thrust per unit of propellant mass compared to black powder propellants [5]. The larger thrust makes composite propellant motors a better choice for larger rockets designed to reach higher altitudes. Rocket motors are single use or reloadable. Reloadable motors require a casing and propellant kits to fill the casing with fuel. The initial cost for the casing is often high, but reloadable motors are more cost effective than single use motors after four to six uses due to the lower costs for propellant reload kits [8].

Most solid propellant rocket motors have the same general components whether they are single use or reloadable. The leads of the ignitor wires are located at the bottom end of the motor and are linked to the ignition system to fire the motor at launch [8]. The nozzle is also located at the bottom of the motor and allows exhaust gas to escape. The nozzle is shaped to accelerate the mass flow of the burned gas to supersonic speeds to provide maximum thrust. The solid propellant grain, which burns to produce the heated gas, is located upstream of the nozzle; the grain is shaped in various ways to provide different burning characteristics and thrust levels during the motor's burn time. Above the propellant grain is the time delay grain as shown in Figure 1.2; the time delay grain is a section of low-energy solid mixture that when ignited, produces no gas or thrust. The time delay allows the rocket to continue traveling after it has achieved its maximum acceleration, prior to ignition of the ejection charge. The ejection charge, typically a pyrotechnic charge, is located at the motor's forward end as shown in Figure 1.2. The ejection charge produces hot gas and particles that pressurize the inside of the model rocket's airframe, eject and jettison
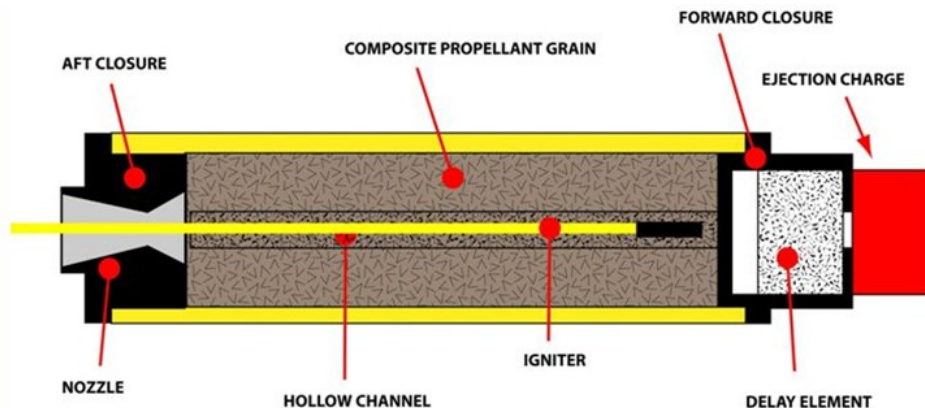
Figure 1.2. Reloadable composite rocket motor diagram [9]. Copyright © 2009 Tom Sarradet.

the nosecone of the rocket and push the recovery device out of the airframe. Reloadable motors have additional components to allow for multiple uses. In addition to the casing, reloadable motors have forward and aft closures that keep the hot gas from escaping the motor casing; this ensures that the gas exits through the nozzle. As shown in Figure 1.2, the aft closure is located at the bottom

of the motor to secure the nozzle piece to the motor casing; the aft closure has a hole that is manufactured to allow the nozzle piece to protrude out of the bottom while still sealing the hot gas in the motor casing. The aft closure has a larger diameter than the casing, which serves as an engine block when inserted into the motor tube [8]. The forward closure, as shown in Figure 1.2, is located at the top of the motor and holds the prepackaged delay module and ejection module.

Rocket motors available for model rocketry are limited to commercially produced motors that are certified by the Standards and Testing Committee of the NAR (National Association of Rocketry). For a motor to become "certified", it must pass strict performance and reliability standards developed by the NAR and the NFPA (National Fire Protection Association) [3]. To assess if a motor follows these standards, extensive testing must be done by one of the three major rocketry associations in the United States: the NAR, the TRA (Tripoli Rocketry Association), or the CAR (Canadian Association of Rocketry) [5]. Testing ensures that motors are not only safe for hobby use, but also deliver the performance, including thrust and impulse, specified by the manufacturer to within a specified tolerance. Motor testing results and uncertainties, as well as official motor statistics and thrust curve data points, can be found through each association's respective testing committee website [10].
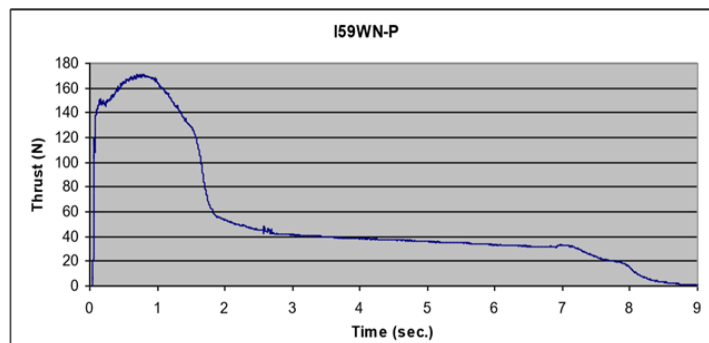
Figure 1.3. Thrust curve of I59WN-P Aerotech motor [11]. Copyright © 2009 NAR Standards and Testing.

Manufacturers provide many motor performance statistics for all commercially available motors. These parameters include total impulse, maximum thrust, average thrust, burn time, delay time, motor diameter and length, and total and propellant mass [8]. In addition, unique thrust

curves are published for each motor that specify the thrust at any moment during the burn time. Figure 1.3 shows an example of a typical thrust curve that was published by the NAR motor testing committee.

The total impulse is calculated from the thrust curve using Eq. (1-1), where I is total impulse, F is thrust, and t is time.

$$I = \int F dt \tag{1-1}$$

To summarize these motor statistics, the NAR motor code was developed to identify any motor and categorize motors based on impulse class. An example of a motor code is "I59WN-P." The first letter in the NAR motor code refers to the total impulse delivered by the motor [5]. A motor, as seen in Table 1.1, equal to or greater than the Class-H impulse range requires a specified user certification of Level-1 or above by the NAR or TRA to be purchased and used. Furthermore, high-power model rocketeers are required by the NAR to have a Level-1 certification to use motors with a high enough total impulse [5]. The first number in the NAR motor code tells you the average thrust in Newtons. This number is found by dividing the total impulse by the burn time. Average thrust is a useful piece of information for altitude prediction. The number that follows the dash in the code is the delay time in seconds, which is the time it takes after burnout before the ejection charge is ignited and deploys the recovery device [5]. Some motors do not have ejection charges and are used with and alternative recovery methods or as lower stage booster motors [8]. These motors are considered a dash-zero type; therefore, the motor code will end with a zero or will not include any number for delay time. Finally, the second letter, which could come before or after the dash, denotes the propellant type. The letters are often unique to specify a propellant used by a certain motor manufacturer, but there are cases where the same letter denotes a different propellant depending on the motor manufacturer. The propellant type does not affect motor performance and is mostly used to specify the rocket exhaust tail color at launch [8].

The motor mount is the part of the rocket that is used to integrate the motor within the body tube of the rocket. The motor mount is used to hold the motor firmly in place so that it cannot move under high amounts of thrust [5]. In addition, the motor mount holds the motor straight so

that it is aligned with the center axis of the rocket's airframe. The motor mount usually consists of the motor body tube and centering rings. The motor body tube holds the motor with a slip fit, meaning the diameter of the body tube is slightly larger than the diameter of the motor to allow for minimal assembly friction. The centering rings center the motor body tube into the center of the

Table 1.1. Rocket motor impulse classification [12]. Copyright © 2018 Rocketry SA.

Class	Total Impulse Limit (N-s)	Category	
1/8A	0.3125	Model Rocketry	
1/4A	0.625		
1/2A	1.25		
A	2.5		
B	5		
C	10		
D	20		
E	40		
F	80		
G	160		
H	320	Rocketry	L1
I	640		
J	1280		L2
K	2560		
L	5120		
M	10240	HPR	L3
N	20480		
O	40960		

airframe. The centering rings have an outer diameter equal to the inner airframe of the rocket and an inner radius corresponding to the diameter of the motor body tube. For high-power model rockets, the centering rings are usually made of laser-cut plywood for a precise cut and sturdy fit within the airframe [8]. The motor mount also needs a form of motor retention to ensure that the motor does not move within the motor body tube. This is often accomplished using a motor retaining clip/hook in more basic models, which fits in between the motor body tube and the centering rings [5]. This prevents the motor from falling out of the motor body tube during assembly and following motor burnout when it is not accelerating upward. To prevent the motor from flying up into the rocket during deceleration of the vehicle after the propellant is consumed,

as well as during stage separation, a thrust ring is often glued to the forward end of the motor. The thrust ring has a hole through its center to allow for the ejection charge gas to pass. A thrust ring is often not necessary for reloadable motors as the diameter of the aft closure of the motor casing is greater than the diameter of the body tube and thus serves as the engine block. Figure 1.4 shows an example of a conventional motor mount.
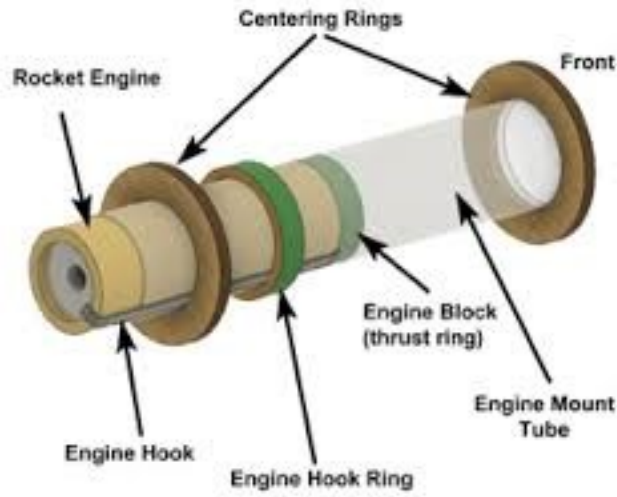
Figure 1.4. Motor mount diagram [13]. Copyright © 2018 Apogee Components.

1.1.2 Stage Separation

Flying a multi-stage model rocket, as discussed by Stine in *The Handbook of Model Rocketry* [5], is commonly referred to as "multi-staging" and refers to use of a rocket which has two or more motors that are used in sequence, with some of them jettisoned from the vehicle, along with any associated airframe components, following motor burnout. A model rocket with multiple stages allows for a lower total vehicle weight during the final burn period by discarding unneeded or dead weight. The performance of the rocket is enhanced through the loss of weight, because the burnout velocity of the rocket is increased compared to a single-stage rocket. Multi-staging also provides a higher total impulse for a rocket using multiple motors.

Stage separation is performed in two forms, series and parallel staging. In series staging two motors are stacked on top of each other and held together with tape. A similar motor would be used to that in Figure 1.2; two motors like those pictured would be stacked on top of each other except that the booster motor would not have a delay element or ejection charge. Stine [5] describes how, in series staging, the lower portion of the rocket, referred to as the "booster" or "booster stage", operates until booster motor burnout thus accelerating the entire rocket body. Hot gases and particles are produced during the operation of the booster. As the propellant burns in the booster motor, a layer of propellant remains at the top of the motor which allows the rocket body to build up internal pressure. These gases and particles break through the remaining propellant in the booster motor as it reaches burnout, and then travel upwards into the second motor's nozzle. The second motor in the upper stage airframe, the "sustainer motor", is then ignited by the hot particles and gases allowing the upper stage to propel the rocket so that it can continue accelerating upwards. The booster stage is then released from the model rocket in a stage separation event, imparting its total impulse to the upper stage of the rocket. The imparted impulse adds to the impulse of the sustainer motor and allows the upper stage to have a larger burnout velocity than if it were a single-stage motor only. Because the apogee, or peak altitude, of the upper stage will vary as the square of the burnout velocity, significant increases in altitude can be achieved by using multiple stages. Stage separation should occur when the model rocket has reached maximum velocity using the booster motor rather than maximum altitude. Neglecting aerodynamic forces, a model rocket series-staged at the booster's peak velocity will go twice as high as if staged at the booster's maximum altitude. In series separation, in-flight motor starts can pose a risk as a motor that does not function as planned can be a safety hazard. If the sustainer motor does not ignite, the ejection method may function at the incorrect time or not at all and the stage may enter free fall.

When utilizing series staging, motors can touch directly or have a small gap between them. Small venting holes, about a quarter inch in diameter, as seen in Figure 1.5, must be made on opposite sides of the rocket body just below the nozzle of the sustainer motor for series staging to be successful. The air between the two motors is ambient. If no venting holes are present, as the hot air and propellant particles from the booster motor rise, they will be blocked by the cooler air and not ignite the sustainer motor. The vent holes allow the cooler air to exit the core of the model rocket core, and the hot gases to reach the sustainer motor. In larger diameter rockets, vent holes also need to be added to the motor mount to prevent premature separation

Small ports
below the nozzle
of the sustainer
motor

Hot gases and
particles flow
upward
following
booster motor
burnout
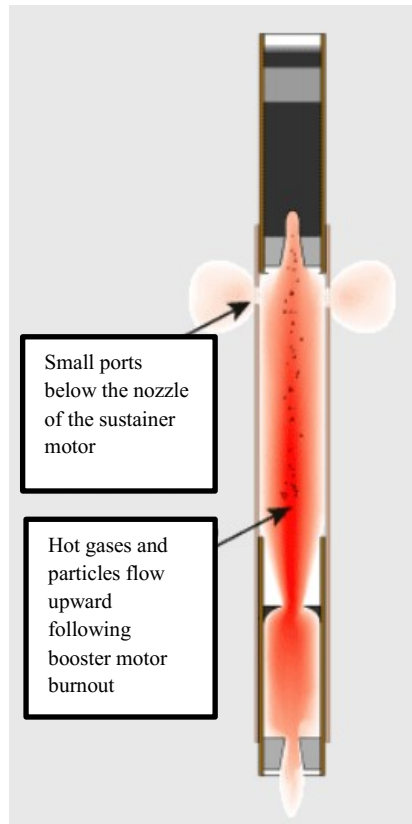
Figure 1.5. Gap staging [14]. Copyright © 2018 Apogee Components.

In parallel staging, as Stine also details [5], at launch the booster and sustainer motors begin operating. The motor(s) inside the rocket during parallel staging are often referred to as "core motors" and are similar to sustainer motors for series staging. This is because these motors are located at the center of the configuration of the rocket and typically have a delay element and ejection charge for the configuration of parallel staging. The booster stages consist of external airframes attached to the main rocket airframe which contain booster motors that are smaller than the core motor(s). The external booster motors are selected to have a shorter burn time than the core motors to allow the core motor to continue burning after separation. The booster motors are jettisoned from the main rocket airframe after burnout. After separation, the core motor continues to operate thus accelerating the main vehicle upwards. Parallel staging enables a higher thrust at takeoff due to the ignition of multiple motors but igniting multiple motors simultaneously can be challenging and pose a risk to proper flight.

Staging can also be categorized as "indirect" and "direct" as detailed in Van Milligan's [14] article about multistage model rockets. Indirect staging of the second stage means that a signal produced by an onboard device will trigger the separation event. Indirect staging is used for anything other than the ignition of a second black powder propellant motor, such as a composite motor or a triggered mechanical separation system event. Indirect staging is necessary for parallel-staged rockets as the booster and core motors do not touch and are not in-line with each other vertically. Direct staging refers to when the hot gases and particles from the booster motor(s) ignite the sustainer motor following burnout. Direct staging can occur when the booster and sustainer motor are stacked directly on-top of each other as in series staging, or with a small gap in between the motors. Direct staging occurs based on the same principles of the flow of hot gas as described previously for series staging whether the motors are touching or gapped.

Both parallel and series staging can be implemented on a single vehicle, as well as direct and indirect staging. It is unsafe to launch multistage model rockets in windy conditions as they turn easily into the wind (weathercocking). For this reason, model rockets should not be built to have more than three stages due to the high risk of weathercocking in even a slight breeze, which results in higher rates of failure and decreased safety for bystanders.

An "ejection system" is a type of separation discussed by Stine and the Huntsville Area Rocketry Association (HARA) [14, 15], that must be used for a model rocket to deploy the recovery device or any internal payloads. Ejection is executed using ejection charges within commercially purchased motors or through custom methods. A common method is using pyrotechnic charges, such as black powder, to eject your recovery system. A black powder ejection charge is usually contained within commercially purchased motors. The motors ignite the black powder charge(s) following the designated time delay for the motor after burnout. The hot gas and particles fill the model rocket's body tube, of volume V, resulting in a buildup of pressure that exerts a force F on the bulkhead end of the nosecone, of area A, which causes it to pop off. The force of the pressurized gas is determined by the relationship between force, area, and pressure as described by Eq. (1-2). The Ideal Gas Law, Eq. (1-3) is then applied to find the mass of black powder, n, needed to reach that pressure. Various model rocketry organizations have created online calculators utilizing these equations to aid in ejection calculations.

$$P = \frac{F}{A} \tag{1-2}$$

$$n = \frac{PV}{RT} \tag{1-3}$$

The force necessary to separate a four-inch diameter bulkhead, as reported by HARA, is 444.8 N to 889.6 N (100 lb. to 200 lb.), which equates to a required pressure of 55. 16 kPA to 110.32 kPa (8 psia to 16 psia).
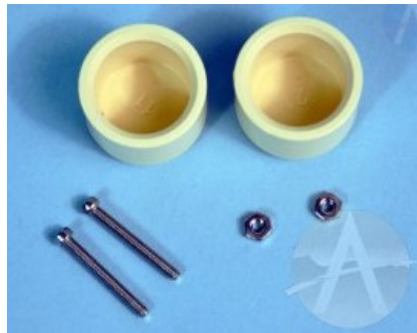
Figure 1.6. Ejection PVC canister caps [16]. Copyright © 2018 Apogee Components.

Figure 1.7. Ejection PVC canister caps and plastic charge wells [17]. Copyright © 2018 Pratt Hobbies.

Multiple materials can be utilized to hold black powder charges including a PVC or plastic charge well which can be commercially purchased, the corner of a plastic sandwich bag, or rolled blue masking tape as seen in Figure 1.6 and 1.7.

1.1.3 Recovery

Recovery methods have remained relatively unchanged since the 1950s and 60s when hobby rocketeers began using rockets for recreation [5]. Multiple groups around that time began using deployable parachutes. In 1946, scientists and engineers began to separate the nosecones from within German V-2 missiles to keep them from breaking apart on impact. The nosecones had parachutes that deployed following separation. The trend towards deployed parachutes not only occurred within the model rocketry field, but within rocketry. It was not until the 1980s that NASA and other contractors developed the Space Shuttle, a revolution in reusable space systems. However, since the space shuttle era there has been relatively little innovation in rocketry, until the emergence of SpaceX in 2008 [18].

Parachute recovery is the oldest and most reliable of the recovery methods. Deployable parachutes were first used as a recovery method for model rockets in 1954 [5]. The recovery parachute can also be used in addition to the nose-blow method, when the nosecone is attached with a shock cord, resulting in the slowest descent speeds out of all the recovery methods. Model rocket parachutes are commonly made from polyethylene plastic sheet or film ranging from 0.00025 in to 0.001 in in thickness [5]. Drogue and spherical parachutes are the most common type of recovery parachute used in model rocketry. A drogue parachute is designed for rocket sections with smaller masses, the nosecone is an example of a small rocket section, to allow for faster descent velocities of about 22 m/s [19]. Drogue parachutes are also designed to deploy before a main parachute to lower the descent velocity and stabilize the rocket. In some cases, the drogue parachute is used to pull the main parachute out of the tube. Equation (1-4), used to determine the diameter of a drogue parachute, is found by equating the vertical cross-sectional area of a model rocket body, a rectangle, to the horizontal cross-sectional area of the same model rocket body, a circle. This formula is not specific to drogue parachutes, it can be used to find the diameter of different shape and sizes of parachutes. The equation is as follows:

$$D = \sqrt{\frac{4dL}{\pi}} \qquad\qquad (1\text{-}4)$$

Where D is the calculated diameter of the drogue parachute, L is the length the rocket, and d is the diameter of the rocket. The calculation of the diameter of a drogue parachute depends on the section of the rocket that needs to be recovered. For example, a nosecone with a diameter of 3 in and length of 10 in requires a 6.18 in diameter drogue parachute. A parachute designed for heavier, more fragile rockets is referred to as a spherical parachute as opposed to the smaller drogue parachute mentioned previously. The desired descent velocities of spherical parachutes are between 4 m/s to 6 m/s [20]. Equation (1-5) is used to determine the area of a round parachute to use for a rocket.

$$S = \frac{2gm}{\rho C_d V^2} \qquad\qquad (1\text{-}5)$$

Where S is the calculated (projected) area of the parachute, g is the acceleration due to gravity, m is the mass of the descending rocket, ρ is the air density, C_d is the coefficient of drag, and V is the descent velocity. The descent velocity V is chosen by the user, as mentioned above, based on the desired ground-hit velocity for the rocket, rocket section, or payload. The calculated, projected circular surface area is used to find the diameter of the spherical chute, using the following equation for the area of a circle:

$$D = \sqrt{\frac{4S}{\pi}} \qquad\qquad (1\text{-}6)$$

23

In this equation, D is the diameter of the spherical parachute and S is the previously calculated projected surface area. As an example, the area of a round parachute S, for a rocket with a mass of 1 kg, a chosen descent velocity of 4.5 m/s, and g, C_d, and ρ values of 9.81 m/s^2, 0.75, and 1.225 kg/m^3 respectively, is 1.05 m^2. With this value of S, to find the diameter of the spherical parachute, D, results in 1.15 m.

1.2 HPMR Program Goals

The goals of the HPRM Program were shared among the three MQP teams involved (NAG-1901 [1], JDB-1901 (this report), MAD-1901 [2]). They are:

- Design, integrate, and fly a reusable, Class-2 high-powered model rocket capable of reaching an altitude of 457.2 m (1500 ft) using Level -1 motors.
- Provide the 21 members of the three MQP teams with a major design experience of a moderately complex aerospace system.

1.3 HPMR Program Design Requirements, Constrains, Standards and Other Considerations

The *design requirements* for the HPMR Program were shared among the three MQP teams involved (NAG-1901 [1], JDB-1901, MAD-1901 [2]) and consisted of the following:

- Use on-board cameras to record video during flight.
- Use an autorotation recovery system to slow the descent and prevent damage upon impact.
- Use a CO_2 stage-separation system to eject the nosecone and deploy the recovery system.
- Use an electromagnetic stage separation system to separate boosters from the main rocket body.
- Use actively-controlled, actuated fins to control the trajectory of the rocket to insure vertical flight.
- Use single or clustered, Level-1 main motors, and boosters if necessary, to provide the necessary thrust-to-weight for a safe launch, while remaining below the total impulse limit.

The *design constraints* for the HPMR Program were shared among the three MQP teams and consisted of the following:

- The overall weight of the rocket must be minimized to ensure a high enough thrust-to-weight ratio to launch safely and meet project height requirements.

- The rocket must leave the launch rail at a high enough speed to ensure there is no chance of injury to those present at the launch site.

- Each motor must be able to individually provide a 5:1 thrust to weight ratio off the launch rail to provide an adequate safety factor.

- The dimensions and location of all internal subsystems must be compatible with constraints imposed by the height and width of the rocket body.

The *design standards* imposed by the National Association of Rocketry (NAR) [3] for high-powered model rockets applied to the three MQP teams and included the following:

- The rocket is built with lightweight materials (paper, wood, rubber, plastic, fiberglass, or when necessary ductile metal).

- Only certified, commercially made rocket motors are used to launch the rocket.

- Motors and rocket body materials used were purchased from reputable hobbyist sources.

- For flight tests, the motors are ignited electronically with commercial ignitors, purchased from reputable hobbyist sources.

- The rocket is launched with an electrical launch system, and with electrical motor igniters that are installed in the motor only after the rocket is at the launch pad or in a designated prepping area. The launch system includes a safety interlock that is in series with the launch switch that is not installed until the rocket is ready for launch and will use a launch switch that returns to the "off" position when released. The function of onboard energetics and firing circuits will be inhibited except when the rocket is in the launching position. The switch is installed and tested before launch.

- The rocket uses a recovery system to land the rocket safely and undamaged in such a manner that it can be flown again. Any wadding used in the recovery system is flame-retardant. For the test launch, this consisted of an appropriately sized parachute. An autorotation recovery system was designed for later launches.

The following *design considerations* for the HPMR Program were shared among the three MQP teams and included the following:

- Safety: A primary consideration during construction, integration, and launch, for both the MQP teams and the public.
    - Simulation of possible landing places to insure the safety of not only the project teams, but also the launch site.
    - Thrust-to-weight ratio: Designed to be relatively high, to insure safe levels and guarantee the rocket maintained a vertical orientation after leaving launch rail.
    - Proper disposal of partially burned motors to insure safety and minimize environmental impact.
- Social impact: The broader impacts of model rocketry as a hobby was researched by the individual teams with findings described in the individual reports.
- Environmental factors: Means of limiting potential environmental impact of model rocketry (e.g. material disposal, damage during launch and flight mishaps) was researched by the individual teams with findings described in the individual reports.
- Community outreach: considered to potentially engage those wishing to learn more about STEM related topics explored with this project.

1.4 HPMR Program Management and Budget

The HPMR Program consisted of three separate MQP teams, each responsible for different aspects of the Program.

The Mechanical, Structural, Aerodynamic, and Thermal (MSAT) MQP team (NAG-1901 [1]), with 8 members, was responsible for the physical assembly and mechanical integration of all subsystems designed by the other teams. The MSAT MQP had the responsibility of ensuring all other teams were aware of the spatial limitations inside the rocket that would affect their subsystem designs. The MSAT MQP also performed structural, aerodynamic, and thermal analysis on the various subsystems inside the HPMR to make sure everything worked cohesively, and to confirm that nothing would be damaged during a launch.

The Propulsion, Staging, and Recovery (PSR) MQP team (this report: JB3-1901), with 8 members, was responsible for the design of the propulsion, staging, and recovery subsystems of the HPMR. The PSR MQP team performed analysis on motor sizing to choose the appropriate motors for the rocket and determined a parachute size that would return the rocket to the ground

at a safe velocity. An autorotation recovery subsystem was also designed, which was meant to replace the parachute. The PSR MQP team also designed the systems that would separate the nosecone section from the rocket body (black-powder and eventually CO_2) and the system that attaches/separates the boosters from the main body via electromagnets.

The Flight, Dynamics, and Control (FDC) MQP team (MAD-1901 [2]), with 5 members, was responsible for the design of the avionics for control and dynamic stability of the HPMR. For the first launch the FDC MQP team had to ensure parachute ejection at apogee as well as dynamic stability of fin design. While communicating with MSAT they were given maximum electronics bay dimensions to ensure sufficient volume for parachute and motors.

The three MQP teams met weekly with each of the faculty advisors involved as a conglomerate organization titled the Systems Engineering Group (SEG). Each week, the MQP teams presented an update of the past week's activities, discussed open action items between the teams, and sought input from the faculty advisors.

Funding for the construction of the rocket was provided by the WPI Aerospace Engineering Department. Per school policy, each student was allotted $250 for use in the project. With 21 students, the budget for the construction of the rocket totaled $5250. The total funds were split between the three MQP teams comprising the HPMR Program. The MSAT and PSR teams each had 8 members, corresponding to a budget of $2000 each. The Controls team received the remaining funds for its 5 members, with $1250. Overall, the SEG spent $1,947.94 in development of the rocket. The full cost breakdown can be seen in Appendix B.

The Code of Ethics for Engineers (National Society of Professional Engineers) states that "Engineers, in the fulfillment of their professional duties, shall:

1. Hold paramount the safety, health, and welfare of the public.
2. Perform services only in areas of their competence.
3. Issue public statements only in an objective and truthful manner.
4. Act for each employer or client as faithful agents or trustees.
5. Avoid deceptive acts.
6. Conduct themselves honorably, responsibly, ethically, and lawfully so as to enhance the honor, reputation, and usefulness of the profession."

The first canon is especially relevant to this project, since model rocketry can be a dangerous hobby if certain regulations are not strictly followed. The HPRM Program took this canon very seriously, by adhering to all FAA and NAR guidelines and regulations throughout the design process, as well as by following all guidelines set forth by the executive staff at the launch site.

The second canon was addressed partially by placing students in each MQP team that they would be most interested and qualified for, thus creating a project wherein students are performing work in their area of expertise.

The third and fourth canons are less relevant to the HPMR Program, since there were no public statements to be issued; nor were there separate employers to speak of.

The fifth and sixth canons are covered by WPI's Academic Honesty Policy, which all three MQP teams (and all MQPs) must follow.

1.5 MQP Objectives and Methods

Objectives of the MQP

1. Analyze and perform top-level design of a propulsion system for a Class-1 rocket
   - Evaluate arguments for and against core motor clustering
   - Estimate the thrust/impulse generated by off-the-shelf rocket motors using a reduced order, steady state combustor model
   - Estimate the heat transfer rates from the burning propellant grain to the rocket body
2. Design, build, and test a pressurized carbon dioxide stage separation system
   - Simulate the operation of the carbon dioxide pressurization system using a transient flow model
   - Design a cost-effective, reliable, and reusable system for carbon dioxide stage separation
3. Design, build, and test an electromagnetic booster separation system
   - Optimize the electromagnetic stage separation system used in the WARRIORS I MQP [21] with respect to mass and power
   - Design and fabricate a reliable and reusable system for electromagnet stage separation

4. Design an autorotation blade system for rocket descent and recovery
    - o Research helicopter and wind turbine blades; and blade element theory
    - o Use MATLAB® and the software package XFLR5 to analyze forces produced by blades

1.6 MQP Tasks and Timetable

The MQP tasks were organized and tracked using a Gantt chart where each team member could update their progress. The Gantt chart can be found in Appendix C.

Chapter 2: Propulsion

2.1 Background

Often, it is quite simple to select a single rocket motor that generates enough thrust and total impulse to propel the rocket to the desired height. However, it is possible to use multiple motors as an advanced propulsion system, as strategy known as "motor clustering" in the hobby rocketry community. Motor clustering makes motor selection and configuration more complicated and significantly increases the importance of having a reliable ignition system, so motor clustering is rarely attempted in hobby rockets. Therefore, this project presented an opportunity for further research, testing, and construction of a clustered motor propulsion system to determine motor clustering's feasibility and advantages compared to a single motor configuration.

2.1.1 Engine Clustering

Motor clustering is the practice of using multiple motors for a propulsion system. Motor clustering can be implemented by using multiple motors as the main propulsion system in the rocket airframe or by using multiple motors as boosters outside of the main propulsion system. Motor clustering is less common in model rockets due to the higher complexity involved; however, the practice does offer some incentives and academic merit.

The configuration and ignition of clustered motors are key factors for a successful rocket launch. No matter how many motors are being clustered, the motor configuration needs to have symmetry about the center axis of the rocket [22]. This is true when a multiple of the same motor or two or more different motors are being used. Motors that are clustered for the main propulsion system should be arranged as close to the center axis as possible. Maintaining symmetry and locating the motors as close as possible to the central axis are two strategies to minimize the possibility of generating torque about the center of gravity of the rocket, which would lead to major stability problems during launch [22]. Figure 2.1 shows examples of typical clustered motor configurations for the main propulsion about the center axis. Booster motors can be arranged outside the airframe of the rocket; however, this means the booster motors are much farther away from the center axis compared to the main propulsion system. As a result, clustering external booster motors increases the risk of generating unwanted torque on the rocket. Therefore, booster

motors should not exceed a "moderate" total impulse (E-G impulse class) so that the risk for torque is minimized [22]. The simultaneous ignition of all clustered motors is also essential to minimize the effects of torque. If just one motor is not ignited at the exact moment that all the other motors are ignited, a torque may be produced that is large enough to substantially change the orientation of the rocket at launch. Therefore, the number of motors clustered should be minimized to reduce the risk of generating torque at launch due to ignition unreliability [22].
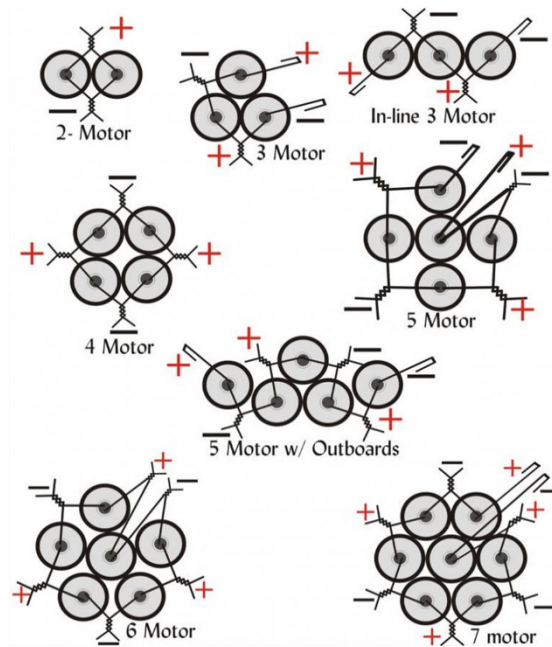
Figure 2.1. Motor clustering configurations [22]. Copyright © 2012 National Association of Rocketry.

Motor clustering requires a few modifications to model rocket hardware and analysis compared to conventional single motor propulsion systems. In the case of motor clustering, there are several modifications that need to be made to the motor mount. Each motor needs its own motor tube, and each motor tube needs a slot in the centering rings to allow for a secure fit. The centering rings will thus need to be designed to match the configuration of the motor cluster. Figure

2.2 shows an example of an optimal centering ring and motor body tube design for three clustered motors as the main engine. In addition, to analyze the characteristics of the overall propulsion system, a composite thrust curve will need to be generated that adds the thrust curves of all individual motors. Motor selection will change the average thrust, maximum thrust, and burn-time of the entire system. The total impulse can simply be calculated by adding the delivered impulse of all the individual motors [22].
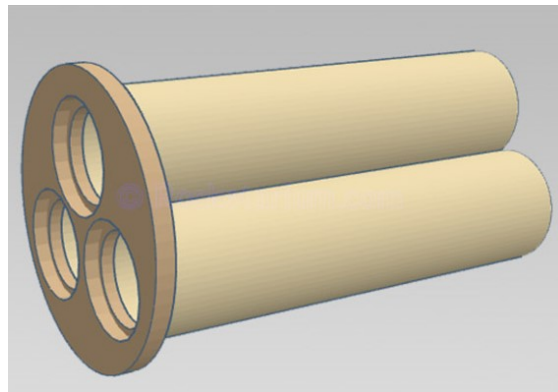
Figure 2.2. Motor mount for three clustered motors [23]. Copyright © 2018 Rocketarium.

Although motor clustering is a higher-risk option compared to using a single motor, there are some incentives that make motor clustering a worthwhile propulsion option. First, motor clustering adds both the total impulse and thrust of each individual motor. For long-burn motors with lower average thrusts, this can be a useful way to provide a higher average thrust to accelerate heavier rockets if long-burn motors are desirable [22]. Also, this additive property allows for more flexibility in terms of combining the total impulses of each motor to achieve the optimal total impulse. Clustering motors can also be used to decrease the required length of the airframe. For example, clustering 3 H motors can provide comparable total impulse and thrust values to a single I motor, but the length of the H motors is only 1/3 of the length of the I motor [8]. Therefore, motor clustering can decrease the required length of the motor section and help create space within the airframe for other rocket subsystems. Motor clustering is also a way to model some aspects of the propulsion system used in actual launch vehicles, such as NASA's SLS (Space Launch System) t,

which will cluster four RS-25 engines as well as two boosters [24]. Therefore, there is academic merit in investigating and successfully launching a model rocket with clustered motors.

However, along with the risks of torque and non-simultaneous motor ignition, there are a few downsides to motor clustering. Motor clustering can often weigh more than just a single motor system. This is due to the increased mass of all the motor propellants and the mass of multiple motor casings. Therefore, this can increase the mass of the rocket and decrease the amount of acceleration generated from the motors during launch [24]. In addition, the cost of multiple propellant kits and motor casings is almost always more expensive than a single casing and propellant kits for a single motor [24]. In conclusion, if one has a reliable ignition system, a proper motor configuration, and a large enough budget, motor clustering can be an innovative alternative to using a single motor as a propulsion system.

2.1.2 Ignition Systems

There are several types of ignition systems used in rocketry on both the recreational and industrial level. For hobby rocketeers, the most common types of ignition systems include the use of electronics, ignition powders, and/or pyrogens [25]. Alternative methods of ignition systems include low-current systems, mini-bulbs, hot particle igniter compounds, and nitrate-based compounds for hybrid propellant systems [26].

One system relies on black powder, which is available commercially, but some rocket hobbyists make their own custom powders. Richard Nakka, author of an extensive experimental rocketry website, uses a custom black powder made of 20% charcoal and 80% potassium nitrate [26]. Commercial powders often include sulfur to make ignition easier, but it can also be more dangerous, as the propellant is more likely to be accidentally ignited. Electric ignition systems, often referred to as an "electric match", use a resistive metal wire dipped in pyrogen, which is a highly flammable material, usually consisting of a fuel mixed with an oxidizer [26]. When the wire heats up to a certain temperature, the pyrogen ignites and releases energy as heat to the propellant, which begins the burning process near instantaneously. This process allows for energy dissipation between the battery and the igniters [26]. The range safety officer at a launch site will provide the power switch, battery, and wires to connect to our own resistive wires.

An electronic ignition system and its wire are analogous to a lightbulb and its filament. A lightbulb's filament gives off energy in the form of light and heat once it passes through the red-hot phase to the white-hot phase, while an igniter is designed to produce enough energy as heat, rather than light, to ignite the combustible pyrogen compound [25]. The extreme heat melts and vaporizes the wire in the process, similar to a filament wire breaking once the bulb is "dead." Once the pyrogen ignites and reaches a high enough temperature, it throws bits of hot material into the propellant and starts the burning process [25].

A common wire material for the resistive wire is nichrome, a nickel-chromium alloy [25]. Nichrome has a high resistivity compared to the lead wire used at the launch site to supply power from the battery, typically copper. The effectiveness of a wire used in an ignitor is determined by the material, diameter, length, current running through the wire, and its heat dissipation capability, which is determined by its resistivity, diameter, and length. The wire is dipped into a pyrogen, which ignites and then, in turn, ignites the rocket motor grain as described above [25]. Ideally, all heat from the igniter is transferred to the pyrogen, but as in all real processes, some heat is lost from the system through dissipation. Because the lead wires are often made of copper, which has an excellent conductivity, most of the thermal dissipation occurs in the nichrome wires [25]. There is a voltage drop through the lead wires when current is flowing however, so the shorter the wires are, the more efficient the system is because there is less length along the wire for these ohmic losses. The lead wire, connecting the igniter to the control box and battery system, are typically made of a material with low resistance (a material with properties similar to copper is common) and should be thicker than the wire coated with pyrogen [27] to further minimize the voltage drop

2.1.3 Static Testing

In industry, rocket engines are tested statically on the ground under controlled conditions to ensure engine quality before flight. Static testing is inexpensive compared to in-flight testing due to the risk of systems being lost or damaged in flight. More importantly, the ability to model the performance of a rocket engine is necessary for the analysis of its behavior. Because the tests are placed under controlled conditions, parasitic forces such as gravity and wind are treated as negligible in these static tests. In addition to filtering out these forces under controlled conditions, several performance characteristics can be isolated and determined from these tests including, but

not limited to, a fully generated thrust curve from which total, average, maximum and minimum thrust can be determined, as well as total and specific impulse, exhaust velocity at design, the exit pressure, and any burn rate predictions [28].

To statically test rocket engines of any magnitude, there must be a rigid fixture for the engine to be mounted on. This ensures stability when isolating performance characteristics. The orientation of the rocket can either be horizontal or vertical. A pressure transducer and load cell are required to measure the amount of force that the accelerated gases produce. A data acquisition module is used to capture these data in a digital format so that it can be processed by a computer. Filtering any vibratory noise with signal filters and amplifiers along with the calibration of the sensors and acquisition modules is additively crucial to obtain data that are worth analyzing. Safety precautions must be taken during these tests to ensure protection from hazardous material. These precautions include a minimum distance requirement, a blast hood for shielding, and a controlled ignition system.
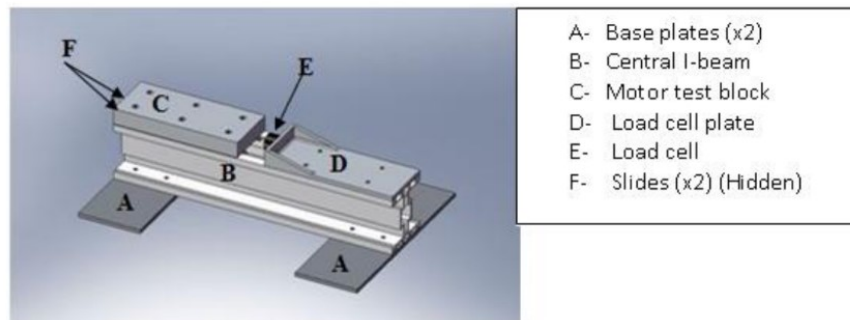
Figure 2.3. WARRIORS III static test mount [29]. Copyright © 2008 WARRIORS III.

Projects such as the Major Qualifying Project (MQP) WARRIORS III [29], drew from these concepts for their own static tests of a hybrid model rocket engine as seen in Figure 2.3. In these tests, the team's rocket engine was mounted to a beam which acted as a rail for the engine to be guided to the load cell used to record the thrust force.

The design faced some obstacles, such as fact that the weight of the motor mount produced torque on some of the hardware which caused friction when sliding on the rail. This resulted in inconsistent contact with the load cell and therefore errors in measurement.

2.1.4 Zero-dimensional (0D) Combustion Model

An important contribution to the propulsion system analysis was to provide a steady state zero-dimensional (0D) combustion model of the rocket motor. A 0D model is a steady state model that has no time dependency. A steady-state model further restricts conditions of the physical combustion process and implies that the system is in chemical equilibrium. The objective of the 0D model is to estimate important motor properties, such as average thrust and specific impulse, using basic physics principles. These physics principles include those related to compressible fluid mechanics in nozzles and the resulting effects on thrust and specific impulse of a rocket motor. This 0D model assumes that the propellant grain produces heated gas in a single step process, ignoring many of the multi-phase and chemical kinetic aspects that are true in a realistic solid motor propellant combustion process. This assumption is necessary because it is very difficult to model the exact chemic process that takes place in the combustion chamber. In addition, the exact chemical composition of the rocket motor propellant is not known as these data were not usually published by the motor manufacturer. Therefore, there are techniques that can be used to estimate the chemical composition of the propellant grain, as well as the chemical composition of the propellant grain combustion products.

A typical high-powered rocket motor propellant consists of approximately 20% fuel and polymer binder, and about 80% oxidizer. It is common for the fuel in model rocket motors to be aluminum, while the oxidizer is ammonium perchlorate. Combustion modeling requires an estimation of the chamber conditions, such as temperature and pressure. Also required are the composition of the combustion reactants (propellant) and products (heated gas) corresponding to these conditions. It is assumed in the 0D model that the composition of the solid propellant is 100% ammonium perchlorate, as this species is most of the propellant. This assumption allows for many simplifications when it comes to computing the composition and properties of the combustion product. Thermodynamic properties useful to this combustion process include temperature,

pressure, density, molecular weight, heat capacity at constant pressure, heat capacity at constant temperature, and the mole and mass fractions of each individual product species. Knowing the mole fraction of the product mixture, the ideal gas law can be used to determine the thermodynamic properties of the burned gas [7].

Cantera is an open-source software toolkit that solves problems involving chemical kinetics, thermodynamics, and transport processes. Cantera can be imported into Python or MATLAB® and can be used to solve for thermodynamic properties of species undergoing a chemical reaction given specified initial conditions. For chemical equilibrium processes, the initial temperature, pressure, and mole fraction of the reactant species must be specified. The thermodynamics properties of the products (resulting from the chemical reaction) that can be computed from Cantera include the final composite temperature, pressure, density, molecular weight, heat capacity at constant pressure, heat capacity at constant temperature, and the mole and mass fractions of each individual product species [30]. The chemical equation for the combustion of ammonium perchlorate can be simplified according to Eq. (2-1). However, a more accurate chemical composition for the combustion products can be computed using Cantera. A diagram of the combustion process, which includes the burn rate and the mass flow rate of the combustion products produced are shown in Figure 2.4.

$$1NH_4ClO_4(s) \longrightarrow \frac{3}{2}H_2O\ (g) + \frac{5}{4}O_2(g) + 1HCl\ (g) + \frac{1}{2}N_2(g) \qquad (2\text{-}1)$$
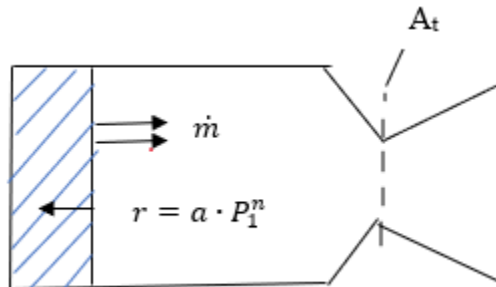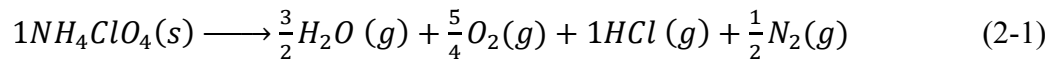
Figure 2.4. 0D model combustion chamber and nozzle diagram.

2.1.5 Heat Flux Modeling and Simulations

COMSOL Multiphysics a finite element analysis (FEA) solver and simulation software that uses physics-based user interfaces and coupled systems of partial differential equations [31]. Using a combination of physics modules in COMSOL allows for coupling effects that are often not possible in most FEA software. In particular, the heat transfer and computational fluid dynamics (CFD) modules in COMSOL can be coupled to simulate "conjugate" heat transfer. Conjugate heat transfer refers to the combination of heat transfer in solids and fluids through both conductive and convective heat transfer. Conductive heat transfer refers to the transfer of thermal energy from an area of higher atomic or molecular kinetic energy to an area of lower kinetic energy through molecular collisions. Conductive heat transfer can be described with respect to the temperature gradient between two cross sections and can be expressed through Fourier's Law for time independent problems as seen in Eq. (2-2),

$$q = -k\nabla\mathbf{T} \tag{2-2}$$

where q is the heat flux (energy flow per unit area, per unit time), k is thermal conductivity, and $\nabla\mathbf{T}$ is temperature gradient. Convective heat transfer is caused by the combined transport of thermal energy due to the dissipative, or conduction, process just described, in addition to an advective contribution, i.e. carried by a fluid with some bulk, or average, velocity. Depending on the thermal properties on the fluid and on the flow regime, either the advective or the conductive heat transfer can dominate. The viscous effects of the fluid flow can also produce fluid heating; however, this contribution is negligible for fluid flows with a low magnitude velocity field. For time-independent, inviscid conductive and convective heat transfer in a fluid, these effects can be described by Eq. (2-3),

$$\rho C_p(\mathbf{u} \cdot \nabla\mathbf{T}) = \alpha_p T(\mathbf{u} \cdot \nabla\mathbf{P}) + \nabla \cdot (k\nabla\mathbf{T}) + Q \tag{2-3}$$

where ρ is density, C_p is specific heat capacity at constant pressure, $\mathbf{u}$ is velocity, α_p is convective heat transfer coefficient, $\nabla\mathbf{P}$ is the gradient of pressure, and Q is heat source/sink flux [32].

The laminar flow module in COMSOL couples the Navier Stokes Equation and the Continuity Equation. The partial differential equation of the Navier Stokes Equation that COMSOL uses to apply the conservation of momentum principle in fluid flow is,

$$\rho(\boldsymbol{u} \cdot \boldsymbol{\nabla})\boldsymbol{u} = \boldsymbol{\nabla} \cdot \left[-P\boldsymbol{I} + \mu(\boldsymbol{\nabla}\boldsymbol{u} + (\boldsymbol{\nabla}\boldsymbol{u})^T) - \frac{2}{3}\mu(\boldsymbol{\nabla} \cdot \boldsymbol{u})\boldsymbol{I} \right] + \boldsymbol{F} \qquad (2\text{-}4)$$

where ρ is density, $\boldsymbol{u}$ is velocity, P is pressure, μ is dynamic viscosity, $\boldsymbol{I}$ is identity matrix, and $\boldsymbol{F}$ is external force. The continuity equation is the conversation of mass for fluid flow and is expressed by the following partial differential equation in COMSOL,

$$\boldsymbol{\nabla} \cdot (\rho\boldsymbol{u}) = 0 \qquad (2\text{-}5)$$

where ρ is density and $\boldsymbol{u}$ is velocity. COMSOL also uses additional equations for specific boundary conditions that can be applied. For both the thermal insulation and outflow boundary conditions, the following equation is used to make the derivative of heat (heat flux) through the boundary equal to zero,

$$-\boldsymbol{n} \cdot \boldsymbol{q} = 0 \qquad (2\text{-}6)$$

where $\boldsymbol{n}$ is the unit normal to the boundary and $\boldsymbol{q}$ is heat flux. For a wall boundary condition, the following equation is used to specific that there is no fluid flow through the boundary,

$$\boldsymbol{u} = 0 \qquad (2\text{-}7)$$

where $\boldsymbol{u}$ is velocity. For a one-dimensional inlet boundary condition, the following equation is used to specify the magnitude and direction of the inlet flow,

$$\boldsymbol{u} = U_0\boldsymbol{n} \tag{2-8}$$

where $\boldsymbol{u}$ is velocity, U_0 is the velocity magnitude specified by the user, and $\boldsymbol{n}$ is the unit normal to the boundary. For an outlet boundary condition, the following equation is used as a modified Navier Stokes equation with no additional external force term

$$\left[-P\boldsymbol{I} + \mu(\nabla\boldsymbol{u} + (\nabla\boldsymbol{u})^T) - \frac{2}{3}\mu(\nabla \cdot \boldsymbol{u})\boldsymbol{I}\right]\boldsymbol{n} = -P_0\boldsymbol{n} \tag{2-9}$$

where ρ is density, $\boldsymbol{u}$ is velocity, P is pressure, μ is dynamic viscosity, $\boldsymbol{I}$ is identity matrix, P_0 is the pressure specified at the outlet by the user, $\boldsymbol{n}$ and is the unit normal to the boundary. For a specific temperature boundary condition, COMSOL uses the equation

$$T = T_o \tag{2-10}$$

where T is temperature and T_o is the specified temperature by the user. For a volumetric heat source domain condition, COMSOL uses the equation

$$Q = Q_0 \tag{2-11}$$

where Q is volumetric heat flux and Q_0 is the specified volumetric heat flux by the user. The specified Q_0 can be calculated using the equation,

$$Q_0 = \dot{m}C_p\Delta T \qquad (2\text{-}12)$$

where Q_0 is volumetric heat flux, $\dot{m}$ is mass flow rate, C_p is thermal conductivity at constant pressure, and ΔT is the average temperature of the flame.

2.2 Methodology

The primary design considerations for propulsion involved selecting a motor configuration and ignition system that would successfully ignite the engine during launch. The two medium risk strategies that were investigated were (1) clustering multiple motors as the main engine in the rocket's airframe and (2) using booster motors in addition to the main engine. The added complexity and academic merit of using these higher risk strategies were weighed against the low risk option of using a single motor as the main engine in the rocket's airframe. To coincide with the goals of the project, we chose to incorporate both medium risk strategies by clustering multiple motors inside the rocket airframe and using multiple exterior booster motors to form an innovative model rocket propulsion system. This propulsion system required modifications to a conventional motor mount and ignition system for a single motor, and so the motor mount and ignition system also factored into our overall system design. To expand on the academic merit of investigating an advanced propulsion system for a model rocket, we also attempted to model the heat flux and compressible flow within a composite propellant motor. This level of modeling and analysis is rare in the model rocketry community, and so there was additional incentive to conduct this modeling as an academic exercise. Once we selected our design choice of clustered main engine motors as well as using boosters, it was possible to state the objectives for the propulsion system:

- Select a motor configuration that provides adequate thrust and total impulse to achieve an altitude of at least 1500 feet, as well as provide symmetry about the rocket's center axis for stability.

- Design and construct an ignition system that ignites all motors simultaneously from the launch pad.

- Design and construct a motor mount that secures and orients all main engine motors about the center axis of the rocket airframe.

- Create models that can be used to investigate: 1) the composition of the motor combustion product gases, 2) the sensitivity of the propellant mass flow rate and required nozzle throat size to chamber temperature and pressure, and 3) = the heat flux from the motor to the surrounding structure.

2.2.1 Engine Clustering

To begin selecting our clustered motor configuration, we first researched commercially available motors certified by either the NAR, TRA, or CAR[1]. We primarily investigated rocket motors manufactured by Aerotech and Cesaroni. These companies are two of the largest manufacturers of high-powered composite rocket motors. They provide a variety of single-use and reloadable motor types in almost all impulse class ranges, which gave us many options to choose from. We decided to aim for a motor configuration that allowed for the highest total impulse consistent with our certification level (Level-1), that would also satisfy our flight objectives to reach an altitude of over 1500 feet. A member of our team had a Level-1 NAR/TRA certification, and therefore, our total impulse limit for this certification was 640 N·s.

While researching motors, we also investigated the incentives of using motor clustering as an advanced alternative to using a single motor. We developed an impulse-mass trade study to

---

[1] National Association of Rocketry, Tripoli Rocketry Association, and Canadian Association of Rocketry, respectively

determine the tradeoffs of motor clustering versus a single motor. This study compared the total impulse and mass of several configurations of multiple G and H motors to the total impulse and mass of a single I motor. This impulse-mass trade study can be found in Appendix A. We predicted that using multiple motors would add additional casing mass, thus the impulse-to-mass ratio for a clustered motor propulsion system would be less than that of a single motor. From this study, we determined that the clustering of H motors would be the most viable compared to clustering G or lower impulse motors. We also deduced that the impulse-mass ratio for multiple H motors was only slightly less than that for a single I motor. According to our study, the average impulse-to-mass ratio for a three H motor cluster was 0.859 N·s/kg, compared to the average impulse-to-mass ratio of 0.891 N·s/kg for a single I motor. Another incentive for using H motors was that the length of an H motor is up to three times less than the length of the highest impulse I motor; this allowed for a shorter motor section, resulting in more room for other rocket subsystems and minimizing the length of the rocket.

Once we finalized our decision to use motor clustering as a propulsion system, we began researching the best motor configuration. In addition to clustering motors for the main engine in the rocket airframe, we also planned to use booster motors in parallel to utilize an electromagnetic booster separation system. Therefore, the maximum total impulse of 640 N·s would have to be split between the main engine motors and the booster motors. For our main engine, we decided to cluster three motors together about the airframe's center axis. A three-motor cluster allowed for radial symmetry about the center axis, which was desirable to minimize unwanted torques generated by deviations in the thrust and burn time of particular motors. Clustering two or three motors for the main engine also offered the most ignition reliability, since using additional clustered motors leads to a greater probability of non-simultaneous ignition. For our first launch, we did not use our booster motors - only the main engine's three motors. We intended to launch the three motors alongside our boosters for our second launch, however we were not able to launch again.

Primarily, we researched reloadable motors due to the flexibility it gave us with our choice of stage separation mechanism. We did not need the ejection charge that comes with most rocket motors because we planned to use a CO_2 separation system. Reloadable motors come with an ejection charge module that is separate from the propellant and delay grain; thus, it is optional to

use the ejection charge with reloadable motors. This offered an easy way to "plug" the motor simply by not loading the ejection charge in the motor casing. We used a plugged forward closure that was manufactured specifically for plugged motors instead of using a regular forward closure as a cap for the reloadable motor casing.

Table 2.1. Motor statistics for Aerotech H73J and D9W motors

Parameter	Variable Name	Value	Units
V_0	Inlet Velocity	2	m/s
T_f	Flame Temperature	2354	K
T_a	Ambient Temperature	298	K
P_1	Outlet Chamber Pressure	2.0684e7	Pa
Q_0	Volumetric Heat Source	35138.5	W/m^2

From our impulse-mass trade study, we decided that clustering three H motors for the main engine would give a greater impulse-mass ratio than clustering three G motors. According to our study, the average impulse-to-mass ratio for a three H motor cluster was 0.859 N·s/kg, compared to the average impulse-to-mass ratio of 0.699 N·s/kg for a three G motor cluster. H motors have a total impulse that range from 160-320 N·s, and therefore clustered H motors could have a total impulse range from 480-960 N·s. Since our total impulse limit for Level-1 certification was 640 N·s, we decided to use three identical H motors at the lower end of the H class total impulse spectrum. We decided to use the Aerotech H73J motor with a total impulse of 185.6 N·s and combined total cluster impulse of 556.8 N·s. With a margin of approximately 80 N·s before we reached the total impulse limit, we decided to use four D motors at the higher end of the D class for the boosters. We selected the Aerotech D9W motor with a total impulse of 18.76 N·s and combined total (booster cluster) impulse of 75.04 N·s. Also, there is an advantage to using D motors as booster motors to minimize potential torques caused by the booster motors. The stability of the rocket is quite sensitive to deviations in the thrust and burn time of the booster motors because the boosters are located relatively far from the center axis of the rocket (~6.35 cm). The overall motor configuration, three main engines plus four boosters, thus gave us a total impulse of 631.84 N·s, just under the 640 N·s limit. The motor statistics for the H73J and D9W motors are given in Table 2.1. In addition, the composite thrust curve for the first launch (three H motors) and

second launch (three H motors and four D motors) are shown in Figure 2.5 and Figure 2.6 respectively, which we generated in Microsoft Excel and MATLAB®, respectively [33].
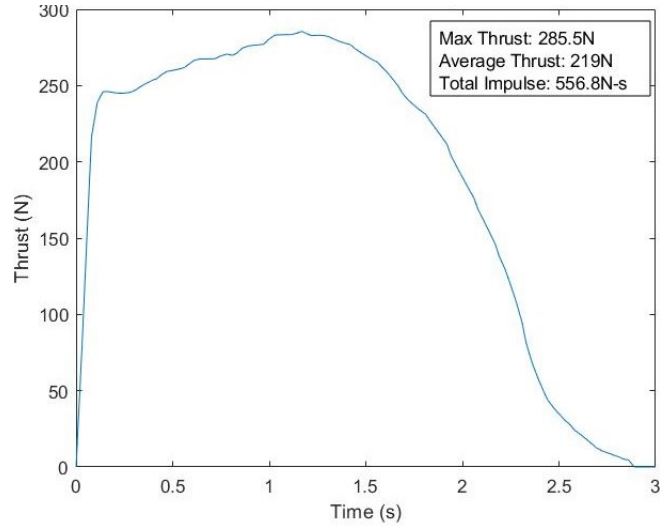
Figure 2.5. Thrust curve for first launch (3 H motors).
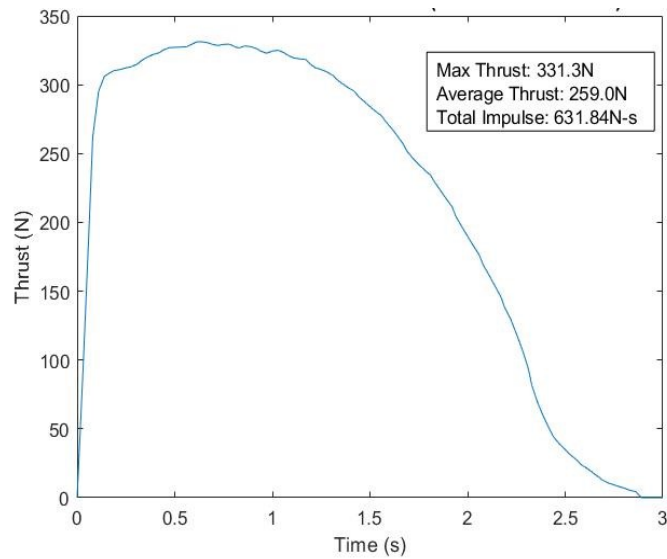
Figure 2.6. Thrust curve for second launch (3 H and 4 D motors).

Once the motor configuration was selected, we were tasked with modifying a typical motor mount design to hold the three H motor cluster in the main airframe of the rocket. Because each Aerotech H73J motor required an RMS (Reloadable Motor System) 38 x 240mm casing, we cut 38 mm diameter paper tubing into three 240mm sections as body tubes for each motor. Next, a typical centering ring model needed to be modified to align the three motor body tubes with radial symmetry about the center axis of the airframe. We needed to consider the diameter of the aft closures for each motor casing because the diameter of the closures was greater than the diameter of the casing. The three 38 mm holes in the centering ring were spread out from the center to account for this, so that they were equidistant from the center and outer diameter of the centering ring. In addition, two of the three centering rings needed to have a slightly smaller overall diameter to account for the increased thickness of the rocket airframe towards the lower end of the motor section. We manufactured the centering rings from plywood using the laser-cutter in the WPI Washburn manufacturing lab. The CAD model for the centering rings is shown in Figure 2.7. We assembled the motor from the RMS 38 x 240 mm casing, the 38 mm plugged forward closure and aft closure, as well as the propellant grain, delay grain, and the igniters from the H73J propellant kit. The motors were assembled prior to launch date and then inserted and secured into the motor body tubes at the launch site.
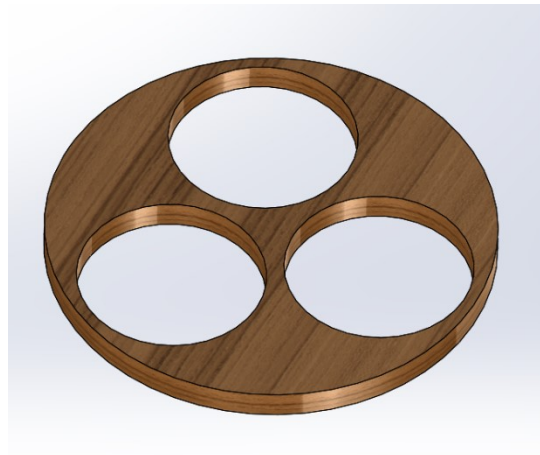
Figure 2.7. Centering ring for main engine motor cluster. For scale, the diameter of each of the three holes is 38 mm.

2.2.2 Igniter Systems

The commercial motor kits we investigated all include appropriate igniters for launching. Our plan was to use electric match "e-match" igniters to initiate the stage separation process for our first launch attempt, before implementation of the CO_2 separation system on later launches. One solution was to construct our own igniters. The igniters that came with the H73J and D9W motors are e-match igniters of the type described in Section 2.1.2, which also work for the stage separation ejection charge. We further investigated how to manufacture those ourselves.

The two key components of the electric match igniter are high-resistance wire and a pyrogen tip. Many premade igniters use nichrome wire, so we investigated what type of nichrome wires and what type of pyrogen dips were available from Apogee Components. They offer 28 AWG (0.321 mm diameter) and 32 AWG (0.202 mm diameter) nichrome wire with an electrical resistance of 4.04 Ohm/ft and 10.871 Ohm/ft respectively. The 32 AWG wire was ordered to have an option with a higher resistance in order to generate more heat. For the pyrogen dip, they offer a QuickDip compound which burns slowly, similar to a sparkler, and an H-3 compound which is more sensitive to heat and will ignite much quicker. Both pyrogen dips consist of a powdered fuel and oxidizer, the H-3 dip additionally included a vial of binding agent. We decided to use the H-3 Compound for our igniters.

Construction of the ignitors consisted of the following steps. First, we measured out equal lengths of wire to ensure heat transfer to the pyrogen at the same rate for a given current. For the ejection charge testing, we used wire segments 254 mm long, but for the motors themselves, the igniters must run through the length of the fuel grain (240mm), so we needed 480mm segments for the motors. The pyrogen came as three separate components - a fuel, a binder, and an oxidizer. Shipping the components separately reduces shipping hazards that would exist if the components were provided as a pre-mixed, flammable mixture. Instructions are provided to combine the ingredients with the addition of acetone. Once the pyrogen was mixed and the wires were cut, we bent the wires in half and dipped the bent end into the pyrogen until the mixture stuck onto the end. We made sure all the e-matches had approximately the same amount of pyrogen on them by visual check for the first test but decided any future igniter manufacturing should include the use of a balance to weigh the wires before and after adding the pyrogen to ensure they have the same amount of pyrogen by mass. These igniters that were fabricated are shown in Figure 2.8.

Figure 2.8. First attempt constructing electric match igniters. Ignitors are shown taped to workbench to allow drying.

The nichrome wires used on our igniters do not require insulation as long as the wires do not touch each other, since they will be connected to the battery and ignition cables via a clip whip (described in Section 2.3.2), which runs most of the length from the motors to the launch controller.

2.2.3 Zero-dimensional (0D) Combustion Model

We developed a zero-dimensional (0D) steady-state model of the combustion and compressible flow within the motor. This model allowed us to estimate important motor properties for the selected H73J and D9W motors, which we then compared to NAR/TRA reported values.

First, we evaluated the decomposition and determined the chemical equilibrium composition of the exhaust products. For simplicity, we modeled the fuel as pure ammonium perchlorate with no added fuels, binders, or other additives. We analyzed the simplest case of the decomposition of ammonium perchlorate based on its four most prominent products: water vapor ($\frac{3}{2}$ H_2O), oxygen gas ($\frac{5}{4}$ O_2), hydrogen chloride (1 HCl), and nitrogen gas ($\frac{1}{2}$ N_2). This allowed us to model a "burned gas" with known composition and gas properties, without the need to use specialized software. In addition, we also modeled the ammonium perchlorate decomposition

using the Cantera software suite to define a more realistic estimate of the burned gas composition and properties for different chamber pressure conditions. This chemical equilibrium model provided the composition of the product gas mixture. We used these results to create a 0D model, which could then be used to evaluate the mixture properties and an estimate of the adiabatic flame temperature. Next, we determined the typical burning characteristics of ammonium perchlorate for different chamber pressures and propellant grain configurations. Using data points from a curve fit model [34], we were able to find the burn rate coefficient. We calculated the mass flow rate generated from the combustion products using the burn rate that we calculated corresponding to the given pressure as well as for different grain surface areas that are typical for our selected motors.

We then developed a steady state compressible flow model for the burned gas through a nozzle section. This model assumed different chamber pressure conditions since the chamber pressure of our motor was not provided by the motor manufacturer. We first determined the burn rate of the ammonium perchlorate propellant grain as a function of chamber pressure using data points given by a study that was conducted by Chen and McQuaid [34]. Next, we estimated the mass of the burned gas products from the propellant combustion process based on the burn rate and the density of the burned gas computed in Cantera. We then equated this mass of burned gas produced to the mass flow rate through the nozzle section, which is a constant for any cross-section within the nozzle. We then measured the nozzle throat and exit diameters of the Cesaroni I218 motor nozzle and calculated the nozzle throat and exit cross-sectional areas. Using these area values and compressible fluid isentropic relations, we calculated the pressure at the nozzle throat and exit cross-sections. These pressure values, cross-sectional areas, and resulting ratio of specific heat values computed in Cantera allowed us to calculate the estimated thrust and specific impulse as a function of the chamber pressure. These steps and equations needed for the 0D model are provided in the flow chart that is given in Table 2.3. The nomenclature for the variables in these equations are shown in Table 2.2. Finally, we compared the calculated minimum nozzle throat area, thrust, and impulse values for typical chamber pressures to the values reported by the NAR/TRA testing committees [35].

Table 2.2. Nomenclature and units for 0D modeling.

Name	Variable	Units
Thrust	T	N
Specific Impulse	I_{sp}	Sec
Gravitational Constant	g	m/s^2
Specific Heat Constant at Constant Pressure	C_p	J/kg mol K
Surface Area of Propellant Grain	A_s	m^2
Thrust Coefficient	C_F	~
Specific Heat Ratio	k	~
Specific Heat Ratio	γ	~
Minimum Throat Area	A_t	m^2
Density of solid Ammonium Perchlorate	ρ	kg/m^3
Chamber Pressure	P_1	Pa
Pressure at Nozzle Exit	P_2	Pa
Atmospheric Pressure	P_3	Pa
Mass Flow Rate	$\dot{m}$	kg/sec
Heated Gas Temperature	T_1	K
Burn Rate	R	mm/s
Burn Rate Coefficient	a	~
Total Number of mols Per Unit Mass of Mixture	N	Mol
Molar Mass Effective	MM_{eff}	kg mol/kg
Specific Gas Constant Effective	R_{eff}	J/kg K
Universal Gas Constant	$\bar{R}$	J/kg mol K
Subscript-Constituent of Species	J	~
Subscript-Mixture of Gases	Mix	~
Subscript-Effective	Eff	~
Exponent-Pressure Exponent	n	~

Table 2.3. Calculation sequence (flowchart) for 0D propulsion model.

Equation	Given	Previously Calculated	Unknowns	Equation Reference	Equation Number in Given Reference
System 1					
$MM_{eff} = \dfrac{\sum n_j \cdot MM_j}{\sum n_j}$	$\dfrac{\sum n_j \cdot MM_j}{\sum n_j}$	~	MM_{eff}	[7]	5-5
$R_{eff} = \dfrac{\bar{R}}{MM_{eff}}$	$\bar{R}$	MM_{eff}	R_{eff}	~	~
$(C_p)_{mix} = \dfrac{\sum n_j (C_p)_j}{\sum n_j}$	$n_j, (C_p)_j$	~	$(C_p)_{mix}$	[7]	5-6
$\gamma_{mix} = k_{mix} = \dfrac{(C_p)_{mix}}{(C_p)_{mix} - \bar{R}}$	$\bar{R}$	$(C_p)_{mix}$	γ_{mix}, k_{mix}	[7]	5-7
System 2					
$r = a \cdot P_1^n$	a, P_1, n	~	r	[7]	12-5
System 3 Block 1					
$\dot{m} = \rho \cdot r \cdot A_s$	ρ, A_s	r	$\dot{m}$	[7]	12-1
System 3 Block 2					
$\dot{m} = \dfrac{A_t \cdot P_1}{\sqrt{R_{eff}T_1}} \cdot \left[\gamma \left(\dfrac{2}{\gamma+1} \right)^{\frac{\gamma+1}{\gamma-1}} \right]^{\frac{1}{2}}$	P_1, T_1	$\dot{m}, R_{eff}, \gamma$	A_t	[7]	3-24
System 4					
$C_F = \sqrt{ \dfrac{2k^2}{k-1} \left(\dfrac{2}{k+1} \right)^{\frac{(k+1)}{(k-1)}} \cdot \left[1 - \left(\dfrac{P_2}{P_1} \right)^{\frac{k-1}{k}} \right] } + \dfrac{P_2 - P_3}{P_1} \cdot \dfrac{A_s}{A_t}$	P_1, P_2 P_3, A_s	A_t, k	C_F	[7]	3-30
$T = C_F \cdot A_t \cdot P_1$	P_1	A_t, C_F	T	[7]	3-31
$I_{sp} = \dfrac{C_F \cdot P_1 \cdot A_t}{\dot{m}g}$	g, P_1	$\dot{m}, A_t, C_F$	I_{sp}	~	~

2.2.4 Heat Flux Modeling and Simulations

In addition, as part of our analysis we developed a COMSOL model that estimated the heat flux through the propellant grain and motor casing from combustion in the motor combustion chamber. This 2D model considered an axisymmetric cross section of the of cylindrical

combustion chamber and assumed that the propellant grain used in our motor had a nearly tubular configuration. The model cross-section, with domain and boundary labeling, are provided in Figure 2.9 and Figure 2.10. This cross-section consisted of a thin aluminum casing domain, a solid ammonium perchlorate propellant domain, a volumetric heat source domain, and a heated gas fluid flow domain. The heated gas flow goes from right to left from the inlet to the outlet as shown in Figure 2.10. The domain phase, material, and governing equation are summarized in Table 2.4. In addition, the material properties of the materials used in these domains are provided in Table 2.5.
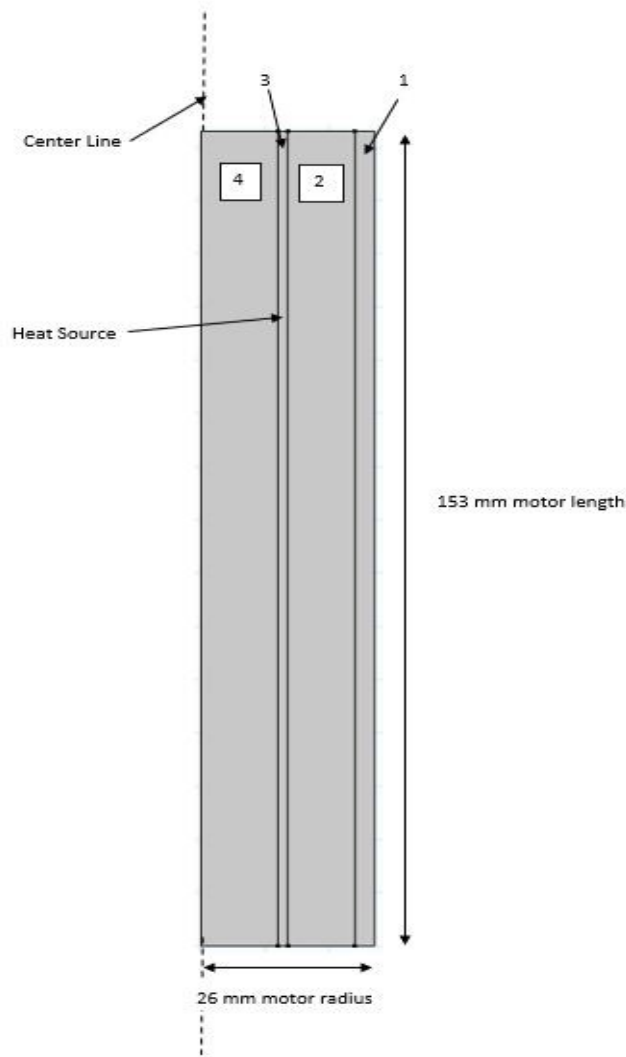
Figure 2.9. Diagram of chamber for 0D propulsion model.
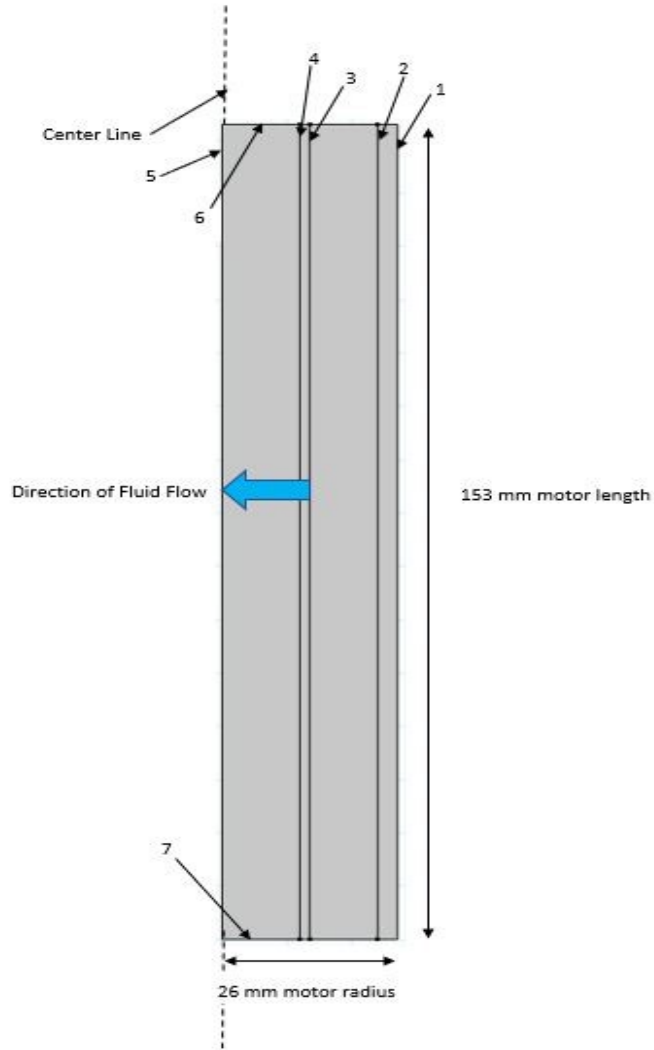
Figure 2.10. Heated gas flow diagram for 0D propulsion model.

Table 2.4. Domain conditions and materials.

Domain	Phase	Material	Model Equations
1	Solid	Aluminum	Eq. (2-2)
2	Solid	Ammonium Perchlorate	Eq. (2-2)
3	Fluid	Combustion Products	Eq. (2-3), Eq. (2-4), Eq. (2-5)
4	Fluid	Combustion Products	Eq. (2-3), Eq. (2-4), Eq. (2-5)

Table 2.5. Manually-created material properties.

Material	Thermal Conductivity [W/m-K]	Heat Capacity [J/kg-K]	Density [kg/m3]	Ratio of specific heats	Dynamic Viscosity [Pa-s]
Aluminum	238	900	2700	-	-
Ammonium Perchlorate	0.5301-0.4552·T	1084.4-1415.1·T	1949	-	-
Burned Gas	0.03	1554.9	29.1863	1.2401	3.78

The ammonium perchlorate thermal conductivity and thermal and heat capacity were estimated using a linear, temperature-dependent model developed from empirical results [35]. The heated gas properties were estimated using results from our Cantera analysis for a pressure of 3000 psia. The heated gas properties and mole fractions of the most prominent combustion products at 3000 psia are given in Table 2.10 and Table 2.11, respectively. Since COMSOL also requires the thermal conductivity and dynamic viscosity for a manually defined fluid in the laminar flow module these two properties were estimated using that of nitrogen gas at ambient temperature and pressure. In addition, the heat transfer and laminar boundary conditions, as well as the globally defined parameters at those boundary conditions are summarized in Table 2.6, Table 2.7, and Table 2.8.

Table 2.6. Heat transfer boundary conditions.

Boundary	Heat Transfer Conditions	Model Equations
1	Temperature (T_a)	Eq. (2-10)
2	-	-
3	Temperature (T_f)	Eq. (2-10)
4	-	-
5	Outflow	Eq. (2-6)
6	Thermal Insulation	Eq. (2-6)
7	Thermal Insulation	Eq. (2-6)

Table 2.7. Laminar flow boundary conditions.

Boundary	Laminar Flow Conditions	Model Equations
1	-	-
2	-	-
3	Inlet (V_0)	Eq. (2-8)
4	-	-
5	Outlet (P_0)	Eq. (2-9)
6	Wall	Eq. (2-7)
7	Wall	Eq. (2-7)

Table 2.8. Globally-defined parameters.

Parameter	Variable Name	Value	Units
V_0	Inlet Velocity	2	m/s
T_f	Flame Temperature	2354	K
T_a	Ambient Temperature	298	K
P_1	Outlet Chamber Pressure	2.0684e7	Pa
Q_0	Volumetric Heat Source	35138.5	W/m^2

2.3 Results and Analysis

2.3.1 Igniter Systems

Our homemade igniters were ground tested to see if they would light with 12 V, the voltage used at most launch sites. Using approximately 12 cm of wire leading to the pyrogen at the end, it took approximately four seconds to heat up the wire enough to light the igniters, whereas we want a quicker response. This was solved by cutting the igniters to shorten the lead wire to approximately 7 cm instead of the original 12 cm, which allowed the ignition testing to run smoothly.

During the stage separation ground testing at our January 19th test launch, however, the igniters began to heat up but not enough to ignite, so the launch site officials gave us some commercial igniters to use instead. We were informed that launch sites typically do not encourage the use of homemade igniters and gave us a few more to carry out our full-rocket test launch.

2.3.2 Engine Clustering

The three-motor cluster in the central airframe was tested at the launch attempt in January. Once the ignition was initiated through the launch pad, the ignition through the clip whip and the

manufactured igniters was successful. However, the O-rings in each of the motors malfunctioned, which caused the burned gas to leak through the be O-ring openings. This was observed at the launch by the motors generating no thrust but releasing all the gas that was generated during the burn. After diagnosing the issue, it was pointed out that the O-rings were not lubricated before being assembled, which caused the O-rings to deform and not function to seal the burned gas through the nozzle [3].

At the launch we also were informed by the Range Safety Officer and some other participants, of some of the NAR's standards for clustered propulsion systems for more advanced model rockets. We learned that if motor clustering was used as an advanced technique that each individual motor must have a thrust level equal to five times the weight of the entire rocket, a rule we will call the "5x thrust-to-weight ratio rule." This is recommended by the NAR so that if one or more motors either failed to ignite or had non-simultaneous ignition, then the other motors would have enough thrust to propel the rocket off the launch pad [3]. In our first motor configuration, the overall average thrust from the three-motor cluster was 219 N. However, per motor, each of the H motors in our initial motor configuration only have a thrust level of 73 N. This would result with a thrust to weight ratio of 1.64 for our rocket per H motor, which is far under the recommended "5x thrust-to-weight ratio rule."

Table 2.9. Cesaroni I218 motor statistics.

Motor Statistic (units)	Cesaroni P54-1G White Thunder (I218)
Total Impulse (N-s)	491.2
Max Thrust (N)	294.2
Average Thrust (N)	218.3
Total Mass (g)	580
Propellant Mass (g)	230
Burn Time (s)	2.3
Size (mm)	54x143
Propellant	White Thunder
Type	Reloadable
Motor Case	Cesaroni 54 mm 1-Grain

In addition, we learned that some users consider Aerotech motors as less reliable in terms of motor clustering, as their modular assembly raises the chances of manual errors. Therefore, it was recommended to us that Cesaroni motors be used for our next motor configuration. Because

of our troubles with motor clustering, we decided that is would be better, for the purpose of testing other subsystems, to use a single motor as a propulsion system in any future launch. This would mean that we would need to use a single I motor to generate enough thrust to conform with NAR standards compared to the weight of our rocket. In addition, we were confined to selecting 54 mm diameter motors, as these were the only class of motors that would provide enough thrust and fit into our previously constructed rocket motor section size of 101.6 mm diameter x 240 mm length. We ultimately chose the Cesaroni I218 motor, a 54 mm diameter x 142.2 mm length I motor that provides an average thrust of 218 N, which is slightly less than five times the weight of our rocket (44.4N). This motor was chosen because it provided the minimal thrust level that is recommended by the NAR and maximized the total impulse to achieve as high of an altitude as possible. The motor statistics for the Cesaroni I218 motor are shown in Table 2.9.

In terms of booster motor selection, we also were also informed that we would likely not be allowed to launch with a cluster of the D9W motors as boosters, along with the H73J primary motors for the second launch. The reason is that they use different propellants: the H73J motors use ammonium perchlorate composite propellant while the D9W motors use black powder propellant. These two propellants have different ignition temperatures, and so one type of propellant could possibly ignite prior to the other and cause non-simultaneous ignition. This non-simultaneous ignition would likely result in rocket motion that would disconnect the clip whip from the igniters of the other motors, which would prevent the other motors from successfully igniting. Therefore, for future launches we would need to choose booster motors that also use ammonium perchlorate composite propellant. Because of our rocket's fins, it would be most ideal for our booster motors to be as small as possible while still being a high enough impulse class to use composite propellant. Most motor companies do not have composite propellant motors below the F impulse range. A good candidate for lower impulse composite propellant motors would be AeroTech Economax motors. This brand of single-use motors spans the E-F impulse range and also use composite propellant [36]. Therefore, for future launches these types of motors would be most feasible to use as booster motors given our size restrictions.

2.3.3 Zero-dimensional (0D) Combustion Model

Table 2.10 shows the thermodynamic properties for the combustion products of ammonium perchlorate that were computed using Cantera and the input into the system of equations. In

addition, the mole fractions of the four most prominent products of the combustion of ammonium perchlorate that were computed in Cantera are listed in Table 2.11. Cantera computed the mole fractions of approximately 50 possible products; however, the mole fractions of these species is quite negligible compared to those of the four most prominent products. The composite properties and mole fractions were computed over a range of pressures from 1000 to 5000 psia with increments of 500 psia. Since the manufacturer did not provide the chamber pressure of our rocket motor, we selected this range of pressures to be modeled based on typical chamber pressures according to Sutton's book: *Rocket Propulsion Elements* [7].

By plotting burn rate as a function of pressure, we were able to use the curve fitting tool in MATLAB® to estimate the coefficients a and n (the burn rate proportionality constant and burn rate pressure exponent, respectively) in the burn equation shown in Table 2.3 System 2. This curve fit was applied to the data with an R^2 of 0.99, indicating a very accurate estimate for the burn rate coefficients. The results of this burn rate equation curve fit are shown in Figure 2.11. With these burn rate coefficients, we implemented the resulting burn rate equation (analytical equation based off of empirical results) in System 2 of the flowchart methodology.

Table 2.10. Thermodynamic properties of ammonium perchlorate (1000-5000 psia)[2].

Chamber Pressure P_1 [Pa]	6894757	10342136	13789514	17236893	20684271	24131650	27579028	31026407	34473786
Specific Heat at Constant Pressure C_p [J/kg mol K]	1553.4	1554	1554.4	1554.7	1554.9	1555.5	1555.3	1555.4	1555.5
Specific Heat at Constant Volume C_v [J/kg mol K]	1252.4	1252.4	1253	1253.4	1253.8	1254.1	1254.4	1254.6	1254.8
Density of	9.76899	14.6293	19.4846	24.3367	29.1863	34.0339	38.8801	43.7249	48.5687

² Variable descriptions for Table 2.10 are given in the variable nomenclature table, Table 2.2

Burned Gas ρ									
Heated Gas Temp. T_1 [K]	2337.92	2343.92	2348.03	2351.14	2353.63	2355.72	2357.50	2359.07	2360.46

Table 2.11. Mole fractions of most prominent products of ammonium perchlorate combustion.

Products	1000 psia	1500 psia	2000 psia	2500 psia	3000 psia	3500 psia	4000 psia	4500 psia	5000 psia
HCl	0.212541	0.212548	0.212345	0.212060	0.211741	0.211407	0.211068	0.210731	0.210398
H_2O	0.358731	0.359381	0.359938	0.360429	0.360873	0.361279	0.361655	0.362006	0.362336
N_2	0.113402	0.113449	0.113485	0.113515	0.113540	0.113562	0.113582	0.113600	0.113617
O_2	0.281577	0.281802	0.281901	0.281942	0.281951	0.281940	0.281918	0.281887	0.281850
Total	0.966251	0.96718	0.967669	0.967946	0.968105	0.968188	0.968223	0.968224	0.968201

The second performance plot shown in Figure 2.12 shows the thrust as a function of chamber pressure. This thrust does in fact fall in the range published by the manufacurer who claims to have an average thrust of 218 Newtons [37].
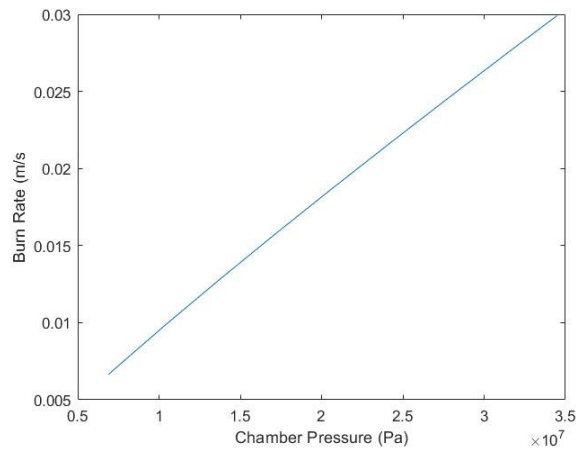
Figure 2.11. Burn rate as a function of pressure.
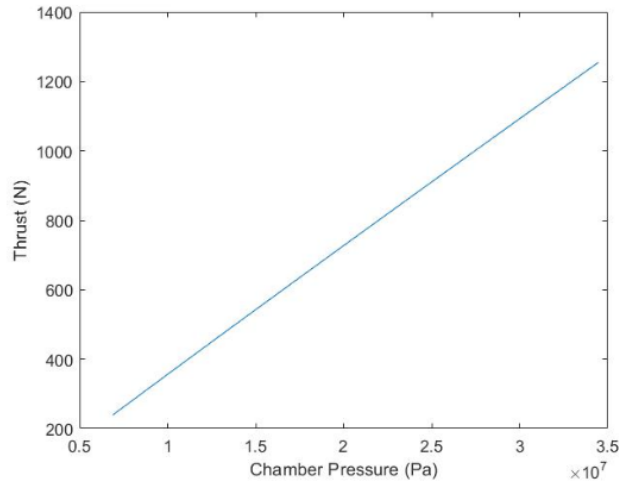
Figure 2.12. Thrust as a function of chamber pressure.

A possible reason for diagreement with published data for the I218 motor are that the constituents of the motor propellant being modeled only includes the oxidizer and not the fuel and binders that are a part of the propellant in reality. One more possible reason for error is mismeasured values and oversimplifying the assumptions being made, such as the steady state and one-phase combustion process.

2.3.4 Heat Flux Modeling and Simulations

The MSAT team was tasked with conducting thermal analysis on the structural components of the airframe. There was concern for the structural integrity of the motor body tubes during combustion in the motors. Since the motor body tubes were made from blue tube (vulcanized paper), there was concern that the high temperature of the aluminum casing would cause the motor body tubes to become singed and lose their durability. Therefore, the PSR team was tasked to estimate the heat flux leaving the motor so that the MSAT team could conduct a thermal analysis on the motor body tubes. The heat flux leaving the motor was estimated using a steady-state conjugate heat transfer model in COMSOL.

From the 2D steady-state conjugate heat transfer COMSOL model, we were able to compute the temperature at any point along the ammonium perchlorate and aluminum domains.

By selecting two points, one at the boundary between the ammonium perchlorate grain and the aluminum grain and one at the end of the aluminum grain, we can find the 1D heat flux across the aluminum casing. The two points selected, and the corresponding temperature values are shown in Figure 2.13. These points were selected at the radial endpoints of the aluminum casing domain.

Using Eq. (2-2) and (2-3) the temperature gradient was calculated and using the thermal conductivity of aluminum provided in COMSOL, the heat flux was calculated to be 377,393 W/m^2. This heat flux value could then be used to conduct thermal analysis on the motor body tubes to see if there is a risk of structural degradation due to scorching.

There were several limitations while conducting this analysis in COMSOL. We initially hypothesized that the heat flux across the propellant grain and casing was going to be dependent on the fluid flow of the heated gas leaving the propellant grain. Since we modeled the flame as a volumetric heat source, we expected fluid flow from the inlet to cause convective heat transfer and carry some of this heat out of the laminar flow control volume. However, this was not observed as the temperature distribution from the inlet to the outlet was purely driven by the temperature gradient created from the temperature boundary condition at the inlet. Multiple cases were attempted in which the outlet boundary was given different temperature conditions, as well as thermal insulation. In the case of thermal insulation, the temperature at the outlet was the same as the temperature at the inlet, indicating that there was no heat transfer in the fluid despite the volumetric heat source. With more time, a solution to this issue may have been found and a more realistic model would have been generated with a temperature distribution in the fluid consistent with convective heat transfer theory.

Another barrier while conducting the COMSOL analysis was the 2D axisymmetric model. When converting the 2D model to 2D axisymmetric, there were issues when computing the solution. With all the boundary conditions kept the same from the 2D model, the 2D axisymmetric model gave the "*Feature: compile equation: stationary (sol1/st1), error: division by zero*" error when we tried to compute the solution. We presumed that this was likely caused because one of the model parameters was zero at the outlet boundary, which is the equivalent to the r = 0 position in the 2D axisymmetric model. We believed that since there was no specified initial condition for the velocity at the outlet, the velocity at the outlet was zero until the laminar flow from the inlet reached the outlet at some moment soon after t = 0. This would have created a singularity if there

was division by the velocity in one of the coupled equations and would align with the specified computation error.
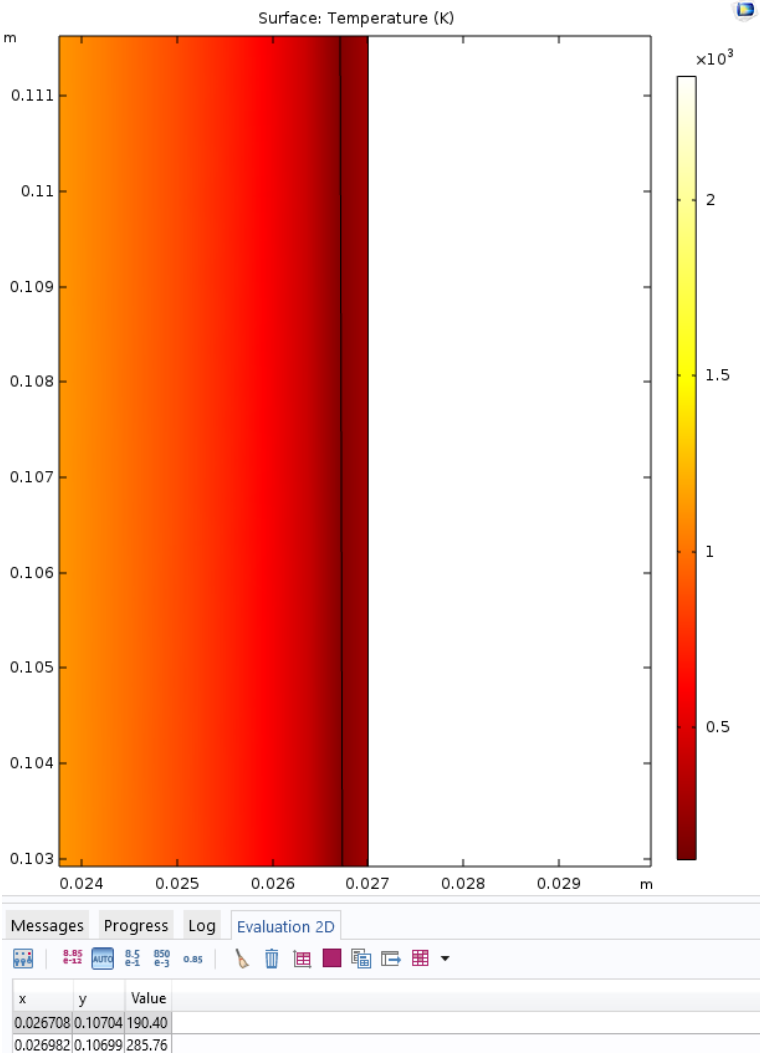
Figure 2.13: Aluminum casing boundary temperature distribution and values.

Chapter 3: Stage Separation

3.1 Background

Carbon dioxide (CO_2) and electromagnetic separation systems are two innovative systems that have limited use in model rocketry. Because these systems have not been extensively investigated, they pose an opportunity to establish new procedures and designs for future use. The inclusion of two different novel stage separation methods adds an extra level of complexity to a model rocket, as compared to using one method or more common methods. The complexities of these systems include the necessary calculations, and the associated construction and integration. However, CO_2 and electromagnetic stage separation systems offer advantages that classic pyrotechnic systems do not, such as testability and safety. These advantages aid reliability and provide a better understanding of the system through catalogued results.

3.1.1 Carbon Dioxide (CO_2) Separation

In model rocketry, carbon dioxide (CO_2) systems have been used for stage separation and ejection mechanisms. In these systems, CO_2 pressurizes the rocket body to jettison the nosecone and release the recovery mechanism. Carbon dioxide systems are increasing in popularity, as discussed in Tinder Rocketry's Peregrine Exhaustless CO_2 Ejection System Manual [38], due to their advantages over common pyrotechnic methods, such as black powder charges.
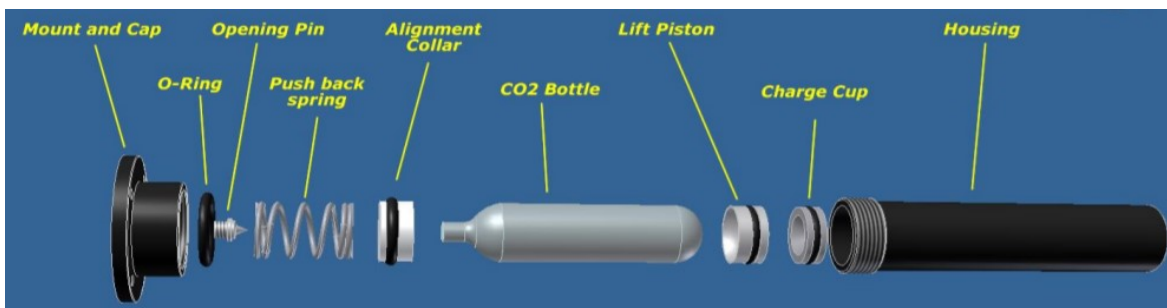
Figure 3.1. Tinder Rocketry Peregrine exploded view [38]. Copyright © 2016 Tinder Rocketry.

Carbon dioxide systems function cold and therefore do not create large amounts of heat, flame, and debris, unlike the hot gases and particles involved in pyrotechnic separation methods [5]. Therefore, flame-retardant cloths or "dog-barf" wadding is unnecessary to protect the rocket's interior, recovery system, and payloads. Currently, several commercial CO_2 model rocket kits are available. Commercial kits are reusable, and some kits include multiple housings for different-sized cartridges. Commercially available CO_2 kits are comprised of three components: a CO_2 cartridge, a cartridge housing to hold the cartridge with a small pyrotechnic charge, and a mechanism that punctures, loads, and seals the cartridge. The mechanism, as pictured in Figure 3.1, is triggered in flight by an onboard altimeter [38]. Commercial systems are prepared for flight by following the detailed manufacturer's instructions for each kit; this includes how to prepare and load the charge cup, mount the system to a bulkhead for use, and how to disassemble the system after use.

An advantage of CO_2 systems is that they are ideal for high altitude flights. Due to the low oxygen content, black powder burns inconsistently above 20,000 ft and does not burn above 50,000 ft, while commercially available CO_2 systems continue to work because the small pyrotechnic charge that is used to puncture the CO_2 cartridge is sealed and does not require the outside air to burn. In Figure 3.1, the small pyrotechnic charge would be placed inside the charge cup. Commercial CO_2 kits such as the Peregrine and RAPTOR made by Tinder Rocketry have been successfully functioned in test environments simulating 80,000 ft [38].

Carbon dioxide cartridges vary in size, but those sold specifically for model rocketry come with gas loads ranging from 8 to 85 g of CO_2. Different-sized CO_2 cartridges are used for various other applications such as airsoft guns and filling bicycle tires [39, 40]. These cartridges are identical to those sold for model rocketry and can be used in commercially available model rocket kits [40]. The amount of CO_2 necessary to properly pressurize the payload compartment of the rocket tube is calculated using the Ideal Gas Law in Eq. (3-2) or an online calculator such as those developed by the Nevada Aerospace Science Associates (NASSA) or the Huntsville Area Rocketry Association [15, 41]. The hand calculations or online calculators output a recommended black powder amount given the rocket's airframe diameter, the nosecone area, and the desired force on the nosecone as demonstrated in Eq. (3-1) and (3-2), and as seen in Figure 3.2. In these equations P represents the pressure in the rocket tube, F the desired force on the nosecone

bulkhead, A the area of the nosecone bulkhead the force is exerted on, V the volume of the payload compartment of the rocket body with diameter D and length L, R_{bp} the gas constant of black powder, and m_{bp} the quantity of black powder, in grams, necessary to properly pressurize the payload compartment of the rocket.

$$P = \frac{F}{A} \tag{3-1}$$

$$m_{\text{bp}} = \frac{P\,V}{R_{bp}\,T} \tag{3-2}$$

The accepted rule-of-thumb in model rocketry, as stated in the manufacturer's instructions of commercial CO_2 kits, is to multiply the recommended black powder ejection charge by five to arrive at the necessary amount of CO_2 to properly pressure the rocket body [38]. It can be demonstrated that preforming the calculation in Eq. (3-2) with the gas constant of CO_2, a predetermined volume, temperature, and necessary pressure, yields a reasonable answer for the necessary amount of CO_2 to properly pressurize the rocket body. The answer is reasonable because, as described in Section 3.2.1, it is similar to the answer produced by the online calculator [15, 41].

The desired pressure differential to jettison a nosecone from a 4 in diameter rocket is between 68947.6 to 103421 Pa (10 to 15 psi), based on experimental data from multiple model rocketry sources [5, 15, 41]. We applied the perfect gas law to calculate the necessary amount of black powder, which needs to be burned with air to produce gases that pressurize the payload compartment of the rocket, as shown in Eq. (3-3). We utilized the upper limit ejection charge pressure of 103421 Pa, P_t, the volume of the rocket tube, V_t, and the combustion gas constant, R_{bp}, and combustion gas temperature of FFFF (4FG) black powder, $T_{combustion}$, as specified in Table 3.9.

$$m_{CO_2} = \frac{P_t\,V_t}{R_{bp}\,T_{combustion}} \tag{3-3}$$

The 4FG black powder is a grade of black powder that is commonly used for model rocketry; the properties of the powder during combustion are dictated by the powder's composition and grain size and geometry [42, 43]. This is because black powder burns from the surface and therefore grains with different surface areas will burn at different rates, while densely packed grains cannot easily distribute the flames. This grade of black powder has a grain size of approximately 0.15-0.42 mm [42] and is a mixture of 75% nitrate, 15% charcoal, and 10% sulfur [43]. The chemical equation for the combustion of black powder in when introduced to air is shown in Eq. (3-4) [4].

$$10\ KNO_3 + 3\ S + 8\ C \rightarrow 2\ K_2CO_3 + 3\ K_2SO_4 + 6\ CO_2 + 5\ N_2 \qquad (3\text{-}4)$$
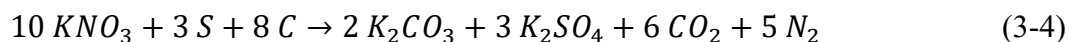
The result is approximately 1.98 g. Therefore, the necessary amount of CO_2 to pressure the airframe of the rocket is approximately 9.88 g, which can be rounded up to the next available cartridge size, 12 g.

This result was compared with the Nevada AeroSpace Science Associates (NASSA) online ejection charge calculator [41]. The online ejection charge calculator is intended to assist in properly sizing black powder ejection charges, which provides more information about properly sizing CO_2 cartridges. NASSA provides a table of recommended pressures for specific airframe diameters and the desired force on the nosecone as seen in Table 3.1. In the top row, the desired values of the force on the nosecone are listed in lb_f, and in the columns corresponding to each force are the necessary pressures needed to produce that force for a given airframe diameter. When the team entered the rocket tube diameter, length, and desired ejection pressure into the NASSA calculator the necessary black power is 2.33 g, which indicates 11.65 g of CO_2 are necessary. The results from the NASSA calculator and the team's results indicate that a 12 g CO_2 cartridge would properly pressurize the payload compartment. It is unclear exactly how NASSA members determined the desired forces to properly eject the nosecone. We were also unsure if the necessary force refers to the absolute pressure generated in the rocket tube, or the difference in pressure between the rocket tube and the pressure produced by air pushing onto the nosecone (i.e. dynamic pressure) during flight. Therefore, we analyzed the CO_2 flow to better understand the information provided by NASSA and determine the required force and necessary CO_2 using a predetermined

method. These values, while they do indicate accuracy of either method, are a point of comparison for the values we tabulated in Section 3.3.1.

Table 3.1. Airframe diameter and desired force [41].

Airframe Diameter	100 lb$_f$	150 lb$_f$	200 lb$_f$	250 lb$_f$
	Pressure [psi]			
2.6"	19	28	38	47
4.0"	8	12	16	20
6.0"	3.5	5.3	7.0	8.8
7.5"	2.3	3.4	4.5	5.7

The mass flow of the CO_2 flow, as well as the pressure, density, and temperature, change with time. The variation in the characteristics of the CO_2 flow properties with respect to time must be understood to know when the separation event should be signaled to occur. We solved a system of differential equations, including Eq. (3-5), to estimate the time needed to pressurize the payload bay to the point where the nosecone will separate. This time represents an estimate of the time-lag between the command to initiate separation and when the nosecone is ejected [44]. The mass flow rate of CO_2 out of the cartridge, $\frac{dm_{CO_2}}{dt}$, is modeled using Eq. (3-5), which assumes the flow is choked.

The CO_2 flow occurs in three stages distinct stages [45, 46] which must be analyzed to understand the transient properties of the flow out of a cartridge into a rocket body as depicted in Figure 3.2. We focused only on the first stage of flow for this analysis. The mass flow of CO_2 during choked flow (the first stage) can be analyzed using Eq. (3-5) and isentropic relations where m_{CO_2} represents the mass of CO_2 during this stage, A_e the exit area of the CO_2 cartridge, P_c the pressure in the cartridge, T_c the temperature in the cartridge, γ_{CO_2} the ratio of the specific heats of CO_2, and R_{CO_2} the gas constant of CO_2.
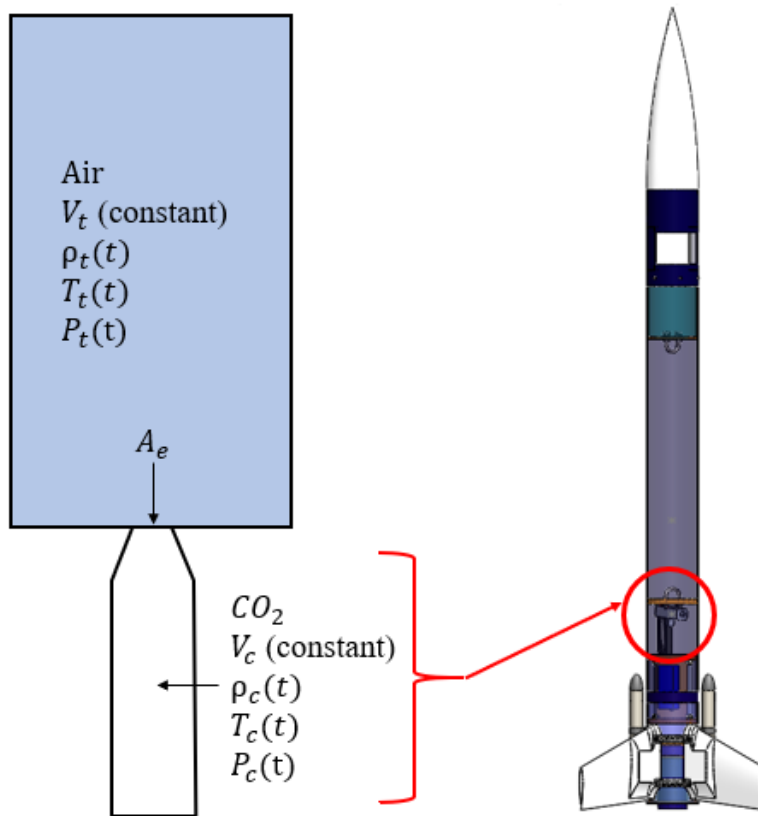
Figure 3.2. Model representation of pressurization system with carbon dioxide flowing into sealed rocket body and placement in completed rocket.

$$\frac{dm_{CO_2}}{dt} = \frac{(-A_e\,P_c(t))}{\sqrt{T_c(t)}}\sqrt{\frac{\gamma_{CO_2}}{R_{CO_2}}}\left(\frac{\gamma_{CO_2}+1}{2}\right)^{\left(\frac{-\gamma_{CO_2}+1}{2(\gamma_{CO_2}-1)}\right)} \tag{3-5}$$

A custom CO_2 stage separation system is not trivial to design or analyze, but commercially available kits show that the system can be developed and used effectively in model rockets. The creation of custom CO_2 kits is possible and innovative, due to the popularity of CO_2 stage separation for high altitude launches, safety, and limited debris.

3.1.2 Electromagnetic Separation

The WARRIORS projects were a series of MQPs from 2006 to 2008. They used the idea that a magnetic field can be used to create a force to separate the boosters. This unorthodox method delves into new technological territory where magnets are employed instead of pyrotechnics. Proper analysis is required to design a successful system. With a permanent magnet on the boosters, and a ferromagnetic metal on the main body, the boosters can be held on with this interaction. When ejection is required, a current is run through a coil to apply a field. This field is designed to reverse the magnetic field inside the ferromagnetic metal to cause a repulsion. This repulsion would lead to a successful ejection.

The goal of the first and second WARRIORS projects in 2005 and 2006 was to create unique solutions for model rocketry systems [21, 47]. One aspect that showed creative problem solving was in the stage separation system. The WARRIORS I project implemented an electromagnetic stage separation system that was continued and modified by the WARRIORS II project. As explained in section 1.1.2, model rocketry staging can appear in either series or parallel. Both WARRIORS I and II pursued parallel staging to move away from traditional model rocketry staging techniques [5]. It is more common for rockets to use series staging because of its simplicity [5]. Parallel staging provides more complicated engineering problems, nevertheless it brings benefits to the performance of the rocket. Traditionally, once these booster rockets have finished burning, they would be ejected using pyrotechnics. The WARRIORS projects decided to change the method of booster separation, and after researching potential ideas, the decision was made to use an electromagnetic mechanism for stage separation. There are always challenges when creating innovative technologies. The WARRIORS I project encountered insufficient current and a flight failure [21]. However, for the most part, integration was completed successfully, showing the feasibility of this method. This design allowed for multiple tests, reliable results, and cleaner separation due to the lack of pyrotechnic debris.

As a result, the WARRIORS II team wanted to improve the design [47]. The second team decided to alter the system to improve the performance of the rocket by lowering mass. The amount of weight in the stage separation system in the WARRIORS I design was reduced, allowing the main rocket body to reach a higher altitude. Different power sources were placed in each booster instead of entirely in the main stage of the rocket. During the construction of this design, the team

ran into obstacles caused by the additional electronics in the boosters and volume and configuration constraints. The WARRIORS II project, however, was not able to conduct system testing and as a result, this design was not able to be field-tested.

One property of the magnetic field is that it decreases in strength over distance. If the magnet is a certain distance from the center of the electromagnet, the residual magnetism changes, in which case using Eq. (3-6) would allow calculation on the surface of the permanent magnet [21].

$$B_m \approx \frac{B_r}{2} \left[\frac{L_m}{\sqrt{R^2 + L_m{}^2}} \right] \tag{3-6}$$

In Eq. (3-6), L_m is length of the magnet and R is the radius of the magnet. This equation applies to cylindrical magnets.

Permanent magnets have a high ratio of flux density to unit mass which cannot be controlled [47, 48]. An electrically generated field must be employed to manipulate the magnetic field. This can be accomplished using a solenoid, a technology that is commonly used for manipulating magnetic fields. A solenoid is a coil of wires wrapped around a ferromagnetic core. When an electric current is run through the wire, a controlled magnetic field is created.

Using both the permanent magnet and the electromagnet allows one to construct a functional separation system. When the magnet and the ferrous metallic core are nearby, they are attracted to each other by the magnet's innate flux [47]. By running a current through the solenoid, a magnetic field can be created to temporarily to create a repulsive force. This force will separate the booster form the core booster. We based much of our analysis on relations from the WARRIORS I project [21].

Eq. (3-7) and (3-8) are used to find the maximum current needed in a circuit to generate the magnetic field flux required.

$$p_{1,2} = -\frac{2}{2L} \pm \sqrt{\left(\frac{R}{2L}\right)^2 - \frac{1}{CL}} \tag{3-7}$$

$$i(t) = -\frac{U_1}{L}\left(\frac{1}{p_1 - p_2} e^{p_1 t} + \frac{1}{p_1 - p_2} e^{p_2 t}\right) \tag{3-8}$$

In Eq. (3-7), R represents the resistance, L represents the inductance, and C is the capacitance. In Eq. (3-8), U_1 represents the voltage and t is the time. These equations are incredibly are used to find the time varying current going through an electric system given circuit parameters.

For this project, we planned to enhance the success of the original projects. Considering that an electromagnetic separation system has been used in a previous project, improvements were planned based on the previous teams' recommendations. The focus for the stage separation team, was to increase the reliability of the booster separation system. WARRIORS I validated the feasibility of the system, proving it to be a highly successful model. The WARRIORS II project shed light that systems can always be improved. By building on the foundations of these previous projects, an improved electromagnetic system provides the rocket with a reliable option.

3.2 Methodology

After we completed a literature review on methods of stage separation, we developed a list of low, medium and, high risk options for stage separation methods that could be used on the rocket. The low risk option was to use a single stage rocket with no side boosters and a standard black powder charge to separate the nosecone from the rocket body. The medium risk option was to create a rocket with one main stage and four side boosters and to develop a custom CO_2 stage separation system for separating the nosecone from the rocket body. This option would also include creating an electromagnetic separation system for the side boosters on the rocket that would improve on aspects present in the WARRIORS I and II projects [21, 47]. Lastly, the high-risk option was to create a CO_2 separations system that would separate both the nosecone and the side boosters from the rocket. The medium risk option was viewed as the most feasible choice for this project and thus was selected for development. We were able to state the goals of each stage

separation system after deciding to pursue a CO_2 separation system and an electromagnetic booster separation system.

- Design and build a successful CO_2 separation system and an electromagnetic separation system that is reusable, reliable, and is less expensive than commercial systems
- Jettison the nosecone and rocket booster successfully during flight

3.2.1 Carbon Dioxide (CO_2) Separation Methodology

CO_2 Flow Calculations

We calculated the amount of CO_2 necessary to properly pressurize the payload compartment of the rocket tube. The mass flow of the CO_2, as well as the pressure, density, and temperature, varies with time. This section presents our methodology to calculate the final pressure in the rocket tube and the time to reach this point, provided by a CO_2 stage separation system. A sample calculation using this design methodology is presented in section 3.3.1. We analyzed the mass flow out of the cartridge and into the payload section of the airframe with respect to time to estimate the time needed for the CO_2 cartridge to deplete enough of its contents to jettison the nosecone and the pressure at that time point. We applied isentropic relations to the CO_2 in the cartridge and CO_2 – air mixture in the rocket tube to determine the properties inside each volume. We preformed the calculation under the assumptions that the gas properties vary only with time (i.e. a 0D model), CO_2 can be treated as an ideal gas with a compressibility factor, and the flow is adiabatic, because the discharge is rapid. The additional assumption of ideal, reversible, flow allows us to apply the isentropic relations to make the calculations tractable with the understanding that this ideal model will provide an approximate result. The cartridge and payload bay are represented by separate, fixed, control volumes with an initial pressure that is calculated given the volume of the cartridge and the CO_2 mass as depicted in Figure 3.2. We solved an ordinary differential equation, Eq. (3-5), to estimate the time needed to pressurize the payload bay to the point where the nosecone will separate [44]. This time represents an estimate of the time-lag between the command to initiate separation and when the nosecone is ejected. The CO_2 flow must be considered in three stages to analyze the transient properties of the flow out of a cartridge into a rocket body [45]. All the parameters used in the model described in this section are defined in Table 3.2.

Table 3.2. Nomenclature and units for CO₂ transient flow model.

Variable	Name	Units
g	Gravitational Constant	$\frac{m}{s^2}$
R	Universal Gas Constant	$\frac{J}{mol\,K}$
A_e	Cartridge Exit Area	m^2
T_{c0}	Initial Temperature in Cartridge	K
V_c	Volume of Cartridge	m^3
P_{c0}	Initial Pressure in Cartridge	Pa
R_{CO_2}	Gas Constant of CO_2	$\frac{J}{kg\,K}$
$R_{CO_2,avg}$	Average Gas Constant of CO_2, over pressure range	$\frac{J}{kg\,K}$
γ_{CO_2}	Ratio of Specific Heats, CO_2	$\sim$
$\gamma_{CO_2,avg}$	Average Ratio of Specific Heats, CO_2 over pressure range	$\sim$
$C_{p_{CO_2}}$	Specific Heat, Constant Pressure of CO_2	$\frac{J}{kg\,K}$
$C_{v_{CO_2}}$	Specific Heat, Constant Volume of CO_2	$\frac{J}{kg\,K}$
$m_{CO_2,0}$	Initial mass of CO_2 in cartridge	kg
MM_{CO_2}	Molar Mass of CO_2	$\frac{kg}{mol}$
n_{CO_2}	Quantity of CO_2	mol
Z_{CO_2}	Compressibility Factor of CO_2	$\sim$
$\rho_{CO_2,0}$	Initial Density of CO_2	$\frac{kg}{m^3}$
V_t	Volume of Rocket Tube	m^3
T_{t0}	Initial Temperature in Tube	K
V_t	Volume of Rocket Tube	m^3
P_{t0}	Initial Pressure in Rocket Tube	Pa
m_{t0}	Initial mass of Air in Rocket Tube	kg
ρ_{t0}	Initial Density of Air in Rocket Tube	$\frac{kg}{m^3}$
R_{air}	Gas Constant of air	$\frac{J}{kg\,K}$
γ_{air}	Ratio of Specific Heats, air	$\sim$
$C_{p_{air}}$	Specific Heat, Constant Pressure of air	$\frac{J}{kg\,K}$
$C_{v_{air}}$	Specific Heat, Constant Volume of air	$\frac{J}{kg\,K}$
m_{air}	Initial mass of air in cartridge	kg
MM_{air}	Molar Mass of air	$\frac{kg}{mol}$
n_{air}	Quantity of air	mol
$MM_{mixture}$	Average Molar Mass of air-CO_2 mixture	$\frac{kg}{mol}$
$R_{mixture}$	Average Gas Constant of air-CO_2 mixture	$\frac{J}{kg\,K}$
$C_{p,mixture}$	Average Specific Heat, Constant Pressure, of air-CO_2 mixture	$\frac{J}{kg\,K}$
$\gamma_{mixture}$	Average Specific Heat Ratio of air-CO_2 mixture	$\sim$

$P_{critical}$	Critical Pressure Ratio	~
P_t	Ejection Charge Pressure	Pa
$P_{t,est}$	Estimated pressure in rocket tube during unchoked, compressible flow	Pa
m_{mix}	Amount of air-CO_2 mixture in rocket tube	kg
$T_{isothermal}$	Estimated isothermal temperature for unchoked, compressible flow	K
R_{bp}	Combustion Gas Constant of FFFF Black Powder	$\frac{J}{kg\ K}$
$T_{combustion}$	Combustion Gas Temperature of FFFF Black Powder	K

The first stage of flow corresponds to the choked flow of CO_2 out of the cartridge into the rocket body. The first stage ends when the critical pressure ratio for CO_2 is reached and therefore the ratio of the pressure in the cartridge to the pressure in the rocket tube is greater than 1.83. The model consists of a differential equation used to determine the changing mass of the CO_2 out of the cartridge and into the payload compartment. The differential equation was solved numerically over a timespan to calculate the total time (to the desired pressurization level) and the density, temperature, and pressure of CO_2, along with the initial density and mass of CO_2 in the cartridge and the rocket tube. The pressurized CO_2 is stored mostly as a liquid and therefore the CO_2 in the cartridge is both a liquid and a gas. The pressure of the CO_2 cannot exceed the vapor pressure of CO_2 at 298 K and therefore, the vapor temperature is taken as the initial pressure, P_{c0}, of the CO_2. We expect that there would be a period, that is neglected in this analysis, where the pressure in the cartridge remains constant at the vapor pressure rather than decreasing initially from it, to reflect the phase change from liquid to gas that occurs at the vapor pressure.

Initially, we calculated the properties of the 12 g of CO_2 inside the cartridge with a known volume and temperature. The CO_2 cartridge depletes from an initial pressure to atmospheric pressure if it depletes completely. The specific heats of CO_2, with constant pressure C_{pCO_2} and constant volume C_{vCO_2}, are available through the National Institute of Standards and Technology (NIST) as seen in Appendix F. The range of specific heats across the pressure range are used to calculate the specific heat ratio, γ_{CO_2}, and the gas constant, R_{CO_2}, as it changes with pressure during the numerical calculation of the mass flow rate of the CO_2. A compressibility factor is necessary because CO_2 is not an ideal gas at the high pressures during most of the emptying of the chamber; this must be accounted for in the analysis to get an accurate result [49]. A compressibility factor of 1 corresponds to an ideal gas. At each timestep, we used pressure and temperature data from NIST [50], as seen in Appendix F, and the Van der Waals equation of state to calculate the variable

compressibility factor, Z_{CO_2}, of CO₂. The MATLAB® code to calculate the compressibility factor was created by Chad Greene [51].

The initial properties of the CO₂ are input arguments to Eq. (3-5), which is repeated below, for the mass flow of the first stage of flow, $\frac{dm_{CO_2}}{dt}$, where the flow of CO₂ is choked. In Eq. (3-5), m_{CO_2} represents the mass of CO₂ during the time range, A_e the exit area of the CO₂ cartridge, P_c the pressure in the cartridge, T_c the temperature in the cartridge, γ_{CO_2} the ratio of the specific heats of CO₂, and R_{CO_2} the gas constant of CO₂. We analyzed the mass flow of CO₂ out of the cartridge to determine the total time to deplete the cartridge [15]. We substituted the isentropic relations, Eq. (3-9) through (3-11), for density, ρ_c, temperature, T_c, and pressure, P_c, into Eq. (3-5) to make the differential equation dependent only on time and the mass of CO₂ prior to solving Eq. (3-5) numerically. The density, temperature, and pressure of the CO₂ over the timespan are then calculated using the isentropic relations and the calculated values of mass flow rate.

$$\frac{dm_{CO_2}}{dt} = \frac{(-A_e\,P_c(t))}{\sqrt{T_c(t)}}\sqrt{\frac{\gamma_{CO_2}(P_c)}{R_{CO_2}(P_c)}}\left(\frac{\gamma_{CO_2}(P_c)+1}{2}\right)^{\left(\frac{-\gamma_{CO_2}(P_c)+1}{2(\gamma_{CO_2}(P_c)-1)}\right)} \tag{3-3}$$

$$\rho_c(t) = \frac{m_{CO_2}}{V_c} \tag{3-9}$$

$$T_c(t) = T_{c0}\left(\frac{\rho_c(t)}{\rho_{c0}}\right)^{\gamma_{CO_2}-1} \tag{3-10}$$

$$P_c(t) = Z_{CO_2}P_{c0}\left(\frac{\rho_c(t)}{\rho_{c0}}\right)^{\gamma_{CO_2}} \tag{3-11}$$

To find the final pressure in the rocket tube at the end of the choked flow regime, we first determined the properties of the air initially in the rocket tube, as well as the average fluid properties of the CO_2 – air mixture in the rocket tube during CO_2 depletion. We calculated the average specific heat ratio, $\gamma_{mixture}$, and gas constant, $R_{mixture}$, of the mixture using the known properties of CO_2 and air when half of the CO_2 was depleted. The mass flow rate out of the cartridge is equal to the mass flow rate into the rocket tube. Therefore, Eq. (3-12) was used to describe the changing fluid mass inside the rocket tube during the first stage of choked flow where the initial mass of air in the rocket tube and the initial amount of CO_2 inside the cartridge is accounted for with the initial mass in the rocket tube, m_{t0}. The quantity m represents the total mass of gas, both CO_2 and air, in the rocket body and its change with time, m_{tCO_2} represents the mass of the carbon dioxide and air gas mixture during the timespan, P_t the pressure in the tube, and T_{t0} the initial temperature in the tube.

$$\frac{dm_t}{dt} = -\frac{dm_{CO_2}}{dt} \tag{3-12}$$

Then, we applied isentropic relations to find the pressure of the mixture inside the rocket tube, as seen in Eq. (3-13) through (3-15). In Eq. (3-13) through (3-15), ρ_t represents the density of gas in the tube, γ_{mix} the ratios of specific heats of the gas mixture found through calculating the specific heat of the mixture $C_{p,mix}$, T_t the temperature in the tube, and R_{mix} the gas constant of the gas mixture calculated using the mole numbers for the mixture constituents. It should be noted that the pressure of the CO_2 - air mixture is calculated using the Ideal Gas Law and not the Van der Waals equation. This is because the Van der Waals constants a and b are not defined for a changing mixture, and the pressure in the tube is not high enough for the gas to differentiate from the Ideal Gas Law. Therefore, the Van der Waals equation is not needed.

$$\rho_t(t) = \frac{m_t(t)}{V_t} \tag{3-13}$$

$$T_t(t) = T_{t0} \left(\frac{\rho_t(t)}{\rho_{t0}} \right)^{\gamma_{mixture}-1} \tag{3-14}$$

$$P_t(t) = P_{t0} \left(\frac{\rho_t(t)}{\rho_{t0}} \right)^{\gamma_{mix}} \tag{3-15}$$

We did not estimate the second and third stage of flow because it was unnecessary for the nosecone to jettison. A sample calculation for the CO_2 transient flow model is provided in Section 3.3.1. The methodology to calculate the time and pressure following partial depletion of the CO_2 cartridge is outlined in Table 3.3. In this table, the first column lists the equation used to calculate the given parameter. The second column lists the parameters used in the calculation for that step, that are either assumed or known from another source such as a reference. The third column lists parameters that appear in the equation that have been calculated in a prior step. The fourth column lists the values that are unknown in the equation. The fifth column lists the number for the source (from the literature review), where the equation was found, with numbers corresponding the References Section of this report. The last column lists the Equation number (if any) that identities the equation in the original source.

Table 3.3. CO₂ transient flow calculations.

Equation	Units	Given/ Assumed	Previously Calculated	Unknowns	Reference	Equation Number in Given Reference
CO₂ parameters and physical constants						
$n_{CO_2} = \dfrac{m_{CO_2,0}}{MM_{CO_2}}$	mol	$m_{CO_2,0}$, MM_{CO_2}	~	n_{CO_2}	~	~
$\gamma_{CO_2}(P_c) = \dfrac{C_{p_{CO_2}}}{C_{v_{CO_2}}}$	~	$C_{p_{CO_2}}$, $C_{v_{CO_2}}$	~	γ_{CO_2}	[52]	(8)
$R_{CO_2}(P_c) = C_{p_{CO_2}} - C_{v_{CO_2}}$	$\dfrac{J}{kg\,K}$	$C_{p_{CO_2}}$, $C_{v_{CO_2}}$	~	R_{CO_2}	[52]	(7)
$Z_{CO_2}(P_c) = 1 + \dfrac{bP_c}{R_{CO_2}T_c}$	~	P_c, V_c, T_c	R_{CO_2}	Z_{CO_2}	[53]	pg. 8

CO₂ mass flow rate ordinary differential equation						
$$\frac{dm_{CO_2}}{dt} = \frac{(-A_e * P_c(t))}{\sqrt{T_c(t)}} \sqrt{\frac{\gamma_{CO_2}(P_c)}{R_{CO_2}(P_c)}} \left(\frac{\gamma_{CO_2}(P_c)+1}{2}\right)^{\left(\frac{-\gamma_{CO_2}(P_c)+1}{2(\gamma_{CO_2}(P_c)-1)}\right)}$$	$\frac{kg}{s}$	$A_e,$ $\gamma_{CO_2,avg}$	P_c, T_c, R_{CO_2}	$\frac{dm_{CO_2}}{dt}$	[44]	~
$\rho_c(t) = \frac{m_{CO_2}}{V_c}$	$\frac{kg}{m^3}$	m_{CO_2}, V_c	~	$\rho_c(t)$	[54]	~
$T_c(t) = T_{c0} \left(\frac{\rho_c(t)}{\rho_{c0}}\right)^{\gamma_{CO_2}-1}$	K	T_{c0}, ρ_{c0}	$\rho_c, \gamma_{CO_2,avg}$	$T_c(t)$	[54]	~
$P_c(t) = Z_{CO_2} P_{c0} \left(\frac{\rho_c(t)}{\rho_{c0}}\right)^{\gamma_{CO_2}}$	Pa	~	$Z,$ $R_{CO_2,avg},$ $\rho_c(t),$ $T_c(t)$	$P_c(t)$	[54]	~
CO₂ – air mixture in rocket tube						
$m_{t0} = m_{air} = \frac{P_{t0} V_t}{R_{air} T_{t0}}$	kg	$P_{t0}, V_t,$ R_{air}, T_{t0}	~	m_{t0}	~	~
$n_{air} = \frac{m_{air}}{MM_{air}}$	mol	MM_{air}	m_{air}	n_{CO_2}	~	~
$\rho_{t0} = \frac{m_{t0}}{V_t}$	$\frac{kg}{m^3}$	V_t	m_{t0}	ρ_{t0}	~	~
$MM_{mixture} = \frac{\left(\frac{n_{CO_2}}{2} MM_{CO_2} + n_{air} MM_{air}\right)}{n_{total}}$	$\frac{kg}{mol}$	$MM_{CO_2},$ MM_{air}	$n_{CO_2}, n_{air},$ n_{total}	$MM_{mixture}$	[7]	(5-5)
$R_{mixture} = \frac{\boldsymbol{R}}{MM_{mixture}}$	$\frac{J}{kg\,K}$	$\boldsymbol{R}$	$MM_{mixture}$	$R_{mixture}$	~	~
$C_{p,mixture} = \frac{\left(\frac{n_{CO_2}}{2} C_{p,CO_2\,tube} + n_{air} C_{p,air}\right)}{n_{total}}$	$\frac{J}{kg\,K}$	$C_{p,CO_2\,tube},$ $C_{p,air}$	$n_{CO_2}, n_{air},$ n_{total}	$C_{p,mixture}$	[7]	(5-6)
$\gamma_{mixture} = \frac{C_{p,mixture}}{C_{p,mixture} - 1}$	~	~	$C_{p,mixture}$	$\gamma_{mixture}$	[7]	(5-7)
$\frac{dm_t}{dt} = -\frac{dm_{CO_2}}{dt}$	$\frac{kg}{s}$	~	$m_{t0}, \frac{dm_{CO_2}}{dt}$	$\frac{dm_t}{dt}$	~	~
$\rho_t(t) = \frac{m_t(t)}{V_t}$	$\frac{kg}{m^3}$	V_t	$m_t(t)$	$\rho_t(t)$	~	~
$T_t(t) = T_{t0} \left(\frac{\rho_t(t)}{\rho_{t0}}\right)^{\gamma_{mixture}-1}$	K	T_{t0}	$\rho_t(t), \rho_{t0},$ $\gamma_{mixture}$	$T_t(t)$	[54]	~
$P_t(t) = P_{t0} \left(\frac{\rho_t(t)}{\rho_{t0}}\right)^{\gamma_{mix}}$	Pa	~	$R_{mixture},$ $\rho_t(t), T_t(t)$	$P_t(t)$	[54]	~
$P_{critical} = \frac{P_c}{P_t} \geq 1.83 \; (for\; choked\; flow)$	~	~	P_c, P_t	$P_{critical}$	[54]	~

We experimentally determined the necessary force to remove the nosecone to determine if the pressure difference created by the depletion of the 12 g CO_2 cartridge would be enough to pressurize the payload compartment and jettison the nosecone. The procedure for this test is described in Section 3.3.1. The force due to atmospheric pressure was calculated using the relationship between atmospheric pressure and the area of the bulkhead. This force is approximately 821.5 N. We assumed that the rocket is airtight and is therefore not equilibrated to the atmosphere throughout the flight. Therefore, the necessary internal pressure to jettison the nosecone is the force due to atmospheric pressure plus the pressure to overcome the friction of the nosecone. The force of friction on the nosecone was determined to be 12.5 N from a static experiment to remove the nosecone. We assumed that at separation the rocket is stationary at apogee and therefore, the only force the nosecone must overcome is the friction force. We used the relation between force and bulkhead area to find the gauge pressure the nosecone exerts to be 1542 Pa. Therefore, the necessary pressure to jettison the nosecone is 102867 Pa. Assuming the nosecone will be jettisoned at a pressure differential of 103421 Pa (15 psi) [15, 41], we can compare the calculated pressure differential to determine if the nosecone will be properly jettisoned.

Carbon Dioxide (CO_2) System Design and Assembly

Following our literature review of commercially available CO_2 separation kits, we established three objectives for design and manufacture of a custom CO_2 separation system. The custom system must be easily reloadable for multiple launches, less expensive than commercially available CO_2 separation kits, and should not involve the use of pyrotechnics to function. With these parameters set forth, we designed and manufactured a custom CO_2 separation system.

One of our first inspirations for designing a reloadable CO_2 system came from CO_2-powered airsoft guns. A typical CO_2 powered airsoft gun functions by using a CO_2 cartridge that has been inserted into either the gun itself or its removable magazine. A screw is then turned that presses the CO_2 cartridge into a puncturing device thus creating an airtight seal around the CO_2. The airtight seal enables the cartridge to serve as a gas reservoir. The gas is then released from the gas reservoir through the action of a firing pin pushing into a release button with a relatively high

force. For the first iteration of the custom CO_2 system design, we created a housing for the CO_2 cartridge that resembled a magazine from an airsoft gun, as seen in Figure 3.3.
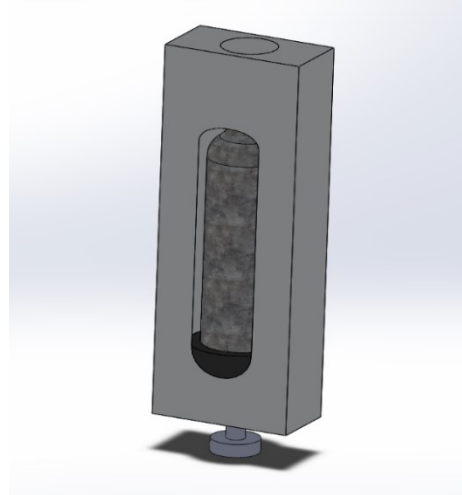
Figure 3.3. CO₂ separation early prototype. For scale, the long dimension of the rectangular housing is 113 mm.

A mechanism to puncture the cartridge would be located at the top of the housing and as with the airsoft gun, the puncture would create a gas reservoir from the punctured and sealed CO_2 cartridge. This would allow the CO_2 cartridge to be punctured before the rocket was launched and avoid the use of any pyrotechnics midflight. The gas would be released by activating a solenoid on the top of the housing. We researched solenoids that could hold the minimum pressure, approximately 850 psi [55], needed to store the CO_2 and these options were too large to fit inside the diameter of the rocket body and more expensive than the existing commercially available CO_2 kits. This idea was ultimately not selected due to these design uncertainties and potential problems relating to how the gas was released. One concept we considered to avoid using a solenoid to release the gas was to use a 0.25 in ball valve turned by a servo. This would solve both the cost and size problems of using a solenoid but was impractical because a ball valve requires a substantial amount of torque to open, more than a small servo could generate. Therefore, this option was rejected as well.

After identifying these potential problems with the initial iterations of the custom CO_2 separation system, we decided that both the simplest and most cost-effective way to store and release the CO_2 for the separation system was to buy an inexpensive magazine for an airsoft hand gun and remove all parts not related to the gas system. Then, we developed a firing mechanism to trigger the CO_2 flow and turn the magazine into a separation system. Unlike an airsoft gun that uses a firing pin to forcefully tap the release button located on the side of the magazine, the firing mechanism would need to hold in the release button until the cartridge was emptied. We considered several different iterations of this mechanism until the "final" design was selected. The first iteration involved placing a linear actuator on a bulkhead next to the release button of the magazine inside of the rocket which, when triggered by the onboard computer, would extend and press the button. The design was flawed because the force required to hold down the release button was experimentally determined to be 12-15 lbs This force was greater than the maximum force values attainable from the micro-linear actuators commercially available that could fit horizontally inside of the rocket body. As a result, a firing mechanism was designed that would have the same functionality as a linear actuator but would also be able to impart the required force.

The final iteration of the firing mechanism consisted of seven key parts: the housing, a 0.25 in ACME threaded rod with 16 turns per in., a 0.5 in. nut, an electric motor with a stall torque of 20 oz-in and a maximum speed of 460 rpm, a coupler, two grub screws, and an actuator to make contact with the release button as seen in Figure 3.4. We selected the threaded rod and electric motor for the firing mechanism based on initial calculations made to insure the nut could travel approximately 0.125 in in a time of 0.5 s and imparting 50 N of force. This distance is the release needed to fully press the button. We calculated the necessary rotational speed of the motor in rpm and a motor torque of 5 oz-in was used as an initial estimate. The total rotational speed is calculated to be 240 rpm using the following equality that is then converted into rpm:

$$\left(\frac{2\ rev}{0.5\ s}\right) = \left(\frac{4\ rev}{x\ s}\right)$$

Originally, a motor with a maximum speed of 270 rpm was selected for the firing mechanism, however due to the unavailability of the 270-rpm motor, we selected a 460-rpm motor.
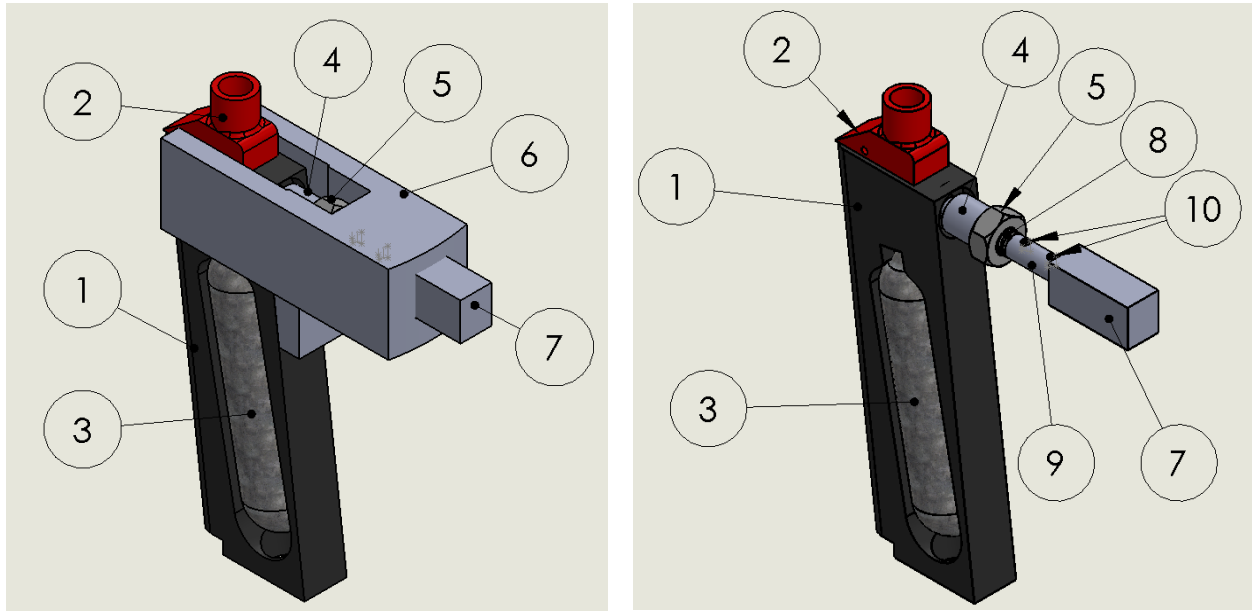
Figure 3.4. Final CO_2 assembly, with housing (left), final CO_2 assembly, without housing (right).

Table 3.4. CO_2 separation assembly parts list.

Item No.	Part	Qty.
1	CO_2 magazine	1
2	Magazine spout	1
3	12 g CO_2 cartridge	1
4	Actuator	1
5	Carbon Steel Acme Hex Nut Right Hand, ¼"-16	1
6	Housing (not shown)	1
7	460 rpm Micro Gear Motor	1
8	Carbon Steel Acme Lead Screw Right Hand, ¼"-16	1
9	Coupler	1
10	18-8 Stainless Steel Cup-Point Set Screw 2-56 Thread, 1/8" long	2

The final CO_2 assembly can be seen in Figure 3.4 and the corresponding components are identified in Table 3.4. We turned down the threaded rod (8) at one end using a lathe to make it the same diameter as the motor shaft (7). Then, the machined threaded rod and the motor shaft were put inside of opposite ends of the coupler (9), and two set screws (10) were put into tapped holes in the coupler to secure the motor shaft and threaded rod. The nut (5) was then screwed onto the threaded rod and the actuator (4) was attached to the nut.
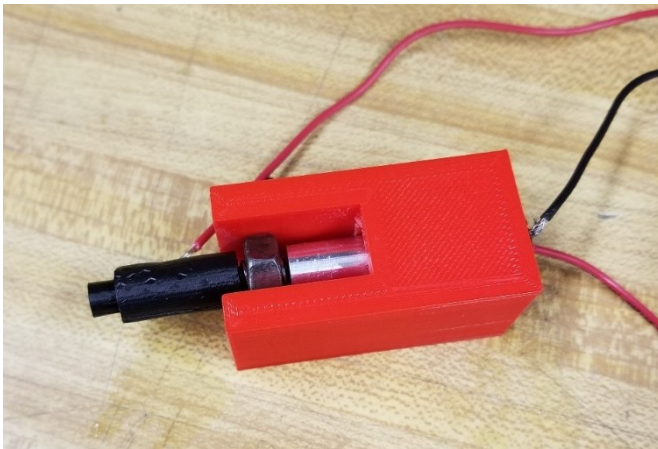
Figure 3.5. CO₂ separation system prototype assembly.
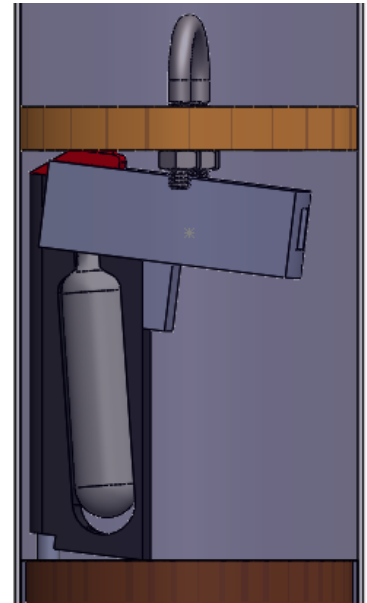
Figure 3.6. CO₂ separation system assembly installed on airframe bulkhead inside model rocket.

The nut is kept from rotating by the housing (6) of the mechanism when the electric motor (7) rotates the threaded rod. The nut then causes the actuator to move forward and press the release button on the magazine. Figure 3.5 illustrates a prototype design of the separation system. The firing mechanism is attached to a bulkhead inside of the rocket body to ensure that it is in line with the release mechanism as seen in Figure 3.6.

Material Testing

We sought to analyze the material properties of the custom-made, polylactide (PLA) components using SOLIDWORKS®. Two major components of the firing system, the housing and

the actuator, were rapidly prototyped (3D-printed) out of PLA. However, the material properties of the 3D-printed materials do not have linear or well-documented properties, because of different possible levels of PLA infill and printing orientations. Therefore, we did not have the material properties to use in the SOLIDWORKS® simulation. The simulation treats the selected part as a solid chunk (100% infill) of the specified material. In 3D printing, the infill percentage, layer height, and wall thicknesses are all variables that the user can change. What specific orientation the part is printed in also influences the structural integrity of the part. As a result of these variables, it was decided that material testing should be conducted for 3D printed PLA with differing infill percentages, layer heights, and wall thicknesses. The goal of the tensile testing was to obtain the young's modulus and tensile strength of the specimens. To do this, twelve specimens were created to an ASTM D638 standard [56] so that tensile testing could be conducted using a universal testing material testing machine known as an Instron [57]. These specimens have a "dog bone" shape to them and are 7 mm thick. The twelve specimens were split into six groups of two as seen in Table 3.5, and Figures 3.7 and 3.8. The first two groups were printed using the default infill percentages, layer heights, and wall thicknesses for an Ultimaker 3 3D printer.

Figure 3.7. Group one specimen printing configuration (thin side up).

Figure 3.8. Group two specimen printing configuration (large side up).

Group one was printed with the thin edge of the specimen facing up while group two was printed with the large side of the specimen facing upward. The next two groups were printed using double the default settings and the pattern of shifting which edge was printed facing upward was continued. The last two groups were printed using the default settings cut in half and again the orientation pattern was continued.

Table 3.5. Material testing specimen characteristics.

Group	Printer Settings	Orientation
1	Layer Height: 0.15 mm Wall Thickness: 1.3 mm Infill Density: 20%	Thin side up
2	Layer Height: 0.15 mm Wall Thickness: 1.3 mm Infill Density: 20%	Large side up
3	Layer Height: 0.3 mm Wall Thickness: 2.6 mm Infill Density: 40%	Thin side up
4	Layer Height: 0.3 mm Wall Thickness: 2.6 mm Infill Density: 40%	Large side up
5	Layer Height: 0.075 mm Wall Thickness: 0.65 mm Infill Density: 10%	Thin side up
6	Layer Height: 0.075 mm Wall Thickness: 0.65 mm Infill Density: 10%	Large side up

3.2.2 Electromagnetic Separation Methodology

The WARRIORS I project started the effort to innovate booster stage separation using electromagnets [21]. As a result, developing a similar electromagnetic system, which focuses on optimization and streamlined performance, would further this technology and make it more straightforward for future project teams to create additional systems. The use of this system is considered moderately risky because there were failures during the WARRIORS I launch, therefore we wanted to assure the dependability of the system. We used a block diagram to organize the calculations and coding for the electromagnetic system as seen in Table 3.6. The variable and units used are also shown in Table 3.7.

The first block lists the calculations of the physical forces that the boosters will experience. The second block lists the calculations required to determine the magnetic field necessary to keep the boosters attached. Finally, the third block lists calculations required to determine circuit properties to produce the current required for a magnetic field that will cancel that effect of the field produced by the permanent magnet.

Table 3.6. Flowchart containing equations for current calculations.

Equation	Given/Assumed	Previously Calculated	Unknowns	Reference	Equation # in Reference
Block 1					
$F_{rf} = \omega^2 r m$	ω, r, m	~	F_{rf}	[58]	4-21
$F_{ad} = \frac{1}{2}\rho v^2 C_d A$	ρ, v, C_d, A	~	F_{ad}	[21]	4-22
$F_{tot} = F_{rf} + F_{ad}$	~	F_{rf}, F_{ad}	F_{tot}	~	~
Block 2					
$F_m = 4000 C B_r L_m \sqrt{\pi R_m^2}$	C, B_r, L_m, R_m	~	F_m	[21]	4-24
$B_m = \frac{B_r}{2}\left(\frac{L_m}{\sqrt{R_m^2 + L_m^2}}\right)$	B_r, L_m, R_m	~	B_m	[21]	4-25
Block 3					
$N = N/L \cdot L_c$	$L_c, N/L$	~	N	~	~
$L = \frac{\mu_0 \mu_r N^2 \pi R_c^2}{L_c}$	$R_c, L_c, \mu_0, \mu_r,$	$N,$	L		
$R_{overdamped} = 2\sqrt{\frac{L}{C}}$	C	L	$R_{overdamped}$		
$p_1, p_2 = \pm\frac{R}{2L} + \sqrt{\left(\frac{R}{2L}\right)^2 - \frac{1}{CL}}$	C, R	L	p_1, p_2	[21]	4-17
$i = \frac{V}{L}\left(\frac{1}{p_1 - p_2}\right)e^{p_1 t} + \left(\frac{1}{p_2 - p_1}\right)e^{p_2 t}$	V	L, p_1, p_2	i	[21]	4-19

The first block focuses on the physical forces the boosters will experience. The specific force that we are looking at is the radial force because we want to prevent the booster from separating prematurely. These forces include the drag and centrifugal force. For a worst-case scenario, we assumed that the rocket would be rotating at 600 rotations/min. This number was assumed by the WARRIORS I team to calculate the maximum potential rotational force [21].

$$F = \omega^2 r m \qquad (3\text{-}16)$$

Table 3.7. Nomenclature and units for electromagnet model.

Name	Variable	Units	Name	Variable	Units
Rad/hertz/spin	ω	1/s	Radius of Magnet	R_m	m
Radius from CG to boosters	r	m	Magnetic Flux of magnet	B_m	T
Mass	m	kg	Length of steel core	L_c	m
Rotational Force	F_{rf}	N	Ratio of wire turns per core length	N/L	$\sim$
Air Density	ρ	$\dfrac{kg}{m^3}$	Number of total wire turns	N	$\sim$
Velocity	v	$\dfrac{m}{s}$	Magnetic constant	μ_0	H/m
Drag Coefficient	C_d	$\sim$	Relative permeability	μ_r	$\sim$
Frontal Area	A	m^2	Inductance	L	H
Asymmetric Drag Force	F_{ad}	N	Voltage	V	volts
Total Force	F_{tot}	N	Resistance	R	Ω
Indicated Force Coefficient	C	$\sim$	Zeros of Denominator	p_1, p_2	$\sim$
Estimated Residual Magnetism	B_r	T	Current	i	A
Length of Magnet	L_m	m			

In Eq. (3-16), ω is the angular speed in revolutions per second, r is the radius from the center of the rocket to the separation system, and m is the mass of the booster. Additionally, we added the force of asymmetric drag. This force, as seen in Figure 3.9, is the force component that could potentially push the model rocket radially away from the main core prematurely. Including this force grants a more conservative answer which leaves a safety margin for our calculations. This assumption was made to help lower the scope of the project for there to have results in the given time frame. The location of the booster can be seen in Figure 3.9.

For the total axial force, we utilized Eq. (3-17):

$$F = \frac{1}{2}\rho v^2 C_d A \qquad (3\text{-}17)$$

In this equation the ρ represents the density of air, v the velocity, A the frontal area of the booster cross sectional area, and C_d the estimated drag coefficient. For our initial calculations, the values from Eq. (3-17), for the centrifugal force, were assumed from the previous project, WARRIORS I [21]. To find the radial force value, extensive beyond the scope of our project would have been required. We used an estimation for the radial force where that value is roughly ten percent of the axial force. Later in the project, we assumed from a max velocity value calculated by the FDC MQP Team provided in MAD-1901 [2]. Table 3.8 describes each variable and its origin and the assumed parameters and their rationale that were made to help create the flowchart.
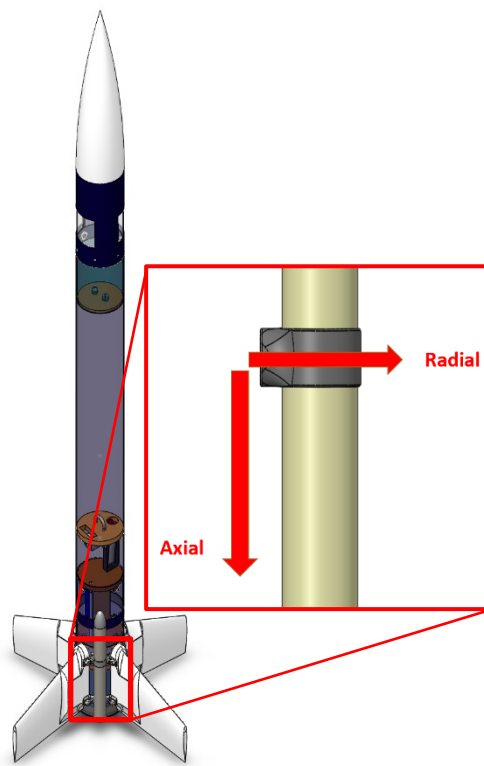
Figure 3.9. Diagram showing direction of radial and axial drag forces.

After adding these forces together, we calculated the total force to be 27 N. This force was calculated to be the maximum force that the booster will experience in the radial direction. We focused on the radial force due to its direct correlation with a successful launch. During acceleration there will be an axial component which will cause friction in the mount, however it

has not been considered for the purpose of these calculations. Knowing this radial force, the next step was to calculate a magnetic field sufficient to withstand this force.

Table 3.8. Assumed parameters and rationale.

Assumed parameter	Rationale
Residual Magnetism, B_r	Average for Neodymium Boron Magnet ~ 1.2 Teslas
Magnetic Permeability, μ_r	The magnetic permeability for a solenoid with a full steel core is 100. In our case, since the core was only half filled with steel, we roughly assumed a magnetic permeability of 50.

In the second block of calculations, we calculated the properties of the magnetic field and consequently, the dimensions of the electromagnet. Now that the total force the booster will experience has been estimated, we calculated the dimensions of a permanent magnet capable of withstanding that force. In these calculations we decided to use the dimensions that the WARRIORS team had as a foundation to our design. The updated dimensions can be found in Figure 3.10.
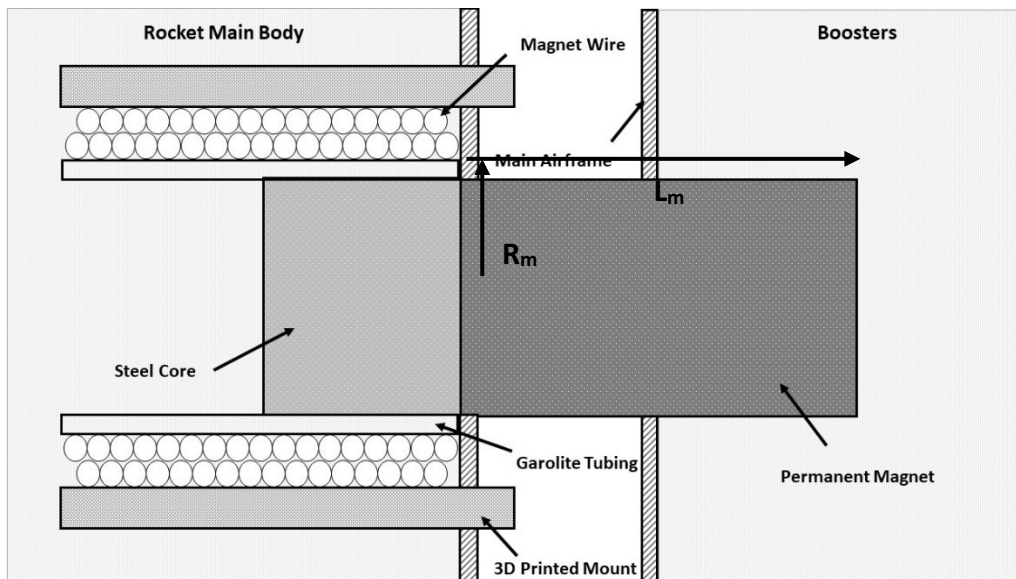
Figure 3.10. Electromagnet diagram.

Some changes were made to this design due to our design choices and integration with the MSAT team. The MSAT MQP Team designed brackets for the booster structural integration which has been provided in NAG-1901 [1]. During the integration efforts, the MSAT Team required more room for the permanent magnet to attach to the booster. We decided to extend the steel core and the permanent magnet slightly outward to compensate for this design. Figure 3.10 and 3.11 displays the updated model for the electromagnet separation system. Appendix I shows more photos of the CAD models in different views.
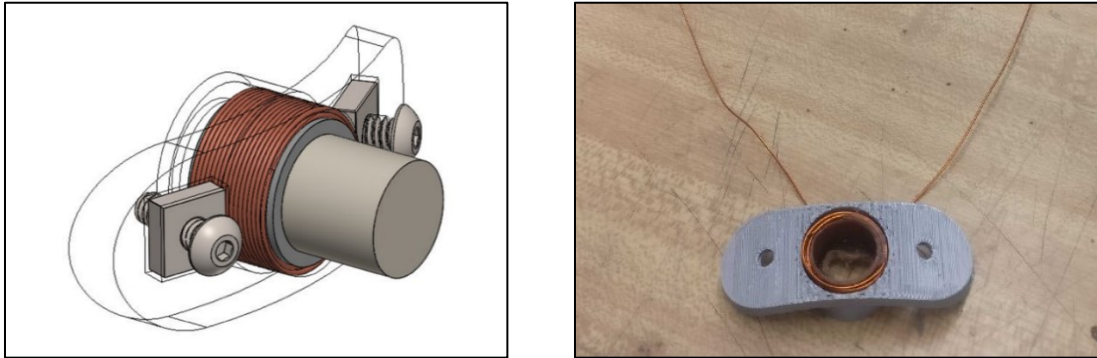
Figure 3.11. CAD Model of electromagnet (left). Prototype of electromagnet coil mount (right).

Figure 3.12. Solenoid with two layers. of wires.

A main concern we had for this design was the relatively small force required to separate the steel core from the permanent magnet. Upon consulting with the MSAT MQP Team, they assured us that most of the axial forces would be counteracted by the hook at the bottom of the rocket shown in Figure 3.9. Changing the placement of the steel core may change aspects of the magnetic field however our current calculations do not account for this. Further information about this concern required intensive

research regarding the magnetic field and relative permeability of the core. Equation (3-18) was used to calculate the magnetic field strength.

$$B_m = \frac{B_r}{2} \frac{L_m}{\sqrt{R_m^2 + L_m^2}}$$

(3-18)

In this equation, B_r represents the residual magnetic field, L_m the length of the magnet, and R_m the radius of the magnet as shown in Figure 3.10. These calculations resulted in a magnetic field of 0.54 T. As a safety factor, we increased the magnetic field to be 0.6 T. Following the determination of the properties of the magnet, we calculated the coil parameters as seen in Table 3.9.

Table 3.9. Coil parameters.

Inner Diameter	0.5	Inches
Number of Layers	2.0	-
Number of Turns per Layers	16.5	-
Wire Gauge	24	-
Total Extra Series Resistance	1	Ohms
Applied Voltage	48	Volts
Applied Capacitance	4.0	Farads
Relative Permeability of Core	100	-
Outer Coil Diameter	0.69	Inches
Total Resistance	1.5	Ohms
Peak Current Flow	24	Amps
Coil Inductance	2.0	Milli-Henry's
Time Constant Ratio	1.33	seconds

We researched methods to calculate inductance, looking specifically for equations that include the effect of a steel core. The most basic equations for finding inductance are given in Eq. (3-19) and (3-20).

$$L = \frac{\mu N^2 A}{l}$$

(3-19)

$$\mu = \mu_0 \mu_r \tag{3-20}$$

The magnetic field created by the electromagnet is directly proportional to the current in the wire. We first calculated the required current to better understand how powerful the electromagnet needed to be. To find this current, Eq. (3-21) was rearranged from a WARRIORS I equation [21]:

$$i_{min} = \frac{2B_m\sqrt{R_c^2+L_c^2}}{\mu_0\mu_r N} \tag{3-21}$$

In Eq. (3-21), B_m represents the magnetic field created by the permanent magnet. R_c is the radius of the coil, L_c the length of the coil, μ_0 the permeability constant, μ_r the relative permeability, and N the amount of turns of the wire. Due to the various equations and the overlapping situations to which these equations apply, we chose to merely use the permeability of free space constant multiplied by the relative permeability. From these calculations, we found that the minimum required current was 4.3 A.

3.3 Results and Analysis

We performed analyses on the two stage separation systems to produce designs that accomplished our project goals and team objectives. Our objectives were to create novel stage separation systems that were above-all-else reliable for multiple uses. We investigated the mass flow of CO_2 stage separation system to determine that our system would properly pressurize the payload compart of the rocket body and jettison the nosecone at apogee. Additionally, we tested the CO_2 separation system and conducted materials testing on rapidly manufactured parts. We tabulated necessary properties to analyze an electromagnetic booster separation system and determined the most efficient system arrangement.

3.3.1 Carbon Dioxide (CO₂) Separation Results and Analysis

CO₂ Flow Calculations

We calculated the amount of CO_2 necessary to properly pressurize the payload compartment of the rocket tube as detailed in Section 3.2.1 and using the initial conditions specified in Table 3.10. The MATLAB code for these calculations can be seen in Appendix G. The mass flow of the CO_2 varies with time, as well as the pressure, density, and temperature as explained in 3.2.1. We analyzed the mass flow out of the cartridge and into the payload section of the airframe with respect to time to estimate the time needed for the CO_2 cartridge to deplete and the final pressure at that time point, as seen in Figure 3.13 and 3.14. Then, we applied isentropic relations to the CO_2 in the cartridge and CO_2 – air mixture in the rocket tube to determine the density, temperature, and pressure inside each volume. In Figure 3.13, the plot represents the change in pressure in the CO_2 cartridge, while Figure 3.14 the change in pressure inside the payload compartment. In these plots, the two curves identified in the legend represent the pressure with a changing compressibility factor and with a compressibility factor of unity. It can be seen in Figure 3.13 that the compressibility factor does not greatly affect the results of mass flow and pressure. We solved an ordinary differential equation, Eq. (3-5), to estimate the time-lag between the command to initiate separation and when the nosecone is ejected.

For the CO_2 flow calculation, the first stage of flow corresponds to the choked flow of CO_2 out of the cartridge into the rocket body as seen in Figure 3.13 and 3.14. We calculated the properties of the 12 g of CO_2 inside the cartridge using the initial conditions in Table 3.10 and the equations given in Table 3.3. The CO_2 cartridge depletes from an initial pressure of approximately 6.4 MPa to higher than atmospheric pressure during stage one because it does not deplete completely. For the purpose of comparison, the changing mass flow rate and pressures are shown with a compressibility factor that is calculated at each timestep and of a constant value equal to unity (i.e. the ideal gas assumption) in Figures 3.13 and 3.14. The disparity between the two lines shows why the compressibility factor is necessary because the two results are not the same throughout the timespan.

We first determined the properties of the air initially in the rocket tube, as seen in Table 3.10, to find the final pressure in the rocket tube at the end of the choked flow regime, as well as the average fluid properties of the CO_2 – air mixture in the rocket tube during CO_2 depletion as

described in Section 3-2-1. At the conclusion of the first stage, the pressure is approximately 219,671 Pa (31.9 psi) after 0.063 seconds, as seen in Figure 3.14. Additionally, the second line in Figure 3.14 shows at what point the necessary pressure differential is reached for the nosecone to jettison from the model rocket.
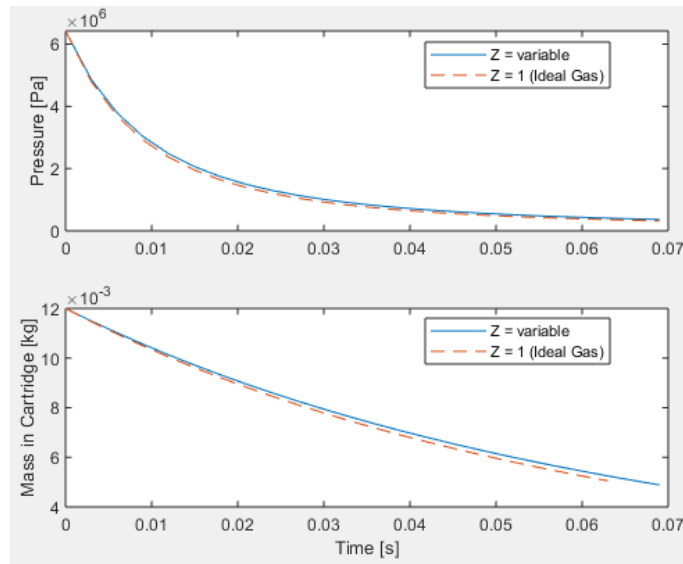
Figure 3.13. Change in mass and pressure over time in the CO_2 cartridge (first stage of flow) with a changing compressibility factor (Z) and as a perfect gas (Z =1).
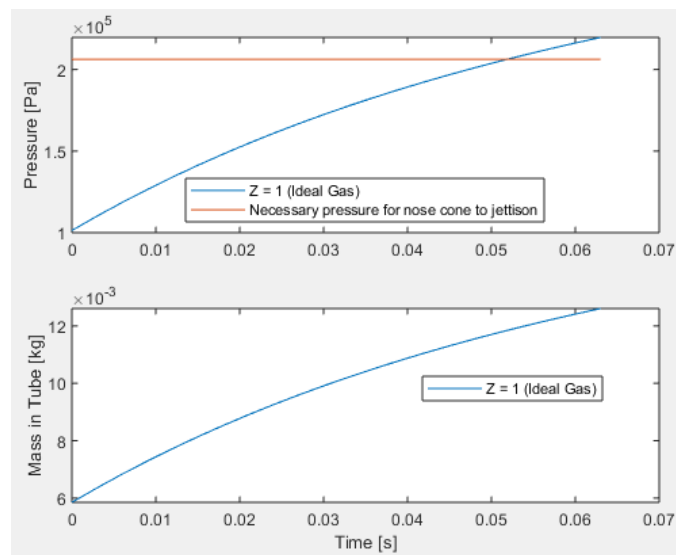
Figure 3.14. Change in mass and pressure over time in the payload compartment (first stage of flow).

Table 3.10. Initial values and physical constants for CO_2 transient flow calculations.

Variable	Description	Value at t=0s	Units
$P_{c,0}$	Pressure in cartridge	6.4	MPa
$T_{c,0}$	Temperature in cartridge	298	K
m_{CO_2}	Mass of CO_2 in cartridge	0.012	kg
V_c	Volume of cartridge	0.000014	m^3
M_{CO_2}	Molar mass of CO_2	44.01	$\frac{g}{mol}$
γ_{CO_2}	Ratio of specific heats of CO_2 at standard pressure and temperature	1.28	unitless
R_{CO_2}	Gas constant of CO_2 at standard pressure and temperature	188.9	$\frac{J}{kg\,K}$
$n_{CO_2,0}$	Initial amount of CO_2	0.2727	mol
C_{p,CO_2}	Specific heat, constant pressure	0.849	$\frac{kJ}{kg\,K}$
a	Van der Waal constant of CO_2	1888.6	$\frac{Pa\,m^6}{kg^2}$
b	Van der Waal constant of CO_2	0.0009748	$\frac{m^3}{kg}$
$\rho_{c,0}$	Density of gas in cartridge	857.14	$\frac{kg}{m^3}$
$m_{t,0} = m_{air}$	Mass of gas in rocket tube	0.2209	kg
M_{air}	Molar mass of air	28.96	$\frac{g}{mol}$
$\rho_{t,o} = \rho_{air}$	Density of gas in tube	1.225	$\frac{kg}{m^3}$
$P_{t,0} = P_{atm}$	Pressure of gas in tube	101,325	Pa
$T_{t,0}$	Temperature in tube	298	K
V_t	Volume of tube	0.00494	m^3
R_{air}	Gas constant of air	287.05	$\frac{J}{kg\,K}$
A_e	Exit area of cartridge	0.000001	m^2
$R_{mix} = R_{air}$	Gas constant of CO_2 – air mixture	287.05	$\frac{J}{kg\,K}$
$\gamma_{mix,0} = \gamma_{air}$	Ratio of specific heats of CO_2 – air mixture	1.403	unitless
n_{air}	Amount of air	7.6278	mol
$C_{p,air}$	Specific heat, constant pressure	1.005	$\frac{kJ}{kg\,K}$
R	Universal gas constant	8.314	$\frac{J}{mol\,K}$
g	Acceleration due to gravity	9.81	$\frac{m}{s^2}$
R_{bp}	Gas constant of combustion of FFFF Black Powder	66.26 [15]	$\frac{N\,m}{kg\,K}$
$T_{combustion}$	Temperature of combustion of FFFF Black Powder	1837.222 [15]	K
m_{nose}	Mass of nosecone	0.283495	kg
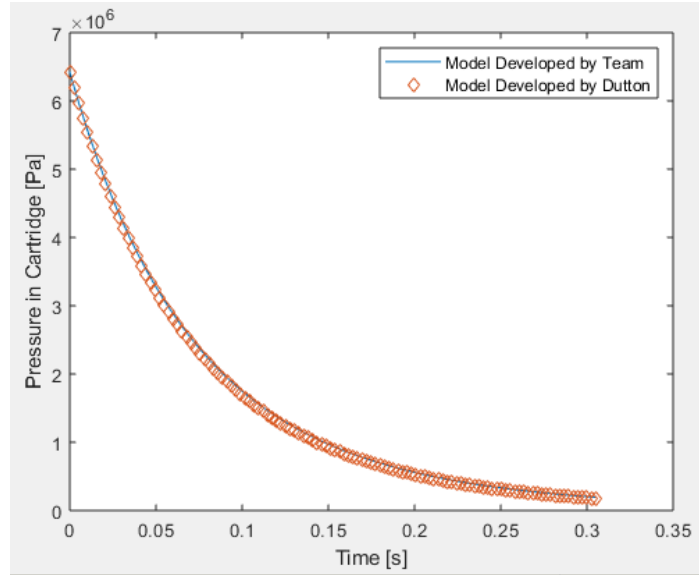
Figure 3.15. Change in pressure over time in the CO₂ cartridge (top) and rocket tube (bottom) using the team's model and Dutton's model (first stage of flow).

We also implemented an alternative method to model the CO_2 flow out of the cartridge and to verify our model. Using a dimensionless method proposed by Dutton [45] to model the properties of discharging vessels, we compared the differential equation model developed by the team to results produced using Dutton's method for the simplest case of flow. Dutton's method allows the properties of flow to be calculated analytically because the gas is assumed to be perfect and therefore the transient properties can be reduced to only depend on time and the specific heat ratio of the gas in a dimensionless case. In this case, 12 g of CO_2 flows into a rocket tube that is assumed to be evacuated prior to the process, with all other initial conditions remaining the same. Dutton specifies that the model assumes the gas to be of a uniform state, the average velocity in the tank to be equal to zero, the cartridge opening to be an ideal converging nozzle with isentropic flow, and the flow to be one-dimensional. In this model, gravitational potential energy and shear and shaft work are neglected. Additionally, the gas is assumed to be thermally and calorically perfect and the thermodynamic process is adiabatic. In the case of a discharging pressure vessel the dimensionless pressure, P_{disch}^+, can be calculated as seen in Eq. (3-22). The dimensionless pressure in the cartridge is related to the pressure by the relation $P_c = P^+ P_{c0}$. The dimensionless

time period, t^+, is arbitrary and is related to the timespan by the relation $t = t^+ \left(\frac{V_c}{A_e a_i} \right)$, where a_i is the initial speed of sound in the cartridge calculated using the initial properties of the CO_2. The calculated results for the case of a discharging pressure vessel in Figure 3.15 are similar to the results produced using the model we developed.

$$P^+_{disch} = \left[1 + \left(\frac{\gamma_{CO_2} - 1}{2} \right) \left(\frac{\gamma_{CO_2} + 1}{2} \right)^{\frac{-(\gamma_{CO_2} + 1)}{2(\gamma_{CO_2} - 1)}} t^+ \right]^{\frac{-2\gamma_{CO_2}}{\gamma_{CO_2} - 1}} \tag{3-22}$$

Twelve grams of CO_2 is sufficient to properly pressurize the nosecone based on the assumption that the necessary pressure difference between the rocket tube and the outside air must be between 68947.6 to 103421 Pa (10 to 15 psi). The final pressure at the end of the first stage of flow is 219,671 Pa (31.9 psi), which is greater than the necessary pressure to jettison the nosecone 206,288 Pa. When we subtracted the pressure necessary to overcome friction on the nosecone, the pressure differential is 116,804 Pa (16.9 psi) which is enough to jettison the nosecone. It is necessary to perform ground tests using various sizes of CO_2 cartridges to verify these results to account for assumptions made during the analysis.

Carbon Dioxide (CO_2) System Testing

We conducted several tests of different aspects of the CO_2 separation assembly. The first test was a functionality test of the magazine assembly where we loaded a CO_2 cartridge into the magazine and pressed the release button. During this process, we recorded the time it took for all the CO_2 to be released which took approximately 0.5 s. One of the biggest problems that we noticed in the initial CO_2 testing was the tendency of the magazine to leak. This was because of two factors: we were inexperienced in properly loading the CO_2 cartridges into the magazine and the components of the magazine had slight gaps in them. To combat these issues, we purchased liquid gasket maker and used it to seal the gaps in the gas system.
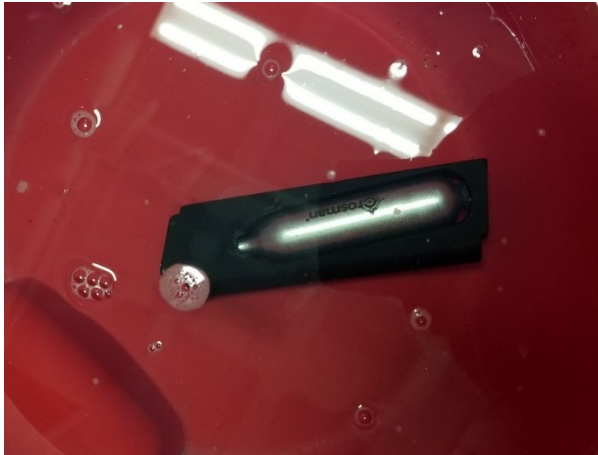
Figure 3.16. CO₂ short-term leak test.

Figure 3.17. CO₂ System test.

We completed leak testing after the liquid gasket maker had time to properly set. First, we conducted an audible test. This was completed by depleting a magazine with a fully loaded CO_2 cartridge and listening for leaks. We did not hear any leaks after applying the liquid gasket maker. We conducted two more leak tests: a short-term test and a long-term test. The short-term test consisted of loading a magazine and then submerging it in a bucket filled with water and dish soap as seen in Figure 3.16. The magazine was then let to sit for ten to fifteen minutes. During this time, we monitored the magazine to see if any bubbles formed which would indicate a leak in the system. This test proved to be a success as no bubbles had formed and no CO_2 appeared to have leaked out of the system. The next test we conducted was the long-term test, which consisted of loading a magazine with CO_2 and allowing it to sit for two hours. We measured the initial mass of the magazine and loaded cartridge and remeasured the assembly again after the two-hour period. This test also proved to be a success as the initial mass of the magazine was the same as the mass of the magazine taken after two hours within the measurement error. After these tests were successful, the entire assembly was constructed.

Before the overall separation system could be mounted on the inside of the rocket, we needed to test the system to prove the functionality of the firing mechanism. We conducted a test to confirm that the firing mechanism would function on its own, as seen in Figure 3.17, without the inclusion of the magazine. We assembled the CO_2 assembly system and connected the motor

to a 12 V power supply. Upon activation of the power supply, the motor shaft began to rotate and the nut that was on the threaded rod began to translate inside the housing as intended. Once the firing mechanism was proven to function on its own, a new CO_2 cartridge was loaded into the magazine. We clamped the magazine to the laboratory bench for testing to prevent movement, and a clamp was placed behind the motor so that its imparted force would not push it backwards and out of the assembly. We then clamped down the firing mechanism assembly next to the magazine, such that the rotation of the motor inside of the housing causes the nut to translate, which in turn causes the actuator to press and hold the release button on the magazine.

We then activated the power supply to initiate the movement of the motor. The motor shaft rotated, and the nut translated properly as with the first test. However, when the actuator contacted the release button, the motor stalled out. This test was conducted three times in a row to rule out any external factors in the test causing the motor to stall out. We then emptied the CO_2 from the magazine and the test was run again with an empty magazine. This time the actuator was successful with pressing and holding the release button before the motor stalled out. We revisited our previous calculations and determined that based on known properties of the threaded rod and estimated friction values, the motor should produce enough torque. We expect that this means the friction force due to the custom-designed parts is higher than we expected. The release button on the magazine requires different amounts of force to press it when the magazine is loaded with CO_2 as compared to when it is empty; when the magazine is loaded with CO_2, 12-15 lbs is required to actuate it. The success of the mechanism leads us to believe that the amount of torque is not high enough to generate 12-15 lbs of force. Additionally, the amount of torque necessary to produce 12-15 lbs of force is closer to the stall torque of the 460-rpm motor, not the optimal torque for use.

We also found that the custom-machined coupler that connected the motor shaft to the turned down threaded rod was oscillating slightly due to the length of the set screws. The set screws were contacting the housing during each revolution, which caused the actuation to occur at a slight angle. This angle means that only some of the total force was delivered to the button although we are not certain if the oscillation was enough to significantly affect the force on the button.

Launch Analysis

The first attempted launch for the rocket occurred on January 19th, 2019. The CO_2 separation system was not functional by this date. As a result, we used a black powder separation

system rather than the CO_2 system. Black ejection charges are common for stage separation in model rocketry. We calculated that approximately 2.3 g of black power would be needed to successfully separate the nosecone from the rocket body. During the preparations leading up to the launch, we conducted a static ground test of the black powder ejection charge system. A black powder charge was measured and loaded into the rocket and an electric match was put into the charge. The charge was then remotely detonated by the range safety officers, and separation was visually confirmed. During the ground test, the nosecone separated farther from the rocket body than was necessary for successful mid-flight separation. This occurred because the amount of black powder charge needed was calculated using a necessary internal pressure of 15 psi, the high end of the 10-15 psi range recommended by the model rocketry group NASSA [41]. Additionally, the scale we brought to the launch site malfunctioned while we there, and therefore the black powder amount may have been overestimated.

Material Testing

After we 3D printed the polylactide (PLA) test specimens, we hoped to conduct tensile testing on the specimens. Unfortunately, due to unavailability of machines, the tensile testing of these specimens was not completed. During an attempt to conduct the testing, we found that the yield strength of the PLA specimens was very close to the 2000 N load cell of the Instron tensile tester we were using. The testing was halted because applying a force greater than the load cell limit can result in the damage to the machine. We attempted to use a different tensile tester with a 3000 N load cell, however the larger Instron was not functional during our project.

3.3.2 Electromagnetic Separation Results and Analysis

We created a MATLAB$^{®}$ code to graph the current as a function of time using our updated resistance, capacitance, and other circuit properties as described in Section 3.2.2. For these calculations, we included capacitors of different values to gain an understanding of the effect of different capacitances on the system. The time-dependent current in the "RLC" circuit is described by Eq. (3-7) and (3-8) in Section 3.1.2, reprinted here for clarity.

$$p_{1,2} = -\frac{R}{2L} \pm \sqrt{\left(\frac{R}{2L}\right)^2 - \frac{1}{CL}} \tag{3-7}$$

$$i(t) = -\frac{U_1}{L}\left(\frac{1}{p_1-p_2}e^{p_1 t} + \frac{1}{p_2-p_1}e^{p_2 t}\right) \tag{3-8}$$

In Eq. (3-7), R represents the total resistance, L the inductance, C the capacitance, $p_{1,2}$ the zeros of denominator, and U the voltage.
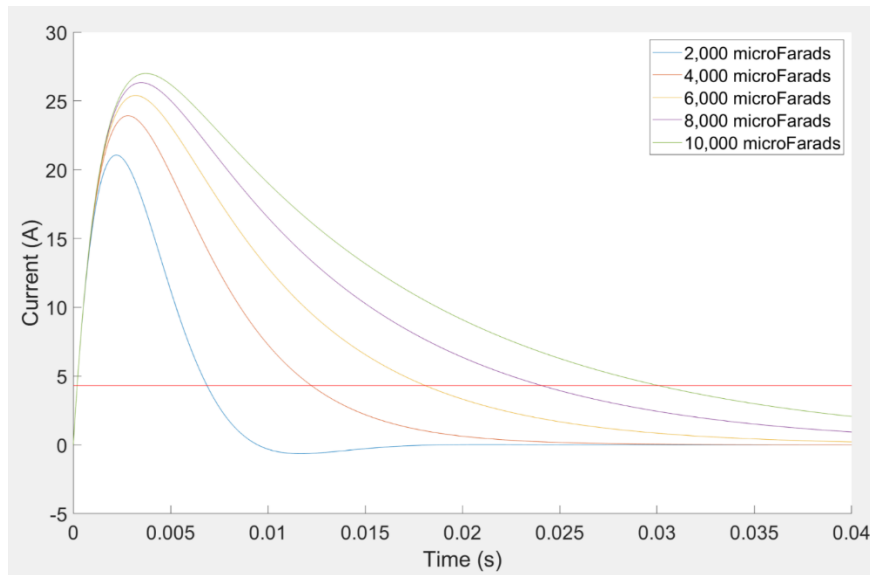
Figure 3.18. Current vs time with varying capacitance. Curves represent solutions with R=1.5 Ω , V=48 V and L=2 millihenries.

The maximum current over the range of capacitance assumed exceeded the minimum current necessary for separation. In Section 3.2.2, this was shown to be approximately 5 A. Based on these results, most of the capacitors would store sufficient energy for the system. However, time is a variable that we must take into consideration. If the magnetic field is not present for a sufficient time, the booster may not eject. As such, the time constant was calculated to estimate

the amount of time over which the booster could eject. To reach convergence, the amps is 5 multiplied by the time constant [59]. The time constant for the circuit described in Figure 3.18 was calculated to be 1.4 milliseconds, giving a maximum time to reach steady state of 7 milliseconds. The time constant duration must allow enough time for successful separation which would most reliably be measured in testing.

Additionally, since the circuit is an oscillatory system, the damping ratio is an important characteristic of the system. An oscillatory system can be either underdamped, critically damped, or overdamped [58]. It would be beneficial for the electromagnetic stage separation system to have a critically damped system. If the system were to be overdamped, the current may not be strong enough in a short amount of time to create a sufficiently strong magnetic field for successful stage separation. On the other hand, if the system were to be underdamped, an oscillatory behavior would appear which might reverse the magnetic field. This reversal could potentially "pull back" the magnet during separation and would lead to a separation failure.

We used these results to design a prototype system with capacitors of varying strength. The resulting system contained smaller capacitors, which results in a lower mass than that in the WARRIORS I and II designs. Not only was mass reduction a priority, but also assuring that the calculations were accurate so that they can be used for different situations. To measure these calculations, we utilized the circuit structure as shown in Figure 3.19.
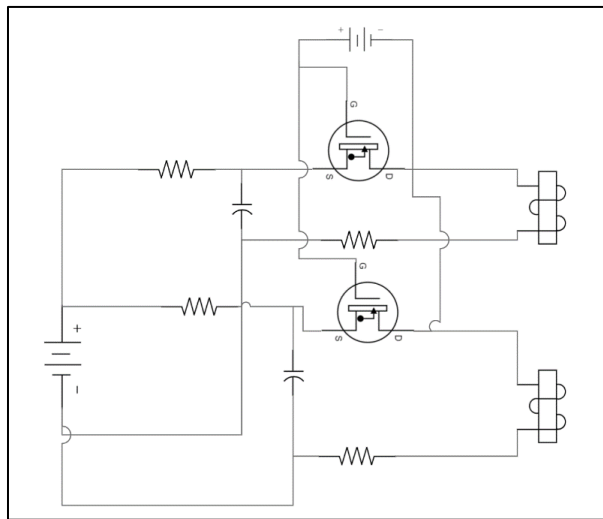
Figure 3.19. Circuit for electromagnet separation.

102

The entire electric circuit is shown for the two electromagnets. A new change in this circuit is the replacement of the switch. Our project utilized a MOFSET, or a metal-oxide semiconductor field-effect transistor. Our research showed that a MOFSET is a voltage driven switch capable of withstanding high currents.

The first step was to measure the force of the permanent magnet. To do so, we acquired a force gauge from the physics department with the help of faculty. Issues occurred with the integration with the steel core and the force gauge due to being unable to use the hook on a cylinder. To fix this, the setup was as followed. The force gauge was secured vertically with the hook facing downwards. A small hole had to be drilled in the steel core to wrap a string through. This string was then connected to the hook of the force gauge. We were only able to drill a hole in the 0.5 in length cylinder and not the 0.2 in length due to size constraints. Figure 3.20 is an example of the force exhibited by the permanent magnet on the steel core. Over five tests, we received an average of 20.3 N. These tests were extremely consistent and are used as a worst-case scenario considering that the steel core that was used for the test is smaller.
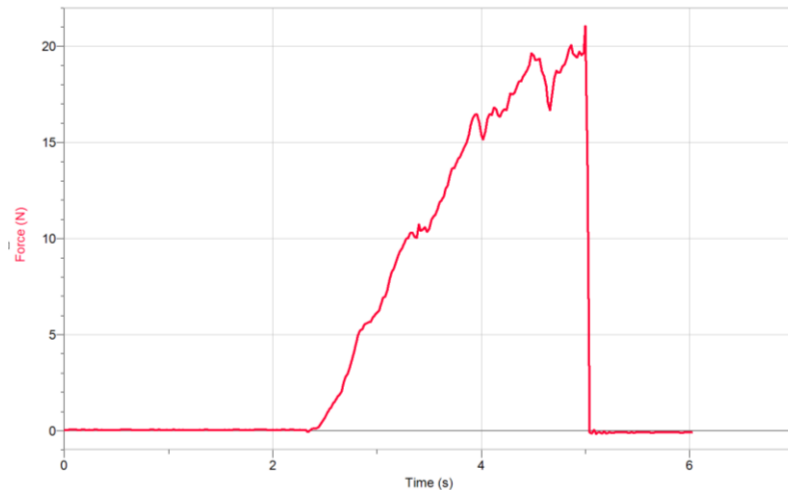
Figure 3.20. Forces vs time for a permanent magnet force test.

The simple design of the WARRIORS I circuit [21] was utilized as a foundation. While the main components of the circuit remained, some changes were done for better optimization. In

the WARRIORS I circuit, they used a TRIAC as a switch [21]. This switch would turn open the circuit so that the capacitor would discharge through the electromagnet. Instead of using a TRIAC transistor, we instead chose on a MOFSET. A MOFSET is a three terminal fully controlled switch. The reason why the MOFSET was chosen was because it is a capacitively driven transistor and the FDC MQP Team had experience using this switch in their design as referenced in MAD-1901 [2]. Another change in the circuit was the resistance value. We lowered the resistance to increase the amount of current. Since this circuit processed high power, special care was taken to assure the safety of the circuit. The power rating of the resistors was considered, and we purchased higher rated resistors.

Observing the magnet ejection from the electromagnet indicated a success. After charging the capacitor, and upon activating the switch, the magnet ejected forcefully. Considering that a small amount of force is needed until the air drag separate the booster, the force to eject we calculated was accurate. Depending on the circuit parameters, with enough amounts of current the magnet ejects out of the tubing. however, to fully understand if our calculations were correct, we required measurements of the voltages and currents in the circuit. We utilized an oscilloscope to be able to measure these values.

We had difficulties obtaining a 48 V power supply as we originally intended. The DC power supply that we were using only reached to roughly 31 V. Because of this we had to alter our calculations slightly to compensate. We changed the MATLAB® code values in consideration of this change.

One of our main goals for testing was to compare our calculations with measured values. To accomplish this, we measured the voltage and current values of the circuit. We used the Tektronix TDS 2004B oscilloscope to measure these quantities and a DC power supply for the voltage. Due to the limitations of the power supply as mentioned above, we took note of the voltage being produced and replicated that value in equations (3.28) and (3.29). Figure 3.21 shows the data from the DC power source and the oscilloscope.

Figure 3.21 shows the data from an oscilloscope for one of our discharge tests. The orange data are the voltage and the purple data are the current. In this graph, once the switch is activated, the voltage drops and the current spikes and then slowly depletes. The peak current almost reaches to 3 A until it starts to decrease. This relationship was expected and validates the data that we

received. To test the calculations and the MATLAB® code, the data from the tests was extrapolated and compared to. Figure 3.22 shows this graph.
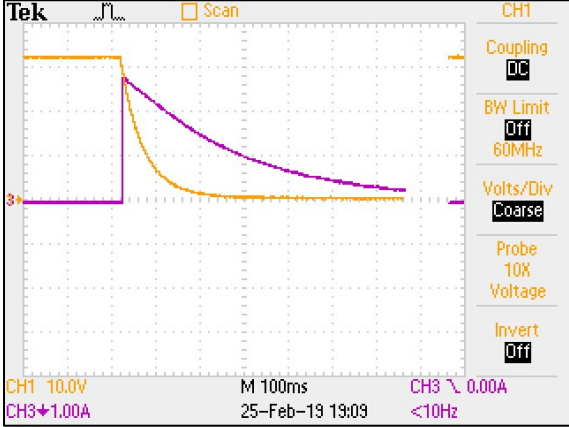
Figure 3.21. Oscilloscope data displaying voltage and current graph for circuit with properties R=10 Ω, V=31 V, L=2 milliHenries, and 4,700 microFarads.
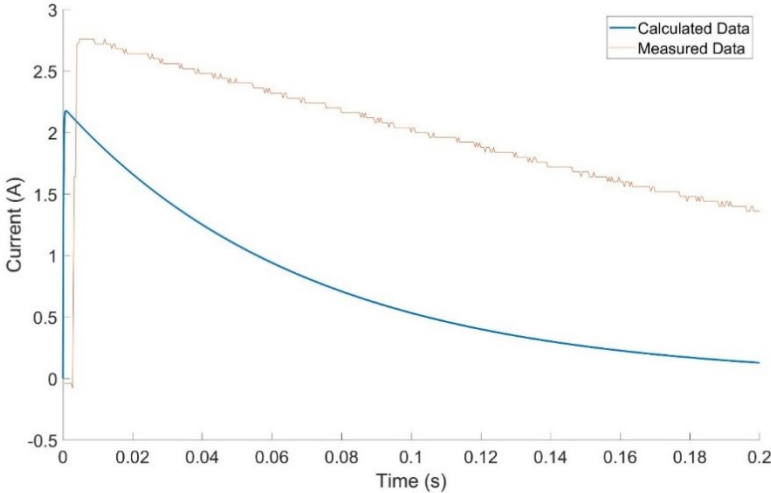
Figure 3.22. Comparison of MATLAB® data calculations and measured values for circuit R=10 Ω, V=31 V, L=2 milliHenries, and 4,700 microFarads.

Comparing Figure 3.21 and Figure 3.22 above, the current history shows a similar trend. The MATLAB® code results plotted in Figure 3.22 were used to determine the current from an RLC circuit with given parameters for resistance and voltage. These data points are plotted over a range of capacitance to visualize the difference in current after changing the capacitance. The resistance and voltage inputted to that code are identical so that a comparison can be made. The main differences between these data points are the peak value and the rate at which the current depletes. These data points show that the calculations can produce a realistic value for the current in this type of circuit, however further modifications must be made to account for realistic conditions. There are many different possibilities for the difference in decay time.

Potential differences between the calculation model and the actual measurements are listed. The calculation does not consider the resistance in a wire. While in calculations they can be considered negligible, they may skew the results slightly. Additionally, there are varying tolerance factors in all the equipment we used. This further alters the results. Finally, the electromagnets were homemade which introduces human error in the fabrication of the system. Specifically, the spacing between each wire would be inconsistent. Besides these factors, by adjusting the calculations in the equations and optimizing the circuit, our goals for this project were met. Comparing the calculated data with the measured data, they match and therefore validates our testing and provides a level of certainty that the calculations are accurate.

Chapter 4: Recovery

With the advent of reusable rocket technology by SpaceX, others have begun chasing the idea of a recoverable rocket. The development of a high-power rocket brings the opportunity to attempt innovations of this kind on a smaller scale. Due to advances in micro-circuitry, the computing power necessary to calculate the angle that rocket motor thrust should be when performing a powered landing is small enough to put on a model rocket. Companies such as Barnard Propulsion Systems, LLC [60] have specially developed computer processors that can perform these maneuvers through quicker calculations and more sensitive sensors. Unfortunately, the limitations of a hobby rocket launch and the safety concerns raised when attempting a completely powered-descent, such as limited budget and the dangers of launching in a field that could catch fire if the motors burned too close to the ground, makes the method impractical for amateur model rocketry.

Innovative recovery options that currently exist in model rocketry include glider recovery, spin recovery, drag device deployment, and helicopter [5]. The glider recovery method would effectively transition the rocket body into a fuselage for a flying wing or traditional glider [5]. This design concept was employed on the Space Shuttle. Spin stabilized utilizes the fins to create drag and stabilize the rocket upon return [5]. This method of recovery is difficult to execute on a large-scale rocket because of the required size of the fins and the stronger effect any disturbances would have on a larger body. The method would risk destruction of the rocket. A drag deployment device deploys a rigid surface which applies a drag force to the rocket body. This system would require large internal storage space and a risky deployment.

4.1. Autorotation

Helicopter recovery, more accurately autorotation recovery, is a rare form of recovery in model rocketry and in industry. The ROTON was a Vertical Takeoff, Vertical Landing (VTVL) concept designed in the 1990s [61] as a solution to the problem of returning a rocket safely to the ground. The ROTON used rocket engines placed at the ends of rotor blades to produce lift and stabilize the vehicle. Unfortunately, the concept of the ROTON was never fully realized and the company shut down in 2001. Hobby rocketeers have tried to use the concept of autorotation to successfully recover their systems. Auto rotation kits for model rockets are available from Apogee

Components such as the Gyro Chaser, as seen in Figure 4.1, and mini-copter, eRockets' Semroc kits, and Estes' Flip Flyer [62].

Figure 4.1. Gyro Chaser [62]. Copyright © 2018 Apogee Components.

Examples of the use of autorotation make it a viable option for the recovery system of a larger scale model rocket. The Kopter designs [63] found in a rocket design catalog dating from 1980, show a 20 in long rocket with internal deployable blades. These blades were oriented inside the rocket and opened using rubber bands. We used the setup of the blades inside the Kopter designs to understand the layout required to place the autorotation fins inside the model rocket body.

Project Hummingbird was a project conducted in 2017 by students at Embry-Riddle Aeronautical University [64]. The project tested the recovery of a rocket using autorotation. Project Hummingbird used an internally stored rotor-hub and a set of externally folded blades as the autorotation system. The autorotation system was built to be used inside a small sounding rocket

which reached an altitude of about 2,700 meters (8858 ft). At apogee, the rocket deployed a drogue parachute to vertically orientate the rocket, after which the blades opened, and rotation began. The students found it difficult to calculate how the autorotation system would perform, therefore they performed scaled tests to determine rotation characteristics.

The state of autorotation occurs when a rotor system continues to rotate and produce lift due to aerodynamic flow of air over blades, most commonly in relation to a helicopter [65]. Just as an airplane can continue to glide without power, a helicopter can continue auto-rotating to safety. Because a helicopter is generally moving forward when it begins to autorotate, parts of the blade are accelerating and applying torque to the central hub while others are pushing through the air creating lift the same way as a wing does. This is different from the rocket autorotation system because when the blades are deployed, the rocket is traveling directly downward and needs to start with no rotational velocity. The power required to produce lift comes from the relative wind traveling upwards from underneath the blades with a velocity U. The basic equation to calculate lift Eq. (4-1) is based on the velocity U, the density of the fluid around it ρ, which is calculated using the ideal gas law Eq. (2-3) for air based on the local temperature and pressure, the area of a chosen wing A, and the airfoil shape's coefficient of lift or C_L. Based on the literature, reasonable coefficients of lift typically range anywhere from 0.4 to 1.8 [66].

$$L = C_L \frac{1}{2} U^2 A \, \rho \qquad\qquad (4\text{-}1)$$

This means that the blades should have a negative angle, so that the upward rushing wind can accelerate the blades. As the blades begin to rotate, different parts of the blade are traveling at different velocities relative to the wind. This changes the lift created by different parts of the blade along the span of the blade because velocity U from Eq. (4-1). With the drag vector also in the direction opposite to the acceleration of the falling rocket, it will also aid in the stable descent of the rocket. These characteristics along the span of a blade are illustrated in Figure 4.2. The left side of this figure illustrates the different regions and points of equilibrium on a blade in autorotation descent. The different regions include the driven region (A), driving region (C), and the stall region (E). The driven region and stall region are the sections on the blade where drag is

produced. While the driven region is where the autorotative force or lift is produced. The two points of equilibrium (B and D) are located between the driven region and driving region, and the driving region and the stall region. The four panels on the right side illustrate the free body diagrams of the airfoils at each region and point of equilibrium. Each panel shows the angle of attack, lift force, drag force, and total aerodynamic force vectors.
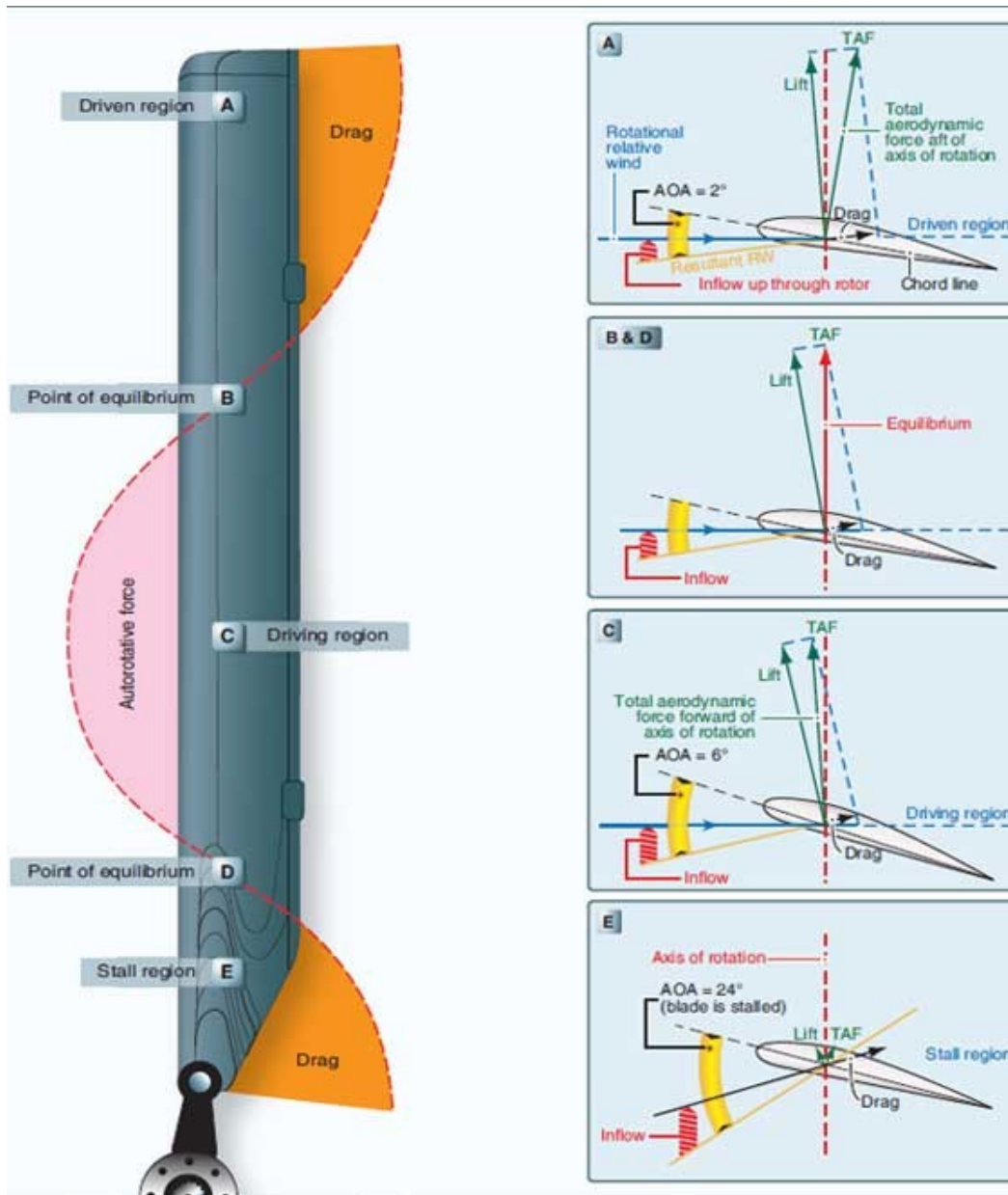
Figure 4.2. Force vectors in vertical autorotation descent [67]. Copyright © 2018 FlightLearnings.com.

In a twisted blade, we identify a "driving region," which produces the forces necessary to turn the blades. The goal in the design of an autorotation system is to have this driving region extend over about 40 percent of the blade radius in order to keep the blades rotating quickly enough to produce enough lift to maintain the desired decent rate. This desire to optimize the characteristics of separate parts of the blade leads to a design, characteristic of most rotating blades such as airplane propellers and wind turbines, in which the blades are twisted. Meaning that each region of the blade has a different angle of attack.

4.2 Methodology

This section presents our methodology to calculate the force provided by an autorotation recovery system to slow the rocket's descent. The MATLAB® code for the calculation using this design methodology is presented in Appendix J. We created the initial designs for the recovery system to meet our objective of developing novel and innovative recovery systems. We reviewed four different designs and ranked them based on levels of risk relative to an established baseline option. Compared with the baseline, these three options were identified as low, medium, and high risk. The baseline option was a conventional parachute-based recovery system, the low-risk option was spin-stabilization with parachute recovery, the medium-risk option was helicopter/autorotation descent, and the high-risk option was powered descent recovery. We chose autorotation descent as an innovative approach to recover a high-power model rocket in order to meet the project goals of and offer a feasible design challenge.

Autorotation has been used in small (< 1 kg) model rockets; however, it is rare to find a high-power model rocket with an autorotation recovery system. Therefore, successfully creating an autorotation system would accomplish the recovery team's objectives. We chose parachute recovery for our first test launch in January 2019, prior to the completion of the autorotation system. After choosing a parachute and autorotation system, we were able to state the objectives for the recovery system.

- Design and build a successful autorotation system to be deployed with a drogue parachute that will achieve the correct landing velocity and return the rocket to the ground safely

4.2.1. Autorotation Design

Autorotation is an uncommon recovery system for high-power model rockets; however, kits for low power model rockets are widely available. These kits come with pre-made blades attached to the rocket body. Designing and fabricating blades as well as a system to deploy the blades is an innovative and difficult design challenge. We pursued both designs as part of this project.

The autorotation option for high-powered rockets has been approached few times and therefore, despite an extensive literature search, we were not able to find documentation for solving this problem. The first approach we considered as a guide, was for the case of a helicopter which has lost power and must autorotate safely to landing. We found some basic characteristics required to calculate the properties needed to design the blades using *Flight Performance of Fixed and Rotary Wing Aircraft* by Antonio Filippone [68].

Table 4.1. Nomenclature and units for blade design.

Variable	Name	Units	Variable	Name	Units
W	Weight	N	λ	Tip Speed Ratio	~
ρ	Air Density	$\frac{kg}{m^3}$	$\frac{W}{A_D}$	Disc Loading Ratio	$\frac{kg}{m^3}$
c	Chord Length	m	ΩR	Root tip speed	$\frac{m}{s}$
N	Number of Blades	~	Ω	Equilibrium Rotational Speed of Blade	$\frac{rad}{s}$
R	Blade Span	m	α	Angle of Attack	Deg.
r	Distance along span	m	$\emptyset$	Local Inflow Angle	Deg.
A_D	Area of Disc	m^2	ψ	Angle of Twist	Deg.
b	Number of Blades	~	C_l	Lift Coefficient	~
m	Mass	kg	C_d	Drag Coefficient	~
V_w	Descent Velocity	$\frac{m}{s}$	V_{rel}	Wind velocity relative to the blades	$\frac{m}{s}$
a	Acceleration	$\frac{m}{s^2}$	F_{hr}	Horizontal Force	N
a_t	Angular Acceleration	$\frac{rad}{s^2}$	F_g	Gravity	$\frac{m}{s^2}$
L	Lift	N	T	Torque	Nm
L_r	Lift Along the Span of the Blade	N	I	Moment of Inertia	kgm^2
D_r	Drag Along the Span of the Blade	N	dt	Time Step	s
v	Velocity	$\frac{m}{s}$	dS	Differential Segments of the Blade Span	m
v_0	Initial Velocity	$\frac{m}{s}$	dF_{tot}	Differential Total Force	N
v_f	Final Velocity	$\frac{m}{s}$	F_{TOT}	Total Force	N

ω	Angular Velocity	$\frac{rad}{s}$	h_0	Initial Height	m
ω_0	Initial Angular Velocity	$\frac{rad}{s}$	D	Drag	N
h	Height	m	σ	Rotor Disk Solidity	~
μ	Ratio Along Span of Blade	~			

All the parameters used in the model described in this section are defined in Table 4.1. The primary characteristic used to calculate various properties of an autorotating blade is the root tip speed Eq. (4-2). The root tip speed, located at the tip on the blade in Figure 4.4, is the velocity at which the tip of the autorotating blade is in a state of equilibrium, which means that the blades are neither accelerating nor decelerating, but have constant angular velocity. In Eq. (4-2), R represents the span of the blade and Ω the rotational speed of the blade (in radians per second). The span of the blade, R, is determined by the geometry of the internal space of the rocket. We were limited by the internal space in the payload compartment of the rocket that was allotted to our team. The rotational rate of the blade is used to calculate the relative velocity of air along the span of the blade in later calculations. The velocity of air along the span of the blade is shown in Figure 4.4.

$$\Omega R = \sqrt{\frac{6W}{C_l \rho A_D \sigma}} \tag{4-2}$$

Equation (4-2) relates the root tip speed to the weight of the payload, W, the coefficient of lift, C_l, the density of ambient air, ρ, the area of the disk swept by the rotors, A_D, and the rotor disk solidity, σ. The rotor disk solidity is calculated in Fig 4.3 by multiplying the number of blades N with the chord length c, then dividing by the span R multiplied by π. The area of the disk, as given by Eq. (4-3), is the total area that the blades sweep out. The rotor disc solidity is calculated in various ways depending on the physical design of the deployment system, as seen in Figure 4.3. However, we used the formula shown as Solution 1 (in Fig. 4.3) for the rotor disk solidity because our design required a central hub around which to rotate.

$$A_D = \pi R^2 \tag{4-3}$$

SOLUTION 1   STANDARD   SOLUTION 2

$$\sigma = \frac{Nc}{\pi R(1+a)}$$

$$\sigma = \frac{Nc}{\pi R}$$

$$\sigma = \frac{Nc(1-a)}{\pi R}$$
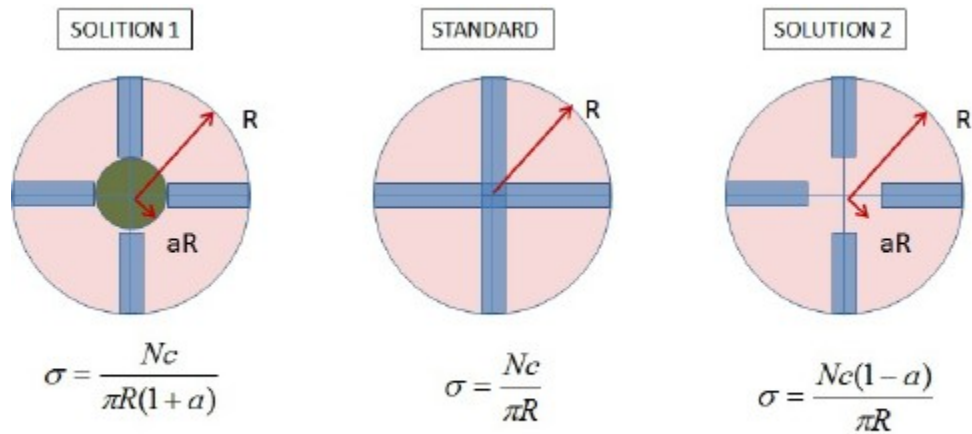
Figure 4.3. Diagram showing top view of rotor and three methods of calculating rotor blade solidity [69]. Copyright © 2015 Riccardi Possamai.

The equations shown in Figure 4.3, are used to calculate rotor solidity, where N is the number of rotors, c is the chord length, R is the span of the blade and a is an axial induction factor. From this point there was no clear way to determine the value of C_l using helicopter design techniques. Autorotation is usually a secondary characteristic approached by helicopter designers, which is generally under power, with adjustable pitch rotors, and consist of a single airfoil shape along the entire blade length. Thus, we needed to approach the challenge of designing the autorotation system differently.

A wind turbine is an aerodynamic blade but is not under power and is therefore optimized to produce maximum lift from the oncoming wind. The main difference is that a wind turbine is optimized to rotate at the maximum velocity possible in order to produce high torque, while the autorotation recovery system calls for more force to be generated perpendicular to the plane of the spinning blade [65]. This means that wind turbine is optimized to reduce drag produced from the blade. But we are attempting to slow the rocket down during descent. Therefore, the wind turbine design method outlined in a standard reference such as *The Wind Energy Handbook* by Burton et. al. [66], is not entirely applicable for our analysis; however, we referred to the blade geometry of wind turbines as a guide. Specifically focusing on the lift coefficients of wind turbines.

Data presented in *Wind Energy Handbook* and *Design of a Tapered and Twisted Blade for the NREL Combined Experiment Rotor* [70], shows that most lift coefficients of wind turbines at the tips of the blades are quite low and always less than one. Producing an initial C_l guess around 0.5 allows for a tip speed guess using Eq. (4-2). In order to be usable, the tip speed needs to be divided by the downward velocity, shown in Eq. (4-4). The wind velocity, v_w, is assumed to be the decent velocity in the case of an autorotation recovery system.

$$\lambda = \frac{\Omega R}{v_w} \tag{4-4}$$

After we determined an optimal tip speed and tip speed ratio based on the decent velocity, we calculated the coefficient of lift along the span of the blade. We calculated the coefficient of lift using the design for variable-speed equation developed in the *Wind Energy Handbook* to maximize the power produced by each element of the blade as seen in Eq. (4-5). In Eq. (4-5), μ represents a nondimensional coordinate along the span of the blade $\frac{r}{R}$, with the origin at the root or center. Each of these $\frac{r}{R}$ differentials represent a blade element that is being analyzed.

$$C_l = \frac{8}{9} \frac{1}{\frac{bc\lambda}{2\pi}\sqrt{(1-\frac{1}{3})^2 + \lambda^2\mu^2(1+\frac{2}{9(\lambda^2\mu^2)})^2}} \tag{4-5}$$

Because of the limit placed on the span of the blades from the geometry, we knew that we would need to optimize the blades by twisting them in order to change the angle of attack along the blade. If the blades are not twisted, the angle of relative wind close to the center (i.e. the root) of the blades would be too large to create lift and would be stalled. Another way to increase the performance of the blades is by designing for a different tip speed, calculated using Eq. (4-2). In the case of our project, we had limitations due to the internal space available to fit the blades. However, if it were possible to allot more internal space to the autorotation system, we could

increase the tip speed by increasing the span, R, and finding the balance between the number of blades and the chord length.

To understand the forces produced by the blades requires an understanding of how the relative wind varies along the span of the blade. Figures 4.4 and 4.5 show our reference system. Figure 4.5 represents the cross section at a coordinate r along the total span R.
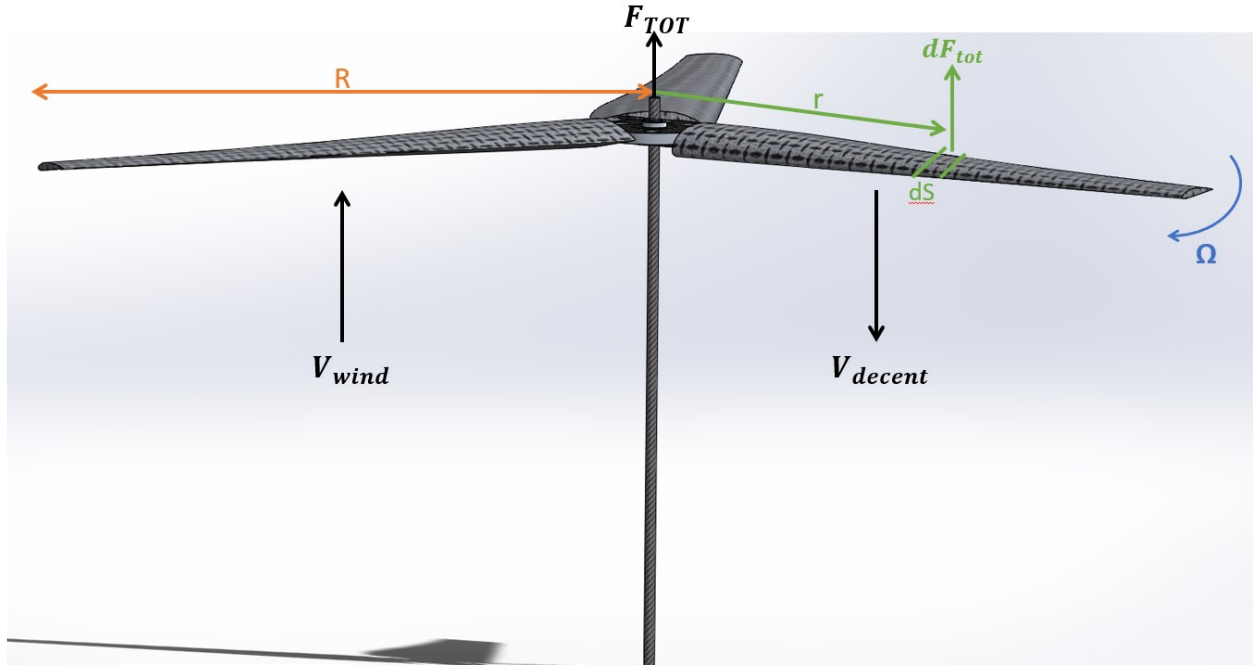
Figure 4.4. Autorotation system reference frame.

$$V_{rel}(r) = \sqrt{(\Omega r)^2 + v_w{}^2}$$

(4-6)

$$\varphi = arcsin(\frac{v_w}{\Omega r})$$

(4-7)

$$\alpha = \varphi - \psi$$

(4-8)

In Eq. (4-8), ψ represents the angle of twist, with "no-twist" corresponding to a location at which the chord is perpendicular to the downward velocity, which can be determined during

final blade design. Equations (4-6) and (4-7) are visualized in Figure 4.4. Where $V_{rel}(r)$ is the red vector in the direction of the relative wind velocity and φ, the local inflow angle, is the angle between the root tip speed and the relative wind velocity. After we determined the coefficients of lift along the blade, we calculated the coefficients of drag. Because we solved for a blade in an equilibrium state, we knew that the lift and drag force components along the axis of rotation are equal, show in Eq. (4-9).
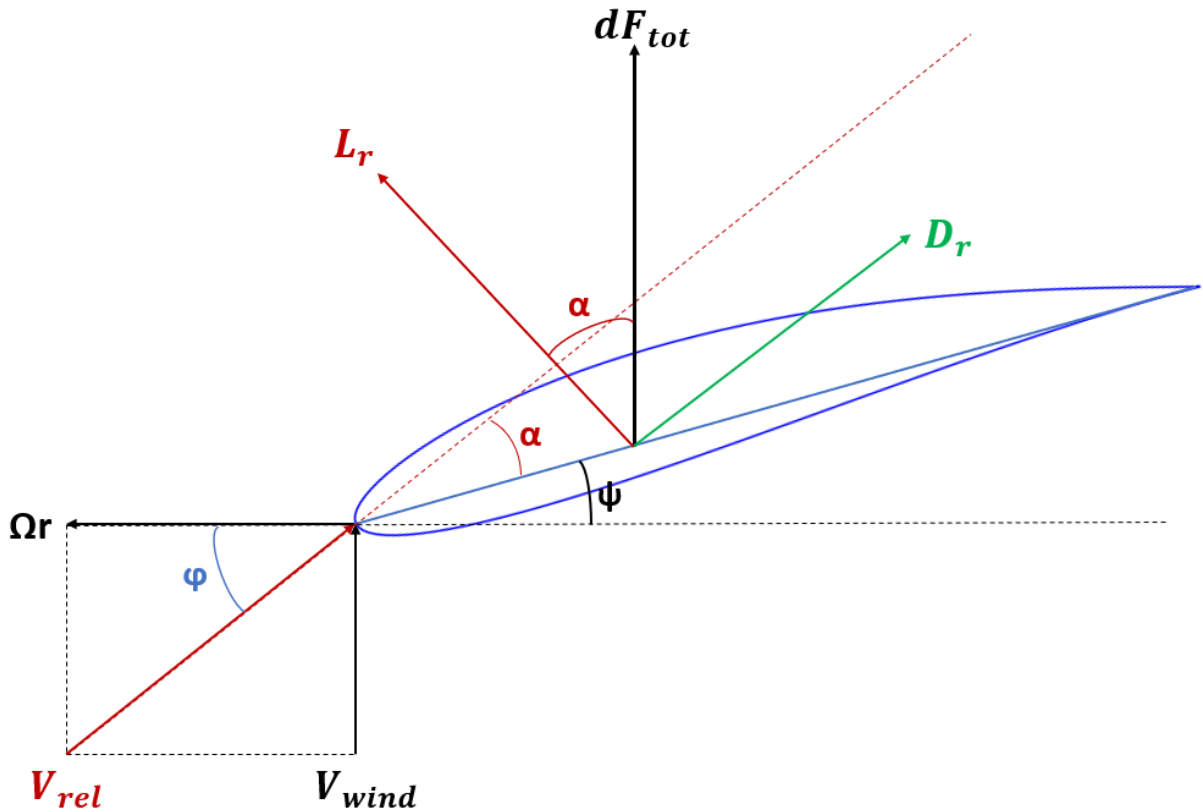
Figure 4.5. Relative wind reference frame.

$$Lsin(\alpha) = Dcos(\alpha) \tag{4-9}$$

$$L_r = \frac{1}{2}\rho A C_l V_{rel}(r)^2 \tag{4-10}$$

$$D_r = \frac{1}{2}\rho A C_D V_{rel}(r)^2 \tag{4-11}$$

$$C_D(r) = C_l(r)tan(\alpha) \tag{4-12}$$

The final check to ensure that the forces being produced are enough to stop the acceleration of the rocket is done by summing the forces produced by each section of the blade in the upward direction. If this F_{tot} equals the weight of the rocket, then the blades will be producing enough lift to maintain a constant velocity. The methodology to calculate the total upward force produced by the autorotation recovery system is outlined in Table 4.2. In this table, the first column lists the equation used to calculate the given parameter. The second column lists the parameters used in the calculation for that step, that are either assumed or known from another source such as a reference. The third column lists parameters that appear in the equation that have been calculated in a prior step. The fourth column lists the values that are unknown in the equation. The fifth column lists the number for the source (from the literature review), where the equation was found, with numbers corresponding the References Section of this report. The last column lists the Equation number (if any) that identities the equation in the original source.

Table 4.2. Autorotation blade design calculations.

Equation	Given/ Assumed	Previously Calculated	Unknowns	Reference	Equation # in Reference
$\sigma = \dfrac{b \cdot c}{\pi \cdot R}$	b, c, R	~	σ	[68]	~
$A_D = \pi \cdot R^2$	R	~	A_D	[68]	~
$dS = c \cdot .01$	c	~	dS	[68]	~
$\Omega R = \sqrt{\dfrac{6 \cdot W}{\sigma \cdot C_l \cdot \rho \cdot A_D}}$	W, R, ρ, C_l	σ, A_D	Ω	[68]	~
$\lambda = \dfrac{\Omega R}{V_w}$	V_w	$\Omega \cdot R$	λ	[68]	~

$\mu = \dfrac{r}{R}$	r, R	~	μ	[66]	3.50a
$C_l = \dfrac{8}{9} \dfrac{1}{\dfrac{b \cdot c \cdot \lambda}{2 \cdot \pi} \sqrt{(1 - \frac{1}{3})^2 + \lambda^2 \cdot \mu^2 [1 + \frac{2}{9(\lambda^2 \cdot \mu^2)}]}}$	b, c	λ, μ	C_l	[66]	3.67a
$V_{rel} = \sqrt{(\Omega r)^2 + (V_w)^2}$	V_w, r	Ω	V_{rel}	[68]	~
$\emptyset = \arcsin(\dfrac{V_w}{\Omega r})$	r, V_w	$\Omega \cdot r$	$\emptyset$	[66]	3.42
$\alpha = \emptyset - \psi$	ψ	$\emptyset$	α	[66]	3.43
$L_r = \dfrac{1}{2} \cdot V_{rel}^2 \cdot A_D \cdot C_l \cdot \rho$	C_l	A_D, V_{rel}	L'	[68]	~
$D_r = \dfrac{1}{2} \cdot V_{rel}^2 \cdot A_D \cdot C_d \cdot \rho$	C_d	A_D, V_{rel}	D'	[68]	~
$C_d = C_l \cdot \tan(\alpha)$	C_l	α	C_d	[68]	~
$dF_{tot} = W = D_r \cdot \sin(\alpha)dS + L_r \cdot \cos(\alpha)dS$	W	D_r, L_r, α	dF_{tot}	~	~

A sample MATLAB® code for the calculation of the blade design is provided in Appendix J. In that section, all the assumed parameters and flight conditions are listed in a table.

4.2.2. Autorotation Analysis

Once the blade is designed, we needed to analyze it to understand its performance. The blade performance can me analyzed using rotational and linear motion Newtonian physics. Each blade element μ is producing a vertical force which we define as dF_{tot} The summation of the force from each of these points along the span of the blade times the number of blades equals the total vertical force F_{TOT}. These forces are dependent upon the rotational and downward velocity of the blade. In order to understand the rotational motion of the recovery system, the torque T must be found using the horizontal force F_{hr} in the Ωr direction from Figure 4.5. Once the total torque is found, the angular acceleration α_t and angular velocity at any time ω be found based on the moment of inertia of the blades I.

$$F_{TOT} = \sum_{r=0}^{R} dF_{tot} \tag{4-13}$$

119

$$F_{hr} = D_r \cos(\alpha) - L_r \sin(\alpha) \tag{4-14}$$

$$T = \sum_{r=0}^{R}(F_{hr}\, r) \tag{4-15}$$

$$\alpha_t = \frac{T}{I} \tag{4-16}$$

$$\omega = \omega_0 + \alpha_t dt \tag{4-17}$$

As for the vertical analysis of the recovery system, a simple application of Newton's 2nd law of motion can find the resultant acceleration, velocity, and height of the rocket on its recovery path.

$$a = \frac{F_{TOT} - F_g}{m_{rocket}} \tag{4-18}$$

$$v = v_0 + adt \tag{4-19}$$

$$h = h_0 + vdt + \frac{1}{2}adt^2 \tag{4-20}$$

4.2.3. Parachute Analysis

When we chose the size of the parachute, we analyzed the force on the main body of the rocket over time when the parachute is deployed. The parachute loads can be analyzed with aerodynamic, Newtonian, and kinematic equations. Eq. 4-21 shows the force of drag F_D the parachute will have for an initial velocity. Where ρ is the density of air, C_D is the coefficient of drag of the parachute, A is the area of the parachute and is 1.19 m^2, and V_0 is the initial velocity of the main body of the rocket when the parachute deploys.

$$F_D = \frac{1}{2}\rho C_D A V_0^2 \tag{4-21}$$

Eq. 4-22 shows the acceleration of the parachute, a. Where F_g is the force of gravity, m is the mass of the main body of the rocket, and F_D is force of drag previously calculated in Eq. (4-21).

$$a = \frac{F_D - F_g}{m} \tag{4-22}$$

Equation (4-23) shows the final descent velocity of the rocket after time t. V_0 is the initial velocity, a is the acceleration of the rocket, and dt is the time step in seconds.

$$V_f = V_0 - adt \tag{4-23}$$

A MATLAB® code was developed for the calculation and analysis of the force the parachute has on the main body when deployed. The code can be found in Appendix K. Table 4.3 outlines the methodology to calculate the force on the main body when the parachute is deployed. Table 4.4, in the results and analysis section, illustrates the parameters we assumed during the analysis, namely V_0, ρ, C_D, and m.

Table 4.3. Parachute force calculations.

Equation	Given/ Assumed	Previously Calculated	Unknowns
$F_D = \frac{1}{2}\rho C_D A V_0^2$	ρ, C_D, A, V_0	~	F_D
$a = \frac{F_D - F_g}{m}$	F_g, m	F_D	a
$V_f = V_0 - adt$	V_0, dt	a	V_f

4.3 Results and Analysis

In our first launch on January 19, 2019, our motors failed to generate enough thrust to lift our rocket off the lift rail. The recovery system was ground tested at the launch site, including the black powder separation with the parachutes packed into rocket body. During the testing, the parachutes ejected from the rocket body and completely unwound from their folded position. Other than ground tests, there was no other way to test the parachutes. Without a launch, we cannot determine if the parachutes would bring both the rocket-body and nosecone to descent velocities for a safe landing. Figure 4.6 shows the force the parachute will exert on the nosecone bulkhead when deployed as a function of time. Equations 4-21 through 4-23 explain the calculations needed to perform the analysis. Table 4.3 shows the parameters we assumed during the analysis. The overall force is in newton's and the analysis was run for 2 seconds. The force the parachute has on the nosecone bulkhead the moment after it is deployed is about 700 N. Over the next couple seconds, the overall force drops exponentially. The range safety officers at the site we launched from said an autorotative system would not be allowed to be part of the launch at most sites in New England. This is due to the smaller size of the launch sites in the New England area and the concern over the rocket drifting a significant distance downrange. If we wanted to use an autorotation system, we would have to travel to a site with a very large field. Even though we were unable to fly an autorotation system, we completed the analysis to design 3D printed blades.

Table 4.4. Assumed parameters of parachute analysis.

Variable	Name	Assumed value (with units)
ρ	Air Density	$1.225 \frac{kg}{m^3}$
C_D	Coefficient of Drag	0.75
m	Mass of the Main Body of the Rocket	3.5 kg
V_i	Initial Velocity When Parachute is Deployed	$49.05 \frac{m}{s}$
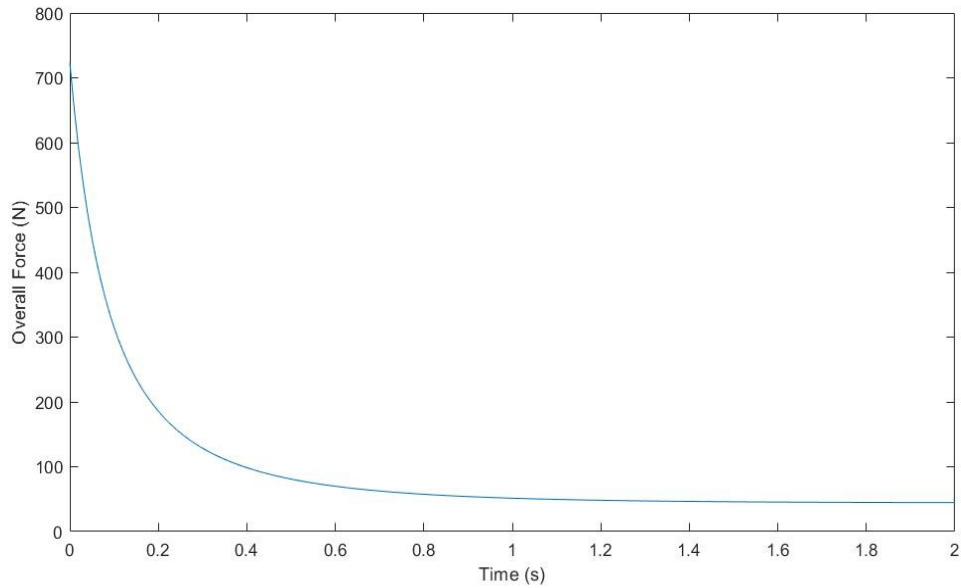
Figure 4.6. Force from parachute on nosecone.

Table 4.5. Assumed parameters of blade design.

Variable	Value	Units
W	4.5	kg
v_w	-6	$\frac{m}{s}$
c	0.0838 or 3.3	m or in
N	3	~
R	0.58 or 22.8	m or in
ΩR	35 or 60	$\frac{m}{s}$ or $\frac{rad}{s}$

Using the equations from Table 4.2, values from Table 4.5, MATLAB®, and XFLR5® we performed analysis and generated plots for parameters for designing an optimized autorotation recovery system. We started the analysis by inputting the equations we determined from literature in Table 4.2 into MATLAB®. The code created in MATLAB® can be found in Appendix J and K. Beginning with the downward velocity, we determined the goal was to get the downward velocity to equal 6 m/s. The downward velocity is the final, terminal velocity the

descending rocket should have with an autorotation recovery system in use. Downward velocity is one of the final parts of the analysis, along with the forces of lift and drag generated by the blades. So, by setting a downward or terminal velocity, we worked backwards through our calculations to generate plots of desired blade characteristics, shown in Figures 4.7 through 4.15. All calculations were performed using MATLAB®. We also started our aerodynamic analysis with the blades in a small rotational velocity less than 1 rad/s, this allows for analysis to begin at angles of attack where the blades will behave as designed and produce torque. The analysis is simplified because the blades have an initial angular velocity instead of having no angular velocity when first released into position by the spring system.
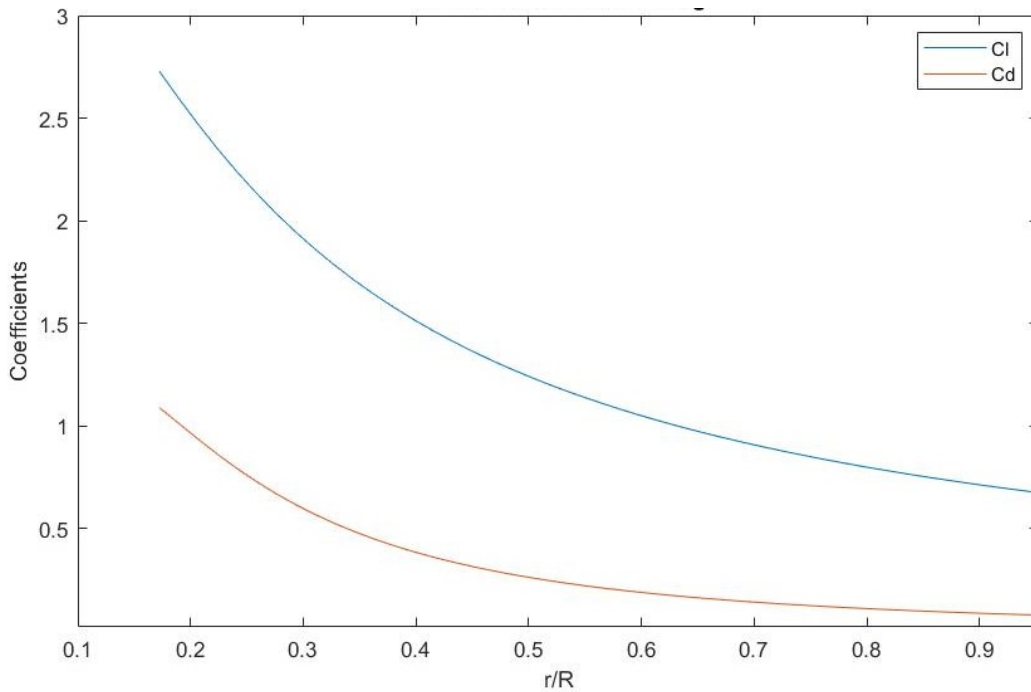
Figure 4.7. Coefficient of lift and drag along the span of the blade. r/*R*=1 corresponds to the point on the blade at the tip.

Figure 4.7 shows the results of Eq. (4-5) and (4-12) which produced the coefficients of lift and drag along the span of the blade. The equations produced coefficients of lift and drag along the span of the blade based on an estimated appropriate rotational speed of 35 m/s or 60 rad/s and

a desired decent velocity of 6 m/s. This rotational speed means that the required coefficients of lift and drag are low enough to be possible at low Reynolds numbers, but the rotational velocity is not so fast that it would take too much time for the blades to spin up.
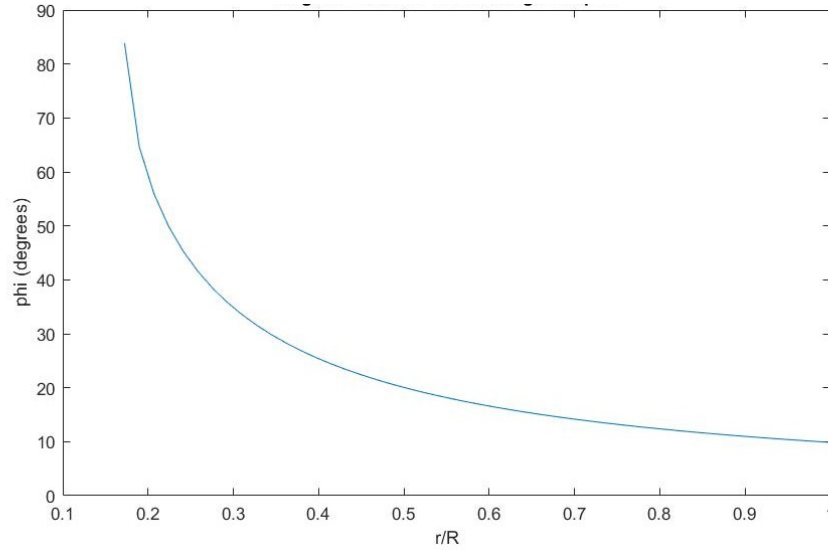
Figure 4.8. Angle of relative wind along the span of the blade. The angle is defined as shown in Figure 4.5.
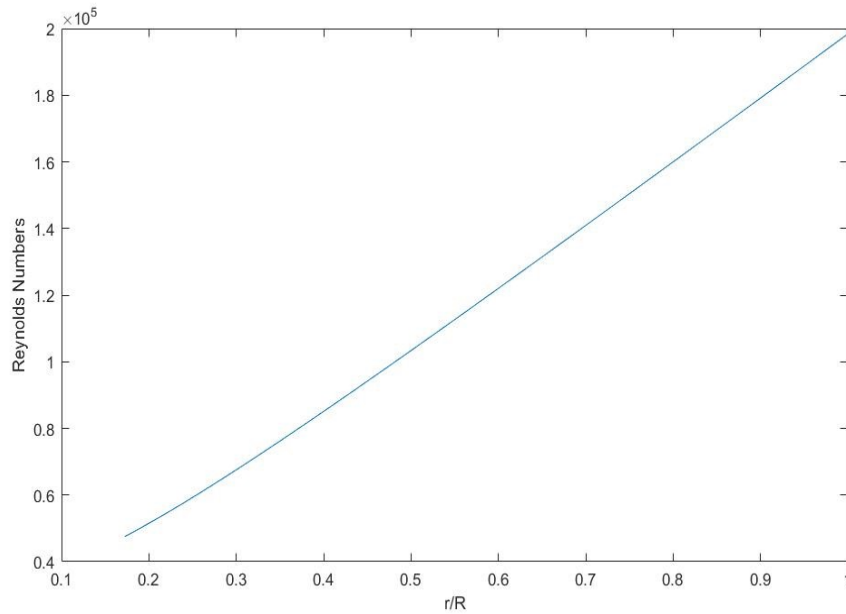
Figure 4.9. Reynolds number at equilibrium speed.

At the final equilibrium conditions, the relative wind at the tip of the rotor blade is at an angle of attack of 9 degrees and a Reynolds number of 200,000. Because the angle of relative wind is based on a sine function in Eq. (4-7), it grows exponentially as it approaches the root of the blade, reaching 90 degrees at a very low Reynolds number of 50,000. Because of this we needed to twist the blades along the span of the blades.
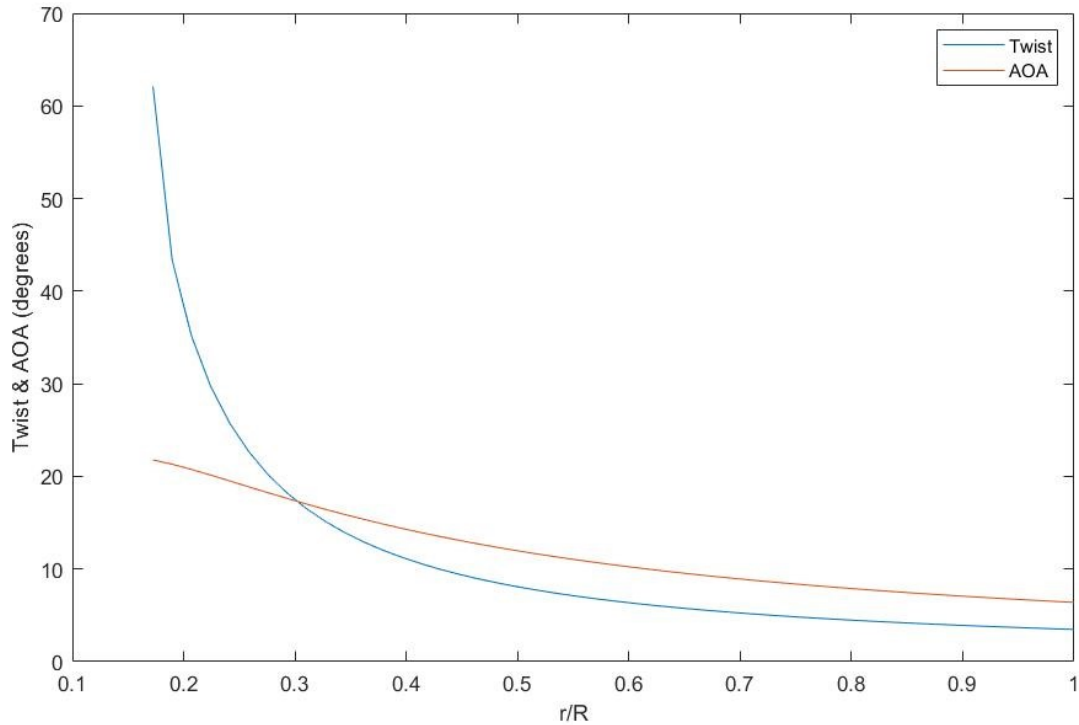
Figure 4.10. Angle of blade twist and angle of attack at equilibrium speed.

Figure 4.10 shows the blades angle of twist phi ψ and angle of attack alpha α, shown in Figure 4.5, versus speed. Once a twisted airfoil is designed, its performance needs to be analyzed using blade element theory, simple aerodynamic principals, and simple Newtonian physics. Because XFLR5 produces separate files for each airfoil and Reynolds number when exporting the simulated wind tunnel data to text documents, we made the simplification of only using a singular airfoil shape, a simple NACA 6420, analyzed at one Reynolds number, 200,000, which was at the top end of our design Reynolds numbers. We still used the calculated angles of optimal twist for the blade in order to maintain reasonable angles of attack that would produce laminar flow over

126

the airfoil. XFLR5 cannot predict turbulent flow. When calculating forces exerted on the descending rocket, we neglected the drag that would be produced by the rocket body and any possible drogue parachute used to pull the recovery system out of the rocket body.

We now present the descent trajectory for the rocket using an autorotation recovery system. The model equations used to calculate this trajectory were presented in Section 4.2.2 and the all the assumed parameters and initial conditions for this sample case result are summarized in Table 4.6 and use the applicable values from Table 4.5 as well. We began with the blades in decent and already spinning because we did not have any aerodynamic data on their behavior at high angles of attack and low velocities. The model we developed is not a physical one because of our inability to replicate induced drag which would drastically reduce the acceleration that the blades are capable of. Because we do not have variable data for each Reynolds number that the blades will experience, the effects of the coefficients of lift and drag do not represent accurate of the airfoils throughout the recovery process. Our model merely shows that the autorotation system would slow the rocket to a predictable velocity, but the accelerations, velocities, and therefore timeline does not represent a physically accurate model.

Table 4.6. Assumed parameters of blade analysis.

Variable	Value	Units
I	4.5	$\dfrac{kg \; m^2}{s}$
v_0	-1	$\dfrac{m}{s}$
ω_0	1	$\dfrac{rad}{s}$
h	457 or 1,500	m or ft
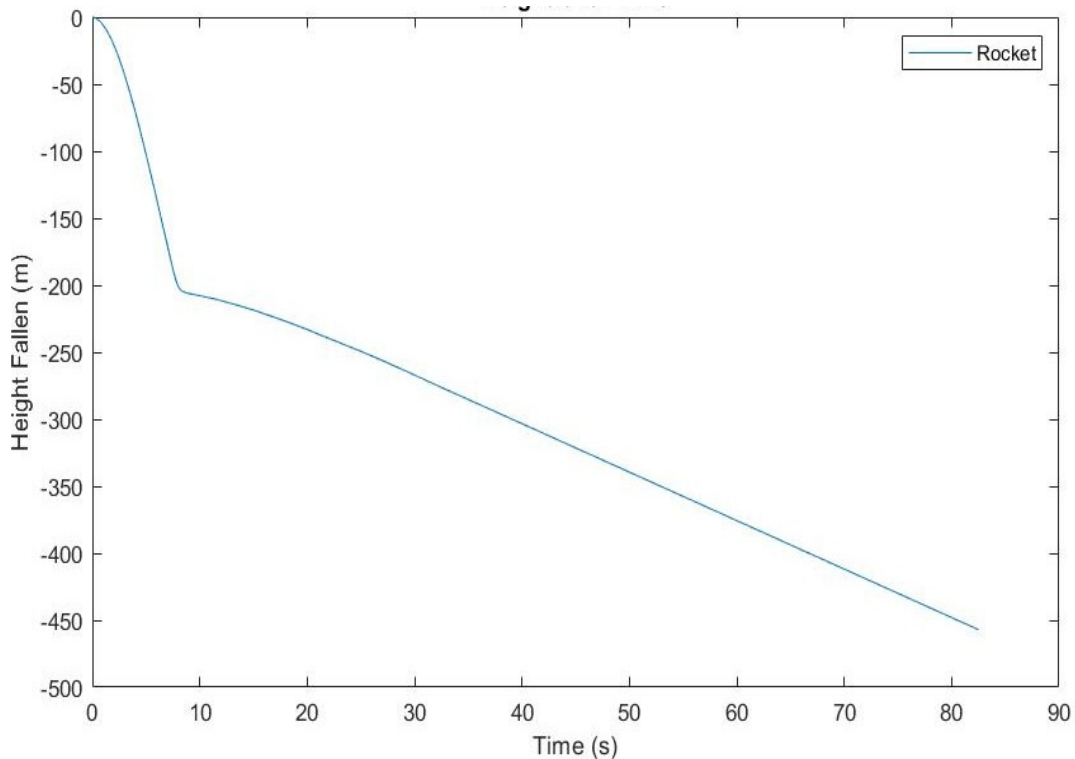
Figure 4.11. Rocket altitude lost as a function of time from deployment.

From Figure 4.11, we can see that a 4.5 kg rocket falling from 1,500 feet or 457 meters will reach the ground after 82 seconds. For the first 210 meters the rocket is falling quite quickly and represents the absolute minimum altitude that the rocket would need to reach in order to safely land using the autorotation recovery method. When accounting for the delay between the rocket apogee and the full deployment of the autorotation system as well as the physical inaccuracies of the model, more height would need to be added to that minimum altitude estimate. The autorotation system would most likely have a larger downward velocity than the 1 m/s that we began our recovery system at.

Figure 4.12 shows the vertical acceleration of the rocket for roughly 85 seconds. The rocket begins at a gravitational -9.81 m/s^2 and quickly begins slowing down rapidly around 8 seconds at which point the lift produced by the blades far exceeded the weight of the rocket. It reaches a maximum acceleration of 4.7 gees which is incredibly high. This acceleration in a physically accurate model would not be as rapid. The blades keep accelerating because of larger coefficients

of lift and higher velocities as the relative wind angle reaches 10º at this point the coefficients of lift begin to shrink and the blades run out of momentum. In this model the jolt only lasts a second but could be enough to snap a shock cord. This rapid acceleration is due to the analysis of the blades not accounting for velocity induced drag which would drastically increase the drag produced by the blades and decrease the blade acceleration. The rocket then stabilizes around 20 seconds and does not accelerate further.
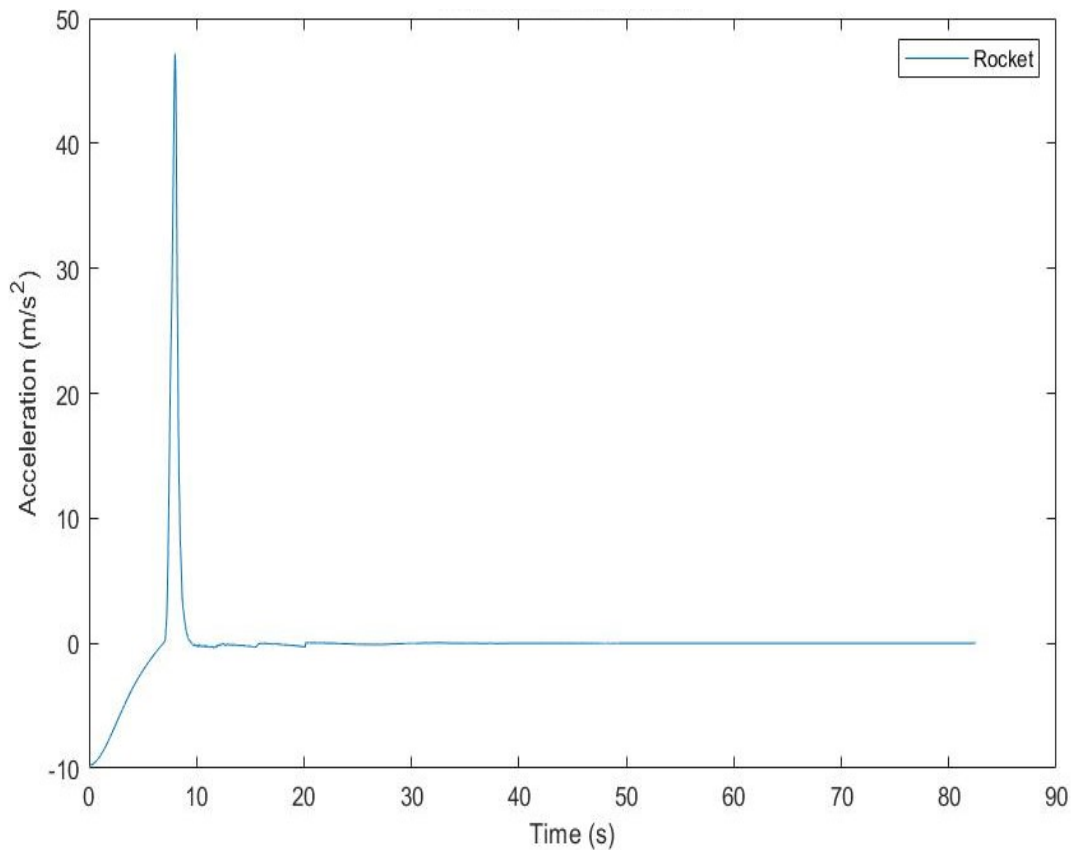
Figure 4.12. Vertical acceleration of rocket as a function of time from deployment.

From Figure 4.13, the maximum velocity of the falling rocket is -35 m/s and reaches a much lower value of -1.5 m/s after the large deceleration the autorotation system produces. The rocket reaches equilibrium at -3.7 m/s because the blade being analyzed is one airfoil and does not follow the coefficients of lift and drag along the span of the blade set though the design

process in Section 4.2.1 and shown in Figure 4.7. In order to increase the equilibrium downward velocity, a blade that produces less lift at the tip should be used. The increased downward velocity would ensure that the rocket does not drift as far during decent.
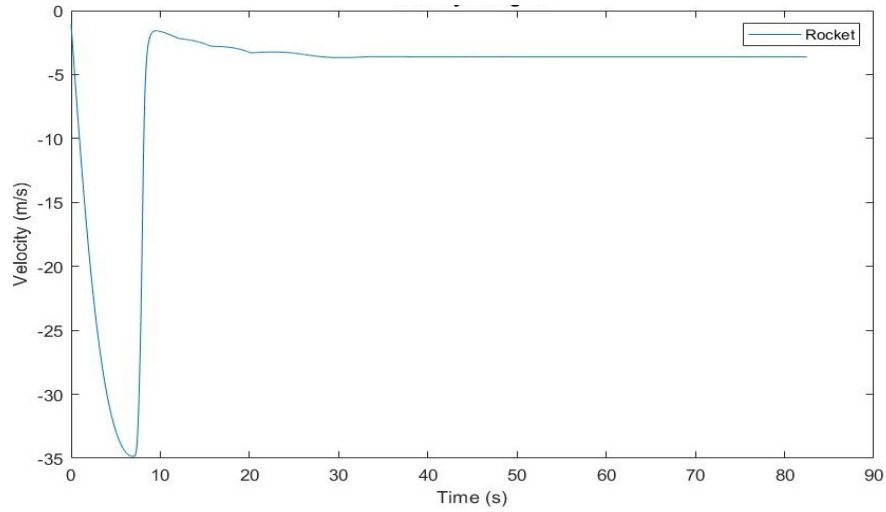
Figure 4.13. Descent velocity of rocket as a function of time from deployment.
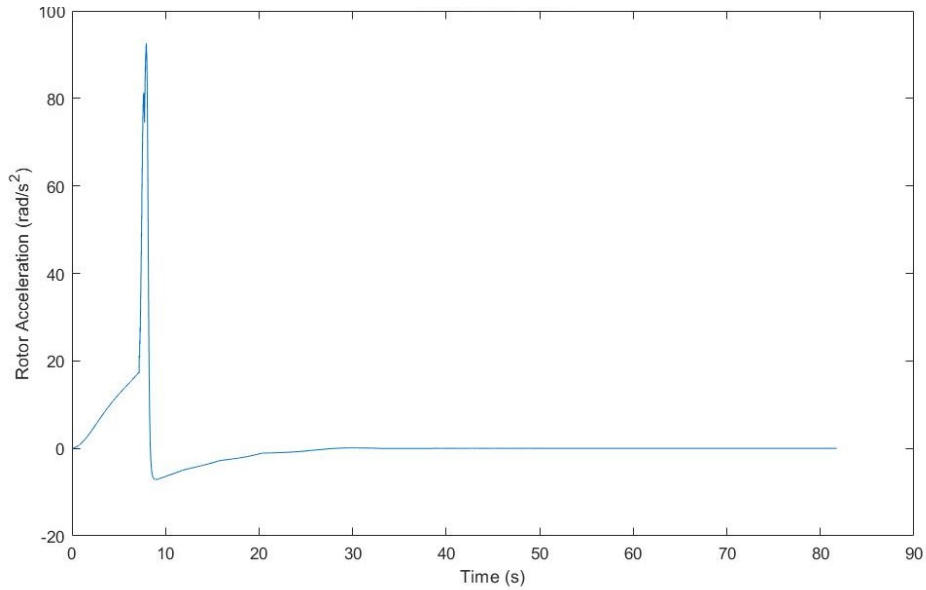
Figure 4.14. Rotor acceleration as a function of time from deployment.
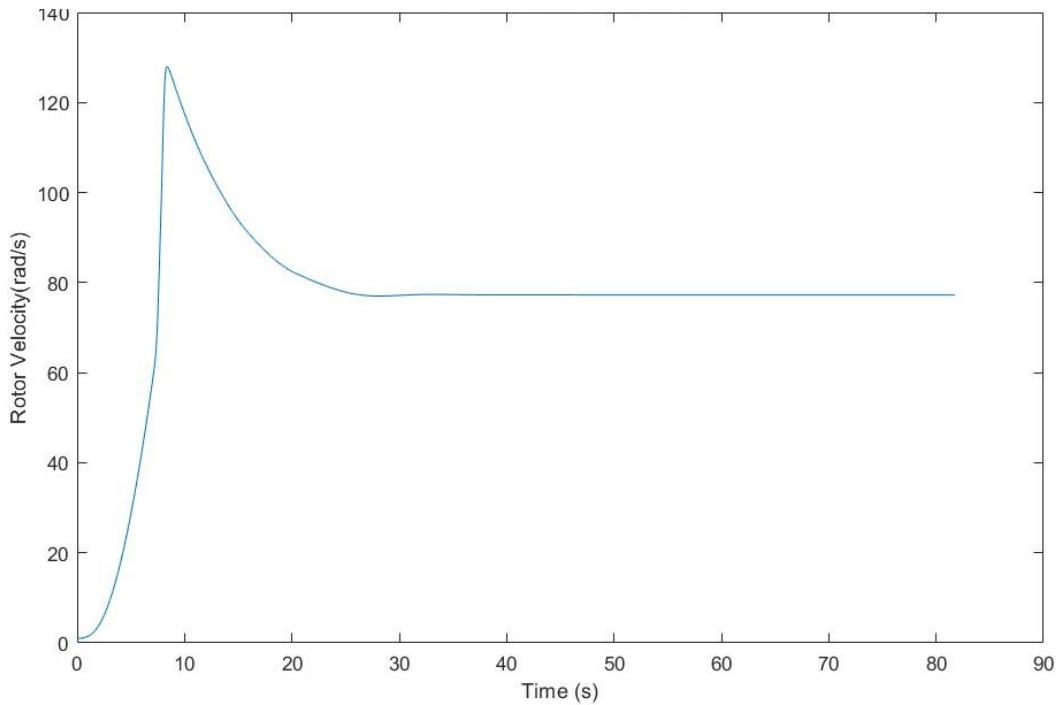
Figure 4.15. Rotor rotational velocity as a function of time from deployment.

In Figures 4.14 and 4.15, we can see that the rotor blades spin up quickly, reaching a maximum acceleration of 80 rad/s² and a maximum angular velocity of 128 rad/s. Because these blades are not the designed for the desired 60 rad/s, the resulting angular velocity is 77 rad/s at the equilibrium condition.

The idea for integrating the autorotation system into the rocket consisted of the blades being packaged inside of our 4-in rocket body attached to a central rotating hub shown in figure 4.16. The hub would be attached to a vertical axel which when ejected is attached to the rocket body via a shock cord. The easiest way to make this work would be to have a one way bearing inside of the hub attached to the axel by industrial hairpins. The blades would need to be folded up, placed inside of the rocket body. When ejected, the blades deploy on a spring hinge system and begin to spin.

131
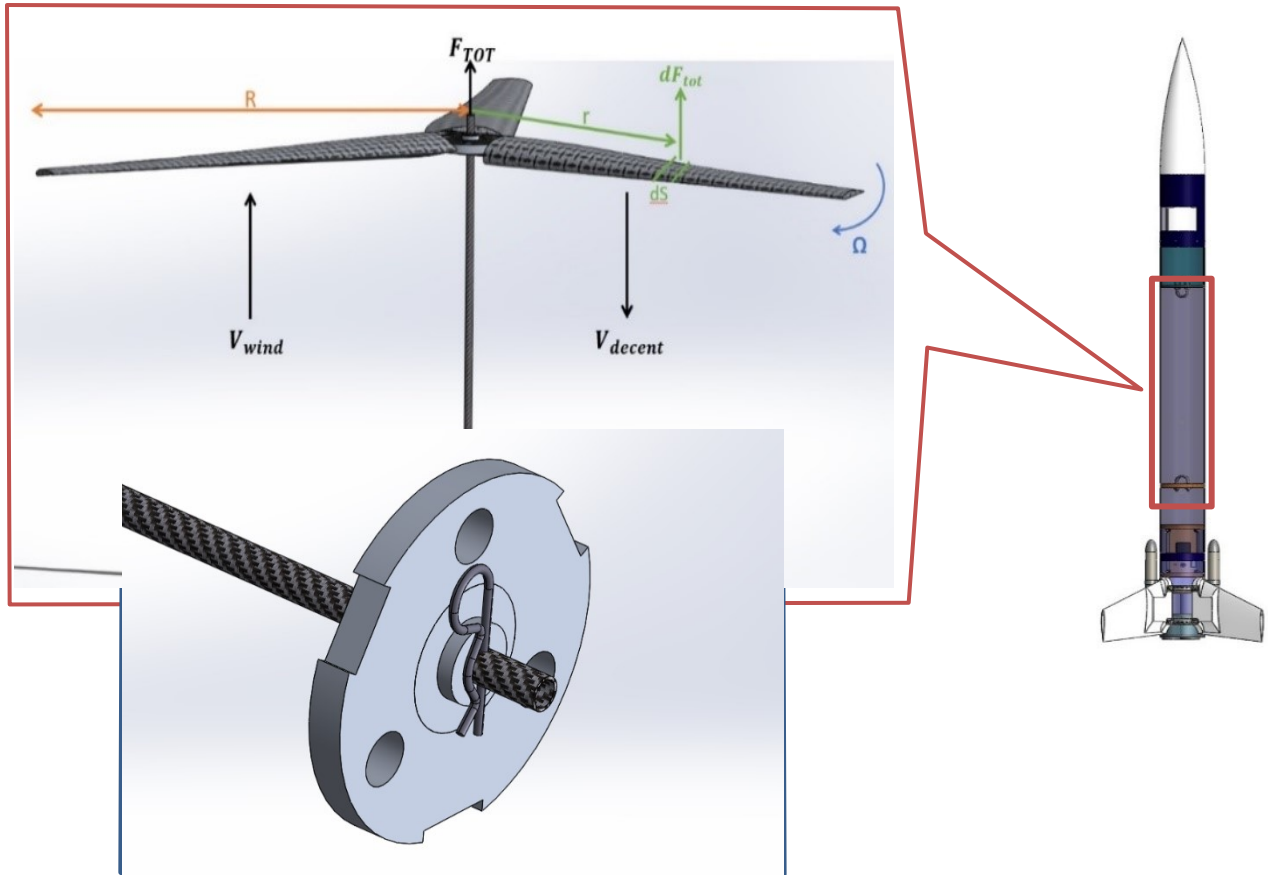
Figure 4.16. Recovery system with central hub.

Chapter 5. Conclusions and Recommendations

5.1 Summary

Overall, this MQP set out to develop novel systems for propulsion, stage separation, and recovery systems of model rocket. We conducted analysis on motor configurations and a heat transfer modeling. We also developed and manufactured a custom CO_2 separation system prototype but did not complete testing. We optimized the electromagnetic stage separation methods used in the WARRIORS I and II MQPs. Finally, we designed an autorotation system for recovering the rocket.

5.2 Conclusions and Future Recommendations

5.2.1 Propulsion System

Motor Clustering

The PSR team attempted to cluster three H motors in parallel in the airframe of the rocket to minimize the airframe length and to investigate the modifications that would need to be made to traditional motor mounts and ignition systems. We successfully designed and manufactured motor mount components to align the clustered H motors within the airframe. We also successfully used a clip whip to attach all three H motors to the launch site ignitor power supply in parallel as a requirement for simultaneous ignition. However, testing the motor cluster propulsion system resulted with a failed ignition and proved motor clustering to be a risky and unreliable propulsion system option. In addition, the current recommendation by the NAR on the required thrust level for each individual motor (5x the weight of the rocket) restricts most motors from being used for clustering depending on the weight of the rocket.

We recommend that motor clustering be considered a low priority when testing innovative rocket systems at a launch, as an unsuccessful ignition can prevent all other rocket systems from being tested. If a team wishes to investigate motor clustering as an advanced propulsion system, they will need to sacrifice other more advanced subsystems to minimize the overall weight of the rocket, as this will allow an individual motor thrust level to exceed that of the NAR recommended thrust level. Also, starting off by using a two-motor cluster will greatly increase the chances of simultaneous ignition at the cost of having only axial symmetry instead of radial symmetry.

Igniter Systems

We investigated three of the most popular model rocket igniter systems - electric match, ignition powder, and pyrogen – and decided to use the electric match igniter for our rocket. This type of igniter consists of high-resistance wire, often nichrome, with a solidified pyrogen along the length which heats up along with the wire when a current is passed through. When the pyrogen heats up enough, it sparks and ignites. The system is analogous to a lightbulb filament, burning when enough current passes through.

We made our own igniters with 32-AWG nichrome wire and QuickBurst's H3-Compound pyrogen dip. After manufacturing the igniters, we tested them to see if they would work with the voltage and current, we planned on launching our rocket with. Overall, the test was a success, but on launch day, the cold temperatures meant more current was needed to heat up the amount of wire in the igniter. When we performed our ground test of the black powder ejection system, the launch site officials directed us to use commercial igniters instead as they were more reliable, and the ground testing went off without further problems.

In the future, it would be wise to have a specific plan to ensure the correct wire length for each igniter and that each igniter has made with the same amount of pyrogen. Had we intended to make more for future launches, we would have made a more detailed procedure, possibly involving weighing the pyrogen added to each wire or making them in a mold, which we recommend to any future teams attempting to make their own igniters. Additionally, we've learned through talking with the launch site officials that many launch sites do not allow the use of homemade igniters at all, and that it's helpful to be in contact with the officials to prepare ahead of time for what they do and do not allow.

0-Dimensional Combustion Model

An attempt to complete a 0-Dimensional (0D) combustion model of the rocket motor proved to be semi-successful. The goal was to create a zero-dimensional model in which a propellant burn rate, from the literature, was used to calculate the mass flow of combustion products into the chamber. The pressure and temperature were to be considered independent variables. The propellant combination was aluminum and ammonium perchlorate, and the products

of combustion were to be determined using the chemical kinetics software package called Cantera. With the composition of the combustion products estimated using Cantera, the mixture properties (e.g. molecular weight, specific heats, etc.) could be determined and used to calculate the minimum throat area required using ideal isentropic flow relations. These relations could also be used to calculate thrust and specific impulse. These results could them be compared with published data for actual hobby motors where available.

While not completed in this project, the model equations are presented. A suggestion for future work on the 0-dimensional model is to consider several different mixtures of the fuel and the oxidizer. Also, a more extensive effort to obtain propellant mixture and estimated operating conditions for hobby motors would be helpful.

Heat Flux Modeling and Simulations

The PSR team attempted to estimate the heat flux through the aluminum casing so that the MSAT team could conduct thermal analysis on the motor body tubes. For the transient heat flux solution, there were many limitations as discussed in the heat flux modeling and simulations results section. An area for future work could be to use a time-dependent conductive heat transfer equation to estimate the heat flux solution. This would capture the temperature change at the boundaries versus time, which add much more complexity as this would turn into a partial differential equation with time and spatial derivatives. Therefore, a more realistic solution approach is to use a partial differential solver software such as COMSOL.

There are also several areas for future work estimating the heat flux in COMSOL. Although the temperature distribution and heat flux were found from purely conductive heat transfer through the solids, adding the convective heat transfer effect in the fluid would change the overall temperature distribution and provide a more accurate model for the combustion process in the motor. However, we were not able to get a working solution using COMSOL. Therefore, an area for future work would be to begin with a simpler COMSOL model and build up complexity gradually. This would eventually include defining the boundary conditions of the model so that convective heat transfer would result from the fluid flow. In addition, there are several model improvements that can be made to more realistically model the motor that we were using for launch. The motor did use a tubular grain as modeled in our current simulation; however, the

propellant grain likely contains around 20% aluminum and 1-5% binder material, which would likely change the thermodynamic properties that were used in the model (pure ammonium perchlorate was used). Therefore, another area for future work would to develop a more accurate estimate of the propellant grain properties to be used in the model. Furthermore, the fluid flow was purely one-dimensional and did not consider the mass flow that was leaving the combustion chamber. This is a much more complicated problem.

5.2.2 Stage Separation Systems

Carbon Dioxide (CO_2) Stage Separation System

We developed a model of the flow of CO_2 out of a cartridge and into the rocket body tube. Based on comparison to Dutton's models of the discharge and charge of pressurized vessels, these models predict reasonable values of the changing pressure in the cartridge during the regime of choked flow. The final pressure in the rocket tube at the end of the choked flow stage is approximately 219,671 Pa (31.9 psi) after 0.063 seconds, which is greater than the necessary pressure to jettison the nosecone 206,288 Pa. When we subtracted the pressure necessary to overcome friction on the nosecone, the pressure differential is 116,804 Pa (16.9 psi). Therefore, based on experimental values gathered from model rocketry resources, the attainable pressure is enough to eject the nosecone during flight [15, 41]. We were unable to test this value because the CO_2 assembly experienced a motor failure and was not moved to the final phase of testing. We recommend this configuration be tested to verify this flow model.

We developed a custom CO_2 stage separation system and we constructed a prototype and performed initial testing. However, the electric drive motor we purchased did not produce enough torque to function as intended and the additional motors did not arrive in time for the conclusion of the project. Therefore, the system was not successfully tested. Each individual part of the system functioned during testing of the magazine or firing mechanism, but they did not function properly as a whole. The biggest challenge that we faced during the design of the system was the amount of force needed to hold down the release button on the magazine when it contained a loaded CO_2 cartridge. The limited size of the rocket body and limited availability of micro-linear actuators able to impart enough force were strong factors that guided our design decisions on the firing

mechanism. If more time was available to test the firing mechanism, our next step would be to test the system with additional motors and then install it into the rocket for separation testing. Regarding future work on the CO_2 separation system, we recommend that future groups reduce the complexity of the system and move.

The material testing planned for this project was not completed due to time constraints and machine unavailability. We recommend that future project teams use our polylactide (PLA) tensile testing specimens to collect the tensile strength of the material. The data collected from the testing can be imported into a custom material in SOLIDWORKS® to perform a more accurate stress analysis of the 3D printed parts.

Due to the failure of the main engine at our attempted launch, the black powder charge was not detonated mid-flight. The overall lesson learned from the range safety officers was that the amount of untested new systems on the rocket was problematic.

Electromagnetic Booster Separation System

We improved the electromagnetic booster separation system by drastically improving its requirements including current and mass. The main reason for the improvement was due to an accurate representation of the equations and models needed for this system. These requirements include the amount of current needed for ejection and the mass needed for the system. By creating a model, which was later tested to be accurate, that portrayed the relationship of electric circuit elements and current, an optimized result can be found. This model could be altered depending on the circuit properties including resistance, capacitance, voltage, etc. By lowering the current needed for successful ejection, the mass was reduced mainly due to the size of the capacitor required.

After creating this model, physical measurements were required to assure the accuracy of the model. By using an oscilloscope, the voltage and the current could be detected in a circuit. By comparing the model and these measured values, a comparison could be made. This comparison proved the reliability of the model. Not only that, but during these tests, successful ejection with the electromagnet could be seen.

Given more time, fully integrating the system in the rocket would have been the next goal. There was not enough time to continue testing the prototype of the electromagnetic system. Further testing would have led to dual electromagnetic activation for more accurate results. Any changes to the system would then be made based on the results of this test. Ultimately, actual testing during rocket flight would prove the capabilities of this system. Since the electromagnetic system was not flight ready by the time of flight it could not be tested.

5.2.3 Recovery System

The concept of an autorotation recovery system can be explored much further than what we were able to in this MQP. Because of the nature of rotating aerodynamic systems, many levels of complexity can be added to the analysis. Our analysis of the autorotation recovery system proves that it is possible to safely land a rocket using deployable autorotation blades and predict its performance. Because of the many simplifications and assumptions made to the analysis, for a truly accurate model of the system more analysis needs to be completed in future projects.

More accurate blade analysis would include: 1) blade geometry with varying chord lengths along the span of the blade, 2) detailed aerodynamic calculations for the forces close to the root of the blades, which were ignored in this project, 3) data on how the airfoils behave whenever they are beyond the stall point, 4) an analysis of the behavior of the tip vortices, and 5) an analysis that takes into account how the Reynolds number affects the recovery performance. Further analysis could include developing an actual blade model that can be analyzed in ANSYS®. This analysis would be much more accurate because of the nature of data produced by XFLR5, which develops different data sets for each Reynold's number, the simplification of having to analyze the entire blade section with the only variables being the differential along the span of the blade and the velocity of rotation of the blade. The entire system could be modeled ANSYS® and data could be gathered on the effects of the central hub and rocket body on the drag that the system produces. A more realistic analysis could even explore how side wind gusts would influence the behavior and stability of the rocket.

Because of the relative lack of previous research into the possibility of recovering a rocket, we attempted to begin an analysis process that could be further explored by more projects. The

ability to recover a rocket using an autorotation system allows for many new capabilities such as controlling landings more accurately through having rotating blades or having softer landings by designing blades that reach the minimum downward velocity just as they approach the ground.

Due to complications at the launch site and advice from range safety officers, multiple unproven systems in one rocket was generally ruled too risky for one flight. In future launches it would be wise to include only one or two experimental systems per launch to mitigate any failure percentages and improve the overall safety of the rocket launch itself.

5.4 Overall Project Broader Impacts

This project has proven the feasibility of creating innovative systems of the field of model rocketry. The systems developed could possibly be commercialized and sold to consumers in the field once the systems have gone through a stringent series of safety tests and possibly more design iterations. The lessons learned from both the successes and failures that happened during this project are immeasurable.

References

1.   Cooper, C., Dings, D., Dohn, P., Fennick, J., Foster, K., George, E., Lapierre, N., Moquin, T., NAG-1901, "Design and Integration of a High-Powered Model Rocket-I," WPI Major Qualifying Project (MQP) report # NAG-1901, May 2019.

2.   Alvarez, A., Gerhardt, G., Kelly, E., O'Neill, J., and Whitehouse, J., MAD-1901, "Design and Integration of a High-Powered Model Rocket-II," WPI Major Qualifying Project (MQP) report # MAD-1901, May 2019.

3.   [Anonymous]. "High power rocketry | National Association of Rocketry" [online] 2018. National Association of Rocketry. Available from: http://www.nar.org/high-power-rocketry-info/. Accessed 9/18/2018.

4.   [Anonymous]. "NAR Certified Motors" [online] 2018. National Association of Rocketry. Available from: http://www.nar.org/standards-and-testing-committee/nar-certified-motors/1. Accessed 9/10/2018.

5.   Stine GH, Stine B. *Handbook of Model Rocketry*. 7th ed. Wiley; 2004. 48-81 p.

6.   Attisano M., Marasca E., and Siciliano I. "Black powder" [online] 2009. University of Torino. Available from: http://lem.ch.unito.it/didattica/infochimica/2008_Esplosivi/BlackPowder.html. Accessed 2/27/2019.

7.   Sutton GP, Biblarz O. *Rocket Propulsion Elements*. Ninth. Hoboken, NJ: John Wiley & Sons, Inc.; 2017.

8.   [Anonymous]. "Rocket motor basics" [online] 2018. Apogee Components, Inc. Available from: https://www.apogeerockets.com/Rocket_Motors/AeroTech_Motors/38mm_Propellant_Kits/38_240_Kits/Aerotech_38mm_Propellant_Kit_H73J-M. Accessed 9/5/2018.

9.   Sarradet, T. "Reloadable composite rocket motor diagram" [online] 2009. Available at https://slideplayer.com/slide/4406026/. Accessed 10/3/2018.

10.   [Anonymous]. "NAR motor testing" [online] 2018. National Association of Rocketry. Available from: http://www.nar.org/nar-motor-testing/. Accessed 9/25/2018.

11.   [Anonymous]. "Thrust curve of I59WN-P Aerotech motor" [online] 2009. National Association of Rocketry Standards and Testing. Available at http://www.nar.org/SandT/pdf/Aerotech/I59WN.pdf. Accessed 10/3/2018.

12. [Anonymous]. "Rocket motor impulse classification" [online] 2018. Rocketry SA. Available at http://www.rocketry.org.za/HighPower_Introduction. Accessed 10/3/2018.

13. Van Milligan, T. "Motor mount diagram" [online] 2018. Apogee Components, Inc. Available at https://www.apogeerockets.com/education/downloads/Newsletter415.pdf Accessed 10/3/2018.

14. Van Milligan T. "How 2-Stage rockets work" [online] 2018. Apogee Components, Inc. Available from: https://www.apogeerockets.com/Tech/How_2-Stage_Rockets_Work. Accessed 9/18/2018.

15. [Anonymous]. "How to size ejection charge" [online] 2018. Huntsville Area Rocketry Association. Available from: http://hararocketry.org/hara/resources/how-to-size-ejection-charge/. Accessed 9/29/2018.

16. [Anonymous]. "Ejection canister caps" [online] 2018. Apogee Components, Inc. Available from: https://www.apogeerockets.com/Ejection_Systems/Ejection_Canisters/Ejection_Canister_Caps_2_pk?zenid=1nivaduf6i3lfr0tbdv0rn9p43. Accessed 12/16/2018.

17. [Anonymous]. "Pyrodex test" [online] 2018. Pratt Hobbies. Available from: http://pratt-hobbies.com/info_pages/pyrodex/pyrotest.htm. Accessed 12/16/2018.

18. [Anonymous]. "About SpaceX" [online] 2019. SpaceX. Available from: https://www.spacex.com/about. Accessed 10/11/2018.

19. Manfredo J. "Properly sizing parachutes for your rockets" [online] 2005. Apogee Components, Inc. Available from: https://apogeerockets.com/education/downloads/Newsletter149.pdf. Accessed 10/10/2018.

20. Van Milligan T. "Selecting the proper size drogue parachute" [online] 2014. Apogee Components, Inc. Available from: https://www.apogeerockets.com/education/downloads/Newsletter361.pdf. Accessed 10/10/2018.

21. Belliss, M., Brayshaw, P., Matook, G., Otterman, A., Sanchez-Torres, A., Moore K., Stechmann, D., Braun, T., JB3-RCK1, "WPI AIAA Research Rocket for the

Investigation and Observation of Recovery and Staging (WARRIORS 1)," WPI Major Qualifying Project (MQP) report # JB3-RCK1, May 2006.

22. [Anonymous]. "Motor clustering information" [online] (2014). Spaceport Rocketry Association. Available at:

http://www.spaceportrocketry.org/Motor%20Clustering.html. Accessed 9/6/2018.

23. [Anonymous]. "Motor mount for three clustered motors" [online] 2018. Rocketarium. Available at: https://www.rocketarium.com/Build/Cluster-Mounts/BT-60-18-3 Accessed 9/27/2018.

24. [Anonymous]. "SLS fact sheet" [online] 2018. NASA. Available from: https://www.nasa.gov/exploration/systems/sls/factsheets.html. Accessed 10/7/2018.

25. Nakka R. "Igniter systems" [online] 2017. Richard Nakka. Available from: https://www.nakka-rocketry.net/igniter.html. Accessed 9/13/2018.

26. Jacobs G. "Amateur rocket motor ignition and igniters" [online] 2018. Jacobs' Rocketry. Available from:

http://www.jacobsrocketry.com/aer/ignition_and_igniters.htm. Accessed 9/13/2018.

27. Cook D. "Model rocket igniter controller" [online] 2018. Robot Room. Available from: http://www.robotroom.com/Rocket-Ignition-System-1.html. Accessed 9/6/2018.

28. Sutton GP, Biblarz O. "Rocket testing" *Rocket Propulsion Elements*. [online] 2018. Available from:

http://www.engineering108.com/Data/Engineering/aeronautical_engineering/Rocket_Propulsion_Elements/26429_20_engineering108.com.pdf. Accessed 9/31/2018.

29. Buhler, J., Coverstone, T., Cummings, N., Fleming, S., Huleatt, T., McDonald, T., Renaud, P., Yocum, M, "WPI AIAA Research Rocket for the Investigation and Observation of Recovery and Staging (WARRIORS 3)," WPI Major Qualifying Project (MQP) report # JB3-RCK3, May 2008.

30. [Anonymous]. "Cantera" [online] 2019. Cantera Developers. Available from: https://cantera.org/. Accessed 3/20/2019.

31. [Anonymous]. "Understand, predict, and optimize physics-based designs and processes with COMSOL Multiphysics® Software [online] 2019. COMSOL, Inc.

2019. Available from: https://www.comsol.com/comsol-multiphysics. Accessed 3/20/2019.

32. Huc, N. "Conjugate heat transfer" [online] 2014. COMSOL. Available from: https://www.comsol.com/blogs/conjugate-heat-transfer/. Accessed 2/10/2019.

33. [Anonymous]. "Aerotech H73J" [online] 2019. Thrustcurve.org: Motor Performance Data Online. Available at http://www.thrustcurve.org/motorsearch.jsp?id=122. Accessed 10/5/2018.

34. Chen C., and McQuaid M. "A skeletal, gas-phase, finite-rate, chemical kinetics mechanism for modeling the deflagration of ammonium perchlorate—hydroxyl-terminated polybutadiene composite propellants" [online] 2016. US Army Research Laboratory. Available from: https://www.arl.army.mil/arlreports/2016/technical-report.cfm?id=7685. Accessed 3/19/2019.

35. Hanson-Parr D. and Parr T. "Thermal properties measurements of solid rocket propellant oxidizers and binder materials as a function of temperature" *Journal of Energetic Materials* [online] 1999. Available at https://www.tandfonline.com/action/showCitFormats?doi=10.1080%2F07370659908 216094. Accessed 2/10/2019.

36. [Anonymous]. "AeroTech announces Economax" [online] 2014. RCS Rocket Motor Components, Inc. Available at http://www.aerotech-rocketry.com/news.aspx?y=2014. Accessed 10/15/2018.

37. [Anonymous]. "Cesaroni I218" [online] 2014. Thrustcurve.org: Motor Performance Data Online. Available at http://www.thrustcurve.org/motorsearch.jsp?id=730. Accessed 10/20/2018.

38. [Anonymous] "Tinder Rocketry's-Peregrine exhaustless CO_2 ejection system" [online] 2016. Available from: https://www.apogeerockets.com/downloads/PDFs/Tinder_Peregrine.pdf. Accessed 9/30/2018.

39. [Anonymous]. "What is airsoft and how does it work?" [online] 2018. AirRattle. Available from: https://www.airrattle.com/How-Airsoft-Works-s/91.htm. Accessed 10/10/2018.

40.   [Anonymous]. "Threaded CO_2 cartridges versus non-threaded CO_2 cartridges" [online] 2017. Genuine Innovations. Available from: https://www.genuineinnovations.com/us/blog/threaded-co2-cartridges-versus-non-threaded-co2-cartridges/. Accessed 10/10/2018.

41.   [Anonymous]. "Ejection charge calculator" [online] 2018. The Nevada AeroSpace Science Associates. Available from: http://www.rimworld.com/nassarocketry/tools/chargecalc/index.html. Accessed 11/12/2018.

42.   [Anonymous]. "Black powder grades - sizes and mesh" [online] 2018. Skylighter, Inc. Available from: https://www.skylighter.com/blogs/fireworks-information/black-powder-grades-sizes-mesh. Accessed 2/27/2019.

43.   [Anonymous]. "Making high-powered black powder" [online] 2018. Skylighter, Inc. Available from: https://www.skylighter.com/blogs/how-to-make-fireworks/making-high-powered-black-powder. Accessed 2/27/2019.

44.   Hall N. "Mass flow choking" [online] 2018. National Aeronautics and Space Administration: Glenn Research Center. Available from: https://www.grc.nasa.gov/www/k-12/airplane/mflchk.html. Accessed 2/27/2019.

45.   Dutton J.C. and Coverdill R.E. "Experiments to study the gaseous discharge and filling of vessels" *The International Journal of Engineering Education*;13(2):123–34 [online] 1997. Available from: https://www.ijee.ie/articles/Vol13-2/ijee924.pdf. Accessed 1/22/2019.

46.   Ardanuy A.F. "Variation of properties during a vessel discharge". *URJ-UCCS Undergrad Res J UCCS,* 9(2):33–40. [online] 2016. Available from: http://ojs.uccs.edu/index.php/urj/article/view/213. Accessed 1/30/2019.

47.   Caron, R. Dempsey, S., Niles, R., Behlman, N., JB3-RCK2, "WPI AIAA Research Rocket for the Investigation and Observation of Recovery and Staging (WARRIORS 2)," WPI Major Qualifying Project (MQP) report # JB3-RCK2, May 2007.

48.   [Anonymous]. "Permanent magnet products" [online] 2005. Stanford Magnets Company. Available: http://www.standfordmagnets.com/magnet/html. Accessed 10/15/2018.

49. [Anonymous]. "Compressibility factor" [online] 2019. Brigham Young University Ira A. Fulton College of Engineering. Available from: https://www.et.byu.edu/~rowley/ChEn273/Topics/Mass_Balances/Single_Phase_Syst ems/Compressibility.htm. Accessed 2/27/2019.

50. Lemmon E.W., McLinden M.O., and Friend D.G. Thermophysical properties of fluid systems in NIST Chemistry WebBook, NIST Standard Reference Database Number 69, Eds. P.J. Linstrom and W.G. Mallard, National Institute of Standards and Technology, Gaithersburg MD, 20899, https://doi.org/10.18434/T4D303. Accessed February 27, 2019.

51. Greene, C. "Compressibility Factor" V 1.2.0.0. [online] 2012. [MATLAB® source code]. https://in.mathworks.com/matlabcentral/fileexchange/35874-compressibility-factor-calculator. Accessed February 25, 2019.

52. [Anonymous]. "Ratios of specific heat of gases" [online] 2003. Engineering ToolBox. Available from: https://www.engineeringtoolbox.com/specific-heat-ratio-d_608.html. Accessed February 28, 2019.

53. [Anonymous]. "Real gases" [online] 2019. York University: Department of Chemistry. Available from: http://www.chem.yorku.ca/courses/chem1000/notes/bw/3_per_page/RealGasesBW3. PDF. Accessed February 28, 2019.

54. Hall N. "Isentropic flow equations" [online] 2018. National Aeronautics and Space Administration: Glenn Research Center. Available from: https://www.grc.nasa.gov/www/k-12/airplane/isentrop.html. Accessed February 28, 2019.

55. [Anonymous]. "Series 223 - high pressure solenoid valve - 2 way – ASCO" [online] 2019. Available from: https://www.shimadzu.com/an/industry/petrochemicalchemical/n9j25k00000pyu05. . Accessed February 20, 2019.

56. [Anonymous]. "Tensile test methods for plastics: ASTM D638" [online] 2019. Shimadzu Corporation. Available from: https://www.shimadzu.com/an/industry/petrochemicalchemical/n9j25k00000pyu05.ht mlhtml. Accessed February 20, 2019.

57.   [Anonymous]. "Universal testing systems – Instron" [online] 2019. Available from: https://www.instron.us/en-us/products/testing-systems/universal-testing-systems. Accessed 3/15/2019.

58.   Kramer, L. and Young, H. D., *Sears & Zemansky's University Physics, 14th Edition Young and Freedman*, San Francisco, CA: Pearson, 2016.

59.   Kaplan B.Z. "A new interpretation of the relationship existing between demagnetizing factor and inductance". *IEEE Transactions on Magnets*. 1994;30(5):2788–94.

60.   Barnard, J. "BPS.space" [online] 2018. 2018 [cited 2018 Oct 10]. Barnard propulsion systems LLC. Available from: https://bps.space/. Accessed 10/10/2018.

61.   Hudson G. "Space future - The ROTON concept and its unique operations" [online] 1995. Available from: http://www.spacefuture.com/archive/the_roton_concept_and_its_unique_operations.s html. Accessed 9/19/2018.

62.   [Anonymous]. "Gyro Chaser competition helicopter style rocket" [online] 2018. Available from: https://www.apogeerockets.com/Rocket-Kits/Skill-Level-4-Model-Rocket-Kits/Gyro-Chaser. Accessed 9/30/2018.

63.   Rice L. "KOPTER Kopter rotor-recovery rocket #RK08" [online] 2018. Available from: http://www.oldrocketplans.com/kopter/kop_RK08/kop_RK08.htm. Accessed 9/30/2018.

64.   Maurer K., Valenti A., Zaccarine S., Le J., and Dennehy J. "Project Hummingbird: recovery of a rocket using autorotation" [online] 2018. Discovery Day - Daytona Beach. Available from: https://commons.erau.edu/discovery-day/db-discovery-day-2018/poster-session/37. Accessed 9/19/2018.

65.   Smith E.H. "Autorotating wings: an experimental investigation" *J Fluid Mech*; 50(03):513 [online] 1971. Available from: http://www.journals.cambridge.org/abstract_S0022112071002738. Accessed 9/26/2018.

66.   Burton T., Sharpe D., Jenkins N., and Bossanyi E. *Wind Energy Handbook* [online]. West Sussex: John Wiley & Sons, Inc.; 2001. Available from:

http://library.uniteddiversity.coop/Energy/Wind/Wind_Energy_Handbook.pdf. Accessed 12/12/2018.

67. [Anonymous]. "Force vectors in vertical autorotation descent" [online] 2018. FlightLearning.com. Available from: https://www.danubewings.com/autorotation-hovering-autorotation/. Accessed 10/10/2018.

68. Filippone A. "Flight performance of fixed and rotary wing aircraft" [online] 2006. Washington, DC: American Institute of Aeronautics and Astronautics, Inc.; 2006. Available from: http://arc.aiaa.org/doi/book/10.2514/4.478390. Accessed 2/28/2019.

69. Riccardi F. and Possamai R. "Conceptual design of a high-speed variable configuration compound helicopter" [online] 2015. Available from: https://www.researchgate.net/publication/277403396_Conceptual_Design_of_a_High-Speed_Variable_Configuration_Compound_Helicopter. Accessed 12/5/2018.

70. Giguère P. and Selig M.S. "Design of a tapered and twisted blade for the NREL combined experiment rotor" [online] 1998. Available from: http://www.doe.gov/bridge/home.html. Accessed 2/28/2019.

Appendix A: Impulse-Mass Trade Study

I Motors	Manufacturer	Total Impulse (N-s)	Total Mass (g)	Impulse/Mass (N-s/g)	Max Cluster (<640 N-s)
I49N	Aerotech	383	398	0.962	1
I180W	Aerotech	326	385	0.847	1
I161W	Aerotech	328.7	385	0.854	1
I218R	Aerotech	330	370	0.892	1
I245G	Aerotech	334.1	365	0.915	1
I357T	Aerotech	342.8	364	0.942	1
I55	Cesaroni	394.6	437	0.903	1
I170	Cesaroni	382	392	0.974	1
I212	Cesaroni	364	475	0.766	1
I236	Cesaroni	338	394	0.858	1
Average:				0.891	

H Motors	Manufacturer	Total Impulse	Total Mass (g)	Impulse/Mass (N-s/g)	Max Cluster
H999N	Aerotech	320	331	0.967	2
H170M	Aerotech	319.9	330	0.969	2
H112J	Aerotech	261.1	385	0.678	2
H110	Cesaroni	269	325.3	0.827	2
H400	Cesaroni	255	283.6	0.899	2
H123	Cesaroni	232	297	0.781	2
H100	Cesaroni	286	327	0.875	2
H130W	Aerotech	210	237	0.886	3
H669N	Aerotech	221	252	0.877	2
H242T	Aerotech	231.7	279	0.83	2
Average:				0.859	

G Motors	Manufacturer	Total Impulse	Total Mass (g)	Impulse/Mass (N-s/g)	Max Cluster
G58	Cesaroni	137	213	0.643	4
G118	Cesaroni	159	188	0.846	4
G185	Cesaroni	128	188	0.681	4
G54	Cesaroni	159.1	198.2	0.803	4
G125	Cesaroni	159	194.5	0.802	4
G79W	Aerotech	108.6	158	0.687	5
G77R	Aerotech	105	155	0.677	6
G25W	Aerotech	109.5	170	0.644	5
G104T	Aerotech	81.5	136	0.599	7
G54W	Aerotech	85	141	0.603	7
Average:				0.699	

Appendix B: Program Cost Breakdown

	Total Budget	Order #	Description	Cost	
HPR MQP Budgeting Management					
MSAT	$ 2,000.00	1	ARR- Tube	$	161.29
		2	West Systems	$	100.84
		3	McMaster Carr	$	23.45
		4	GiantLeap	$	33.06
		5	Amazon-Cameras	$	69.30
		Con.1	McMaster pt2 (With FDC)	$	36.68
		6	DigiKey	$	112.72
		7	Strain Gauge Updates - Digikey	$	83.56
			Remainder:	$	1,379.10
PSR	$ 2,000.00	1	Evike- Magazine	$	27.00
		2	Apogee	$	144.67
		6	McMaster	$	32.69
		7	ServoCity	$	9.99
		5	Apogee2: Fire items	$	89.62
		MSAT 6	DigiKey Magnet Stuff	$	31.11
		9	Mouser Transistors	$	9.90
		11	Adafruit Motor Drivers (really Digike	$	7.50
		13	McMaster: Garolite + Magnet Wire	$	39.54
		8	H73J Motors - Apogee	$	152.55
		10a	MotoJoe End Closures (x3 + x1) aft	$	159.77
		10b	OffWeGo Aft Closure (x1)	$	45.20
		14	Sparkfun CO2 motors	$	43.84
		15	Apogee- CTI Motors	$	232.39
			Remainder:	$	974.23
FDC	$ 1,250.00	1	McMaster-Wire/Rod	$	26.03
		4	CopperHill-MegaCore	$	40.95
		3	Adafruit-SD and IMU	$	62.35
		2	Sparkfun-RF Transmitter	$	4.95
		5	ServoCity Fin Servos	$	166.99
			Remainder:	$	948.73
			Total Spent	$	1,947.94
Total	$ 5,250.00		Total Remainder:	$	3,302.06

Appendix C: Master Gantt Chart

PSR Gantt Chart

| | | | | Project Start: | Thu, 8/23/2018 |
| | | | | Display Week: | 2 |

TASK	PRIORITY	ASSIGNED TO	PROGRESS	START	END
Propulsion		JT, MH, VL			
Heat Flux Calculations	High	JT	100%	11/14/18	2/28/19
Chemical formulation/grain configuration/model in COMSOL	Medium	JT	90%	9/14/18	2/28/19
0-D analysis of combustion, nozzle flow, and thrust estimation	Medium	VL, MH	90%	1/20/19	2/28/19
Analyze COMSOL simulation	Medium	JT	100%	1/20/19	2/28/19
Research System Idea for clustered main motor	Medium	JT	100%	9/5/18	10/5/18
Research and Order Pyrogen and Igniter Wires	High	VL	100%	9/14/18	11/15/18
Order H motor casings and caps	High	JT	100%	9/24/18	10/8/18
Order I motor casings and caps	High	JT	100%	1/15/19	2/2/19
Motor uncertainty/Contact TRA for motor statistics uncertainty	Medium	JT	100%	9/19/18	10/10/18
Create composite thrust curve for other teams	Medium	JT	100%	9/24/18	10/15/18
Research ignition system for clustered motors	Medium	VL	100%	9/24/18	10/8/18
Analyze Ignition Test Results	High	JT, MH	100%	11/30/18	2/28/19
Test Ignition System	High	JT, MH, VL	100%	11/7/18	2/28/19
Construct Ignition system	High	JT	100%	10/25/18	2/28/19
Hand-drawn conceptual drawings of motor mount	High	JT, MH, VL	100%	9/24/18	10/8/18
Physical design and construct motor mount	High	JT, MH, VL	100%	10/7/18	10/28/18
Stage Separation					
CO₂ Separation		SH, NS			
Model of CO2 Systems	Medium	NS	100%	9/10/18	2/20/19
Step-by-step conceptual drawing	High	SH,NS	100%	9/17/18	9/20/18
Research systems that are similar to CO2 Sep & parts similar to Apogee kit	Medium	NS	100%	9/17/18	9/20/18
Purchase CO2 parts	Medium	NS	100%	10/3/18	11/28/18
Construct CO2 System - Machine threaded rod (turn down, hole for grub screw) (Dependent on part arrival	High	SH, NS	100%	10/23/18	1/25/19
CO2 Transient Flow Model	High	SH	100%	9/17/18	2/25/19
CO2 Nose cone Force Test	Medium	SH	100%	9/12/18	10/3/18
Black Powder Backup Calculations	Low	SH	100%	9/17/18	9/21/18

Task	Priority	Assignee	%	Start	End
Black Powder Construction	Low	SH, NS	100%	12/3/18	12/14/18
Sizing and mass estimate	Medium	SH, NS	100%	9/24/18	2/20/19
Design firing systems	High	SH, NS	100%	10/22/18	11/8/18
Leak Proofing Magazine	High	SH, NS	100%	10/22/18	10/27/18
CO2 Separation Testing	High	SH, NS	25%	1/27/19	
PLA Material Testing	Medium	SH, NS	50%	2/1/19	
Leak Testing - Leak Testing in water - Long term leak testing	High	SH, NS	100%	10/7/18	10/7/18
Electromagnetic Booster Separation					
Electromagnetic Calculations - Determing Circuit Current, Capacitance, Resistance, Inductance, etc..	High	NLF & VL & JT	100%	9/17/18	12/1/18
Physical and functional layout of electromagnetic system -Design the circuit including all circuit components	High	NLF, VL, SH	100%	11/5/18	12/14/18
Materials comparison for electromagnetic system - Confirm solenoid core, wire AWG, garolite, permanent magnet	Medium	NLF	100%	11/5/18	12/14/18
Sizing and mass estimate - Give Controls and MSAT dimensions and mass of system to help their analysis	High	VL & NLF	100%	11/5/18	2/15/19
Purchasing Parts - Purchase all parts for breadboarding, testing, and construction of the circuit	Low	NLF	100%	11/14/18	12/5/18
Construction of Ground Test Electromagnetic System - Construct the prototype for separation	Low	NLF, VL	100%	12/1/18	2/25/19
Write Electromagnetic Testing Plan - Prepare for testing system by writing procedures - provide timelines, procudes, lists.	Medium	NLF, VL	100%	11/20/18	1/23/19
Breadboarding - test circuit to assure calculation results. - Make any changes needed to assure successful seperation	Medium	NLF, JT, VL	100%	11/20/18	2/25/19
COMSOL Model of Electromagnetic Coil -Develop CAD model in COMSOL -Analyze results and compare to theoretical	Medium	NLF, JT	100%	1/9/18	2/22/19
Manufacture Steel Rods for Electromagnet Separation Sytem	High	NLF	100%	1/9/18	2/6/19
Electromagnetic Separation Testing - Using constructed system, perform ground testing to create reliable results	High	NLF, VL	100%	11/20/18	2/25/19
Recovery					
Central Hub/Axis					
Physical design	High	JF	100%	9/1/18	2/2/19
Work through and research Blade Calculations/ propellar theory	High	CM & JF	100%	9/14/18	2/22/19
Modeling	High	JF	100%	9/14/18	2/20/19
Rocket Descent Rates for Autorotation	High	JF	100%	12/1/18	2/20/19
Rocket descent rates	Medium	CM	100%	9/10/18	11/5/18
Sizing and mass estimate	High	CM & JF	100%	9/19/18	12/5/18
Determine if method for calculation and design of blades is a go or no go	High	CM & JF	100%	11/8/18	1/24/19
Create Flow Chart	High	CM & JF	100%	1/10/19	1/25/19
Parachutes					
Booster Descent rates/ parachute sizing	High	CM	100%	10/10/18	10/20/18
Purchase Parachutes	Medium	CM	100%	10/15/18	10/25/18
Deliver controls team equations of motion	Low	CM	100%	11/9/18	11/19/18
Integrate Parachutes/Flame retardant cloth into rocket	Medium	CM & JF	100%	12/8/18	12/8/18
Drogue parachute calculations/ sizing	Medium	CM	100%	9/10/18	9/20/18

151

Project Start: Thu, 8/23/2018
Display Week: 10

Oct 22, 2018 | Oct 29, 2018 | Nov 5, 2018 | Nov 12, 2018 | Nov 19, 2018 | Nov 26, 2018 | Dec 3, 2018 | Dec 10, 2018

TASK	PRIORITY	ASSIGNED TO	PROGRESS	START	END
Propulsion		JT, MH, VL			
Heat Flux Calculations	High	JT	100%	11/14/18	2/28/19
Chemical formulation/grain confirguration/model in COMSOL	Medium	JT	90%	9/14/18	2/28/19
0-D analysis of combustion, nozzle flow, and thrust estimation	Medium	VL, MH	90%	1/20/19	2/28/19
Analyze COMSOL simulation	Medium	JT	100%	1/20/19	2/28/19
Research System Idea for clustered main motor	Medium	JT	100%	9/5/18	10/5/18
Research and Order Pyrogen and Igniter Wires	High	VL	100%	9/14/18	11/15/18
Order H motor casings and caps	High	JT	100%	9/24/18	10/8/18
Order I motor casings and caps	High	JT	100%	1/15/19	2/2/19
Motor uncertainty/Contact TRA for motor statistics uncertainty	Medium	JT	100%	9/19/18	10/10/18
Create composite thrust curve for other teams	Medium	JT	100%	9/24/18	10/15/18
Research ignition system for clustered motors	Medium	VL	100%	9/24/18	10/8/18
Analyze Ignition Test Results	High	JT, MH	100%	11/30/18	2/28/19
Test Ignition System	High	JT, MH, VL	100%	11/7/18	2/28/19
Construct Ignition system	High	JT	100%	10/25/18	2/28/19
Hand-drawn conceptual drawings of motor mount	High	JT, MH, VL	100%	9/24/18	10/8/18
Physical design and construct motor mount	High	JT, MH, VL	100%	10/7/18	10/28/18
Stage Separation					
CO₂ Separation		SH, NS			
Model of CO2 Systems	Medium	NS	100%	9/10/18	2/20/19
Step-by-step conceptual drawing	High	SH,NS	100%	9/17/18	9/20/18
Research systems that are similar to CO2 Sep & parts similar to Apogee kit	Medium	NS	100%	9/17/18	9/20/18
Purchase CO2 parts	Medium	NS	100%	10/3/18	11/28/18
Construct CO2 System - Machine threaded rod (turn down, hole for grub screw) (Dependent on part arrival	High	SH, NS	100%	10/23/18	1/25/19
CO2 Transient Flow Model	High	SH	100%	9/17/18	2/25/19
CO2 Nose cone Force Test	Medium	SH	100%	9/12/18	10/3/18
Black Powder Backup Calculations	Low	SH	100%	9/17/18	9/21/18

152

Task	Priority	Assigned	%	Start	End
Black Powder Construction	Low	SH, NS	100%	12/3/18	12/14/18
Sizing and mass estimate	Medium	SH, NS	100%	9/24/18	2/20/19
Design firing systems	High	SH, NS	100%	10/22/18	11/8/18
Leak Proofing Magazine	High	SH, NS	100%	10/22/18	10/27/18
CO2 Separation Testing	High	SH, NS	25%	1/27/19	
PLA Material Testing	Medium	SH, NS	50%	2/11/19	
Leak Testing - Leak Testing in water - Long term leak testing	High	SH, NS	100%	10/7/18	10/7/18

Electromagnetic Booster Separation

Task	Priority	Assigned	%	Start	End
Electromagnetic Calculations - Determing Circuit Current, Capacitance, Resistance, Inductance, etc..	High	NLF & VL & JT	100%	9/17/18	12/1/18
Physical and functional layout of electromagnetic system -Design the circuit including all circuit components	High	NLF, VL, SH	100%	11/5/18	12/14/18
Materials comparison for electromagnetic system - Confirm solenoid core, wire AWG, garolite, permanent magnet	Medium	NLF	100%	11/5/18	12/14/18
Sizing and mass estimate - Give Controls and MSAT dimensions and mass of system to help their analysis	High	VL & NLF	100%	11/5/18	2/15/19
Purchasing Parts - Purchase all parts for breadboarding, testing, and construction of the circuit	Low	NLF	100%	11/14/18	12/5/18
Construction of Ground Test Electromagnetic System - Construct the prototype for seperation	Low	NLF, VL	100%	12/1/18	2/25/19
Write Electromagnetic Testing Plan - Prepare for testing system by writing procedures - provide timelines, procudes, lists.	Medium	NLF, VL	100%	11/20/18	1/23/19
Breadboarding - test circuit to assure calculation results. - Make any changes needed to assure successful seperation	Medium	NLF, JT, VL	100%	11/20/18	2/25/19
COMSOL Model of Electromagnetic Coil -Develop CAD model in COMSOL -Analyze results and compare to theoretical	Medium	NLF, JT	100%	1/9/18	2/22/19
Manufacture Steel Rods for Electromagnet Separation Sytem	High	NLF	100%	1/9/18	2/6/19
Electromagnetic Separation Testing - Using constructed system, perform ground testing to create reliable results	High	NLF, VL	100%	11/20/18	2/25/19

Recovery

Central Hub/Axis

Task	Priority	Assigned	%	Start	End
Physical design	High	JF	100%	9/1/18	2/2/19
Work through and research Blade Calculations/ propellar theory	High	CM & JF	100%	9/14/18	2/22/19
Modeling	High	JF	100%	9/14/18	2/20/19
Rocket Descent Rates for Autorotation	High	JF	100%	12/1/18	2/20/19
Rocket descent rates	Medium	CM	100%	9/10/18	11/5/18
Sizing and mass estimate	High	CM & JF	100%	9/19/18	12/5/18
Determine if method for calculation and design of blades is a go or no go	High	CM & JF	100%	11/8/18	1/24/19
Create Flow Chart	High	CM & JF	100%	1/10/19	1/25/19

Parachutes

Task	Priority	Assigned	%	Start	End
Booster Descent rates/ parachute sizing	High	CM	100%	10/10/18	10/20/18
Purchase Parachutes	Medium	CM	100%	10/15/18	10/25/18
Deliver controls team equations of motion	Low	CM	100%	11/9/18	11/19/18
Integrate Parachutes/Flame retardent cloth into rocket	Medium	CM & JF	100%	12/8/18	12/8/18
Drogue parachute calculations/ sizing	Medium	CM	100%	9/10/18	9/20/18

PSR Gantt Chart

Dec 17, 2018 | Dec 24, 2018 | Dec 31, 2018 | Jan 7, 2019 | Jan 14, 2019 | Jan 21, 2019 | Jan 28, 2019 | Feb 4, 2019

TASK	PRIORITY	ASSIGNED TO	PROGRESS	START	END
Propulsion		JT, MH, VL			
Heat Flux Calculations	High	JT	100%	11/14/18	2/28/19
Chemical formulation/grain configuration/model in COMSOL	Medium	JT	90%	9/14/18	2/28/19
0-D analysis of combustion, nozzle flow, and thrust estimation	Medium	VL, MH	90%	1/20/19	2/28/19
Analyze COMSOL simulation	Medium	JT	100%	1/20/19	2/28/19
Research System Idea for clustered main motor	Medium	JT	100%	9/5/18	10/5/18
Research and Order Pyrogen and Igniter Wires	High	VL	100%	9/14/18	11/15/18
Order H motor casings and caps	High	JT	100%	9/24/18	10/8/18
Order I motor casings and caps	High	JT	100%	1/15/19	2/2/19
Motor uncertainty/Contact TRA for motor statistics uncertainty	Medium	JT	100%	9/19/18	10/10/18
Create composite thrust curve for other teams	Medium	JT	100%	9/24/18	10/15/18
Research ignition system for clustered motors	Medium	VL	100%	9/24/18	10/8/18
Analyze Ignition Test Results	High	JT, MH	100%	11/30/18	2/28/19
Test Ignition System	High	JT, MH, VL	100%	11/7/18	2/28/19
Construct Ignition system	High	JT	100%	10/25/18	2/28/19
Hand-drawn conceptual drawings of motor mount	High	JT, MH, VL	100%	9/24/18	10/8/18
Physical design and construct motor mount	High	JT, MH, VL	100%	10/7/18	10/28/18
Stage Separation					
CO₂ Separation		SH, NS			
Model of CO2 Systems	Medium	NS	100%	9/10/18	2/20/19
Step-by-step conceptual drawing	High	SH,NS	100%	9/17/18	9/20/18
Research systems that are similar to CO2 Sep & parts similar to Apogee kit	Medium	NS	100%	9/17/18	9/20/18
Purchase CO2 parts	Medium	NS	100%	10/3/18	11/28/18
Construct CO2 System - Machine threaded rod (turn down, hole for grub screw) (Dependent on part arrival	High	SH, NS	100%	10/23/18	1/25/19
CO2 Transient Flow Model	High	SH	100%	9/17/18	2/25/19
CO2 Nose cone Force Test	Medium	SH	100%	9/12/18	10/3/18
Black Powder Backup Calculations	Low	SH	100%	9/17/18	9/21/18

154

Task	Priority	Assigned	%	Start	End
Black Powder Construction	Low	SH, NS	100%	12/3/18	12/14/18
Sizing and mass estimate	Medium	SH, NS	100%	9/24/18	2/20/19
Design firing systems	High	SH, NS	100%	10/22/18	11/8/18
Leak Proofing Magazine	High	SH, NS	100%	10/22/18	10/27/18
CO2 Separation Testing	High	SH, NS	25%	1/27/19	
PLA Material Testing	Medium	SH, NS	50%	2/1/19	
Leak Testing - Leak Testing in water - Long term leak testing	High	SH, NS	100%	10/7/18	10/7/18

Electromagnetic Booster Separation

Task	Priority	Assigned	%	Start	End
Electromagnetic Calculations - Determing Circuit Current, Capacitance, Resistance, Inductance, etc..	High	NLF & VL & JT	100%	9/17/18	12/1/18
Physical and functional layout of electromagnetic system -Design the circuit including all circuit components	High	NLF, VL, SH	100%	11/5/18	12/14/18
Materials comparison for electromagnetic system - Confirm solenoid core, wire AWG, garolite, permanent magnet	Medium	NLF	100%	11/5/18	12/14/18
Sizing and mass estimate - Give Controls and MSAT dimensions and mass of system to help their analysis	High	VL & NLF	100%	11/5/18	2/15/19
Purchasing Parts - Purchase all parts for breadboarding, testing, and construction of the circuit	Low	NLF	100%	11/14/18	12/5/18
Construction of Ground Test Electromagnetic System - Construct the prototype for seperation	Low	NLF, VL	100%	12/1/18	2/25/19
Write Electromagnetic Testing Plan - Prepare for testing system by writing procedures - provide timelines, procudes, lists.	Medium	NLF, VL	100%	11/20/18	1/23/19
Breadboarding - test circuit to assure calculation results. - Make any changes needed to assure successful seperation	Medium	NLF, JT, VL	100%	11/20/18	2/25/19
COMSOL Model of Electromagnetic Coil -Develop CAD model in COMSOL -Analyze results and compare to theoretical	Medium	NLF, JT	100%	1/9/18	2/22/19
Manufacture Steel Rods for Electromagnet Separation Sytem	High	NLF	100%	1/9/18	2/6/19
Electromagnetic Separation Testing - Using constructed system, perform ground testing to create reliable results	High	NLF, VL	100%	11/20/18	2/25/19

Recovery

Central Hub/Axis

Task	Priority	Assigned	%	Start	End
Physical design	High	JF	100%	9/1/18	2/2/19
Work through and research Blade Calculations/ propellar theory	High	CM & JF	100%	9/14/18	2/22/19
Modeling	High	JF	100%	9/14/18	2/20/19
Rocket Descent Rates for Autorotation	High	JF	100%	12/1/18	2/20/19
Rocket descent rates	Medium	CM	100%	9/10/18	11/5/18
Sizing and mass estimate	High	CM & JF	100%	9/19/18	12/5/18
Determine if method for calculation and design of blades is a go or no go	High	CM & JF	100%	11/8/18	1/24/19
Create Flow Chart	High	CM & JF	100%	1/10/19	1/25/19

Parachutes

Task	Priority	Assigned	%	Start	End
Booster Descent rates/ parachute sizing	High	CM	100%	10/10/18	10/20/18
Purchase Parachutes	Medium	CM	100%	10/15/18	10/25/18
Deliver controls team equations of motion	Low	CM	100%	11/9/18	11/19/18
Integrate Parachutes/Flame retardent cloth into rocket	Medium	CM & JF	100%	12/8/18	12/8/18
Drogue parachute calculations/ sizing	Medium	CM	100%	9/10/18	9/20/18

PSR Gantt Chart

Timeline: Feb 11, 2019 | Feb 18, 2019 | Feb 25, 2019 | Mar 4, 2019 | Mar 11, 2019 | Mar 18, 2019 | Mar 25, 2019 | Apr 1, 2019

TASK	PRIORITY	ASSIGNED TO	PROGRESS	START	END
Propulsion		JT, MH, VL			
Heat Flux Calculations	High	JT	100%	11/14/18	2/28/19
Chemical formulation/grain configuration/model in COMSOL	Medium	JT	90%	9/14/18	2/28/19
0-D analysis of combustion, nozzle flow, and thrust estimation	Medium	VL, MH	90%	1/20/19	2/28/19
Analyze COMSOL simulation	Medium	JT	100%	1/20/19	2/28/19
Research System Idea for clustered main motor	Medium	JT	100%	9/5/18	10/5/18
Research and Order Pyrogen and Igniter Wires	High	VL	100%	9/14/18	11/15/18
Order H motor casings and caps	High	JT	100%	9/24/18	10/8/18
Order I motor casings and caps	High	JT	100%	1/15/19	2/2/19
Motor uncertainty/Contact TRA for motor statistics uncertainty	Medium	JT	100%	9/19/18	10/10/18
Create composite thrust curve for other teams	Medium	JT	100%	9/24/18	10/15/18
Research ignition system for clustered motors	Medium	VL	100%	9/24/18	10/8/18
Analyze Ignition Test Results	High	JT, MH	100%	11/30/18	2/28/19
Test Ignition System	High	JT, MH, VL	100%	11/7/18	2/28/19
Construct Ignition system	High	JT	100%	10/25/18	2/28/19
Hand-drawn conceptual drawings of motor mount	High	JT, MH, VL	100%	9/24/18	10/8/18
Physical design and construct motor mount	High	JT, MH, VL	100%	10/7/18	10/28/18
Stage Separation					
CO₂ Separation		SH, NS			
Model of CO2 Systems	Medium	NS	100%	9/10/18	2/20/19
Step-by-step conceptual drawing	High	SH,NS	100%	9/17/18	9/20/18
Research systems that are similar to CO2 Sep & parts similar to Apogee kit	Medium	NS	100%	9/17/18	9/20/18
Purchase CO2 parts	Medium	NS	100%	10/3/18	11/28/18
Construct CO2 System - Machine threaded rod (turn down, hole for grub screw) (Dependent on part arrival	High	SH, NS	100%	10/23/18	1/25/19
CO2 Transient Flow Model	High	SH	100%	9/17/18	2/25/19
CO2 Nose cone Force Test	Medium	SH	100%	9/12/18	10/3/18
Black Powder Backup Calculations	Low	SH	100%	9/17/18	9/21/18

156

Task	Priority	Owner	%	Start	End
Black Powder Construction	Low	SH, NS	100%	12/3/18	12/14/18
Sizing and mass estimate	Medium	SH, NS	100%	9/24/18	2/20/19
Design firing systems	High	SH, NS	100%	10/22/18	11/8/18
Leak Proofing Magazine	High	SH, NS	100%	10/22/18	10/27/18
CO2 Separation Testing	High	SH, NS	25%	1/27/19	
PLA Material Testing	Medium	SH, NS	50%	2/11/19	
Leak Testing - Leak Testing in water - Long term leak testing	High	SH, NS	100%	10/7/18	10/7/18

Electromagnetic Booster Separation

Task	Priority	Owner	%	Start	End
Electromagnetic Calculations - Determing Circuit Current, Capacitance, Resistance, Inductance, etc..	High	NLF & VL & JT	100%	9/17/18	12/1/18
Physical and functional layout of electromagnetic system -Design the circuit including all circuit components	High	NLF, VL, SH	100%	11/5/18	12/14/18
Materials comparison for electromagnetic system - Confirm solenoid core, wire AWG, garolite, permanent magnet	Medium	NLF	100%	11/5/18	12/14/18
Sizing and mass estimate - Give Controls and MSAT dimensions and mass of system to help their analysis	High	VL & NLF	100%	11/5/18	2/15/19
Purchasing Parts - Purchase all parts for breadboarding, testing, and construction of the circuit	Low	NLF	100%	11/14/18	12/5/18
Construction of Ground Test Electromagnetic System - Construct the prototype for seperation	Low	NLF, VL	100%	12/1/18	2/25/19
Write Electromagnetic Testing Plan - Prepare for testing system by writing procedures - provide timelines, procudes, lists.	Medium	NLF, VL	100%	11/20/18	1/23/19
Breadboarding - test circuit to assure calculation results. - Make any changes needed to assure successful seperation	Medium	NLF, JT, VL	100%	11/20/18	2/25/19
COMSOL Model of Electromagnetic Coil -Develop CAD model in COMSOL -Analyze results and compare to theoretical	Medium	NLF, JT	100%	1/9/18	2/22/19
Manufacture Steel Rods for Electromagnet Separation Sytem	High	NLF	100%	1/9/18	2/6/19
Electromagnetic Separation Testing - Using constructed system, perform ground testing to create reliable results	High	NLF, VL	100%	11/20/18	2/25/19

Recovery

Central Hub/Axis

Task	Priority	Owner	%	Start	End
Physical design	High	JF	100%	9/1/18	2/2/19
Work through and research Blade Calculations/ propellar theory	High	CM & JF	100%	9/14/18	2/22/19
Modeling	High	JF	100%	9/14/18	2/20/19
Rocket Descent Rates for Autorotation	High	JF	100%	12/1/18	2/20/19
Rocket descent rates	Medium	CM	100%	9/10/18	11/5/18
Sizing and mass estimate	High	CM & JF	100%	9/19/18	12/5/18
Determine if method for calculation and design of blades is a go or no go	High	CM & JF	100%	11/8/18	1/24/19
Create Flow Chart	High	CM & JF	100%	1/10/19	1/25/19

Parachutes

Task	Priority	Owner	%	Start	End
Booster Descent rates/ parachute sizing	High	CM	100%	10/10/18	10/20/18
Purchase Parachutes	Medium	CM	100%	10/15/18	10/25/18
Deliver controls team equations of motion	Low	CM	100%	11/9/18	11/19/18
Integrate Parachutes/Flame retardant cloth into rocket	Medium	CM & JF	100%	12/8/18	12/8/18
Drogue parachute calculations/ sizing	Medium	CM	100%	9/10/18	9/20/18

157

Appendix D: System of Equations for 0D Combustion Modeling (MATLAB®)

```matlab
clear all; close all; clc;
%% Defined Variables & Constants
g = 9.81; %gravitational constant (m/s^2)
C_p = [1553.4 1554 1554.4 1554.7 1554.9 1555.1 1555.3 1555.4 1555.5];%specific heat↵
@ constant pressure (J/kg-mol-K)
C_v = [1251.6 1252.4 1253 1253.4 1253.8 1254.1 1254.4 1254.6 1254.8];
k = C_p./C_v;
L_motor = 0.153; %m
A_s = 0.0175; %average surface area of propellant grain (m^2)
rho = [9.76899 14.6293 19.4846 24.3367 29.1863 34.0339 38.8801 43.7249 48.5687];%↵
density of burned gas (kg/m^3)
P_1 = [1000 1500 2000 2500 3000 3500 4000 4500 5000].*6894.757;%chamber pressure↵
(Pa)
A_2 = 0.000246; %cross sectional area of the nozzle exit
P_3 = 101325; %atmospheric pressure (Pa)
T_1 = [2337.92 2343.92 2348.03 2351.14 2353.63 2355.72 2357.5 2359.07 2360.46];%↵
chamber temperature/heated gas temperature (K)
a = 5.538*10^-9; %burn rate coefficient
R_bar = 8314.3; %universal gas constant (J/kg mol-K)
n = 0.8943; %pressure exponent
b = -0.0005789; %%% Burn rate vertical shift coefficient
%% Mixed Gas
%% Mass Flow Rate
%for i=1:...;
%MM_eff_ind= n_j(:,n).*MM(:,n)./(n_j(:,n));
%MM_eff = symsum(MM_eff_ind, 1, i);
%R_eff = (R_bar)/(MM_eff);
%C_p_ind = n_j(:,i).*C_p(:,i)/(n_j(:,i));
%C_p_eff = symsum(C_p_ind, 1, i);
%k=(C_p_eff)/(C_p_eff-R_bar);
%end

MM_eff = [27.541 27.566 27.5845 27.5994 27.6119 27.6228 27.6325 27.6412 27.6492];%↵
kg/kg mol
R_eff =(R_bar)./(MM_eff);
%% Burn Rate
r = a.*P_1.^n + b ; %Burn Rate as function of chamber pressure
%% Minimum Throat Area
m_dot=rho.*r.*A_s; %Average steady state mass flow rate
%A_t = (sqrt(R_eff.*T_1).*m_dot./P_1).*(k.*(2./(k+1)).^((k+1)./(k-1)).^(-1/2));%%↵
Minimum throat area
A_t = pi/4*(5*10^(-3))^2;
Ae_over_At = A_2./A_t;
P2_over_P1 = [3.599, 5.88, 8.274, 10.774, 13.347, 16.015, 18.622, 21.421, 24.225]↵
*10^(-5);
P_2 = P_1.*P2_over_P1; %pressure at nozzle exit (Pa) %%%Need A_2 to get P_2 with↵
isentropic calculator

%% Thrust and Impulse
```

```matlab
C_F = sqrt((2.*k.^2./(k-1)).*(2./(k+1)).^((k+1)./(k-1)).*(1-(P_2./P_1).^((k-1)./k)))↵
((P_2-P_3)./P_1).*(A_2./A_t);
T = C_F.*A_t.*P_1;
I_sp=(C_F.*A_t.*P_1)./(m_dot.*g);
%% Plots

figure;
plot(P_1, r);
title('Burn Rate vs Chamber Pressure'); xlabel('Chamber Pressure (Pa)');
ylabel('Burn Rate (m/s)');

figure;
plot(P_1, A_t);
title('Minimum Throat Area vs Chamber Pressure'); xlabel('Chamber Pressure (Pa)');
ylabel('Minimum Throat Area (m^2)');

figure;
plot(P_1, T);
title('Thrust vs Chamber Pressure'); xlabel('Chamber Pressure (Pa)');
ylabel('Thrust (N)');

figure;
plot(P_1, I_sp);
title('Specific Impulse vs Chamber Pressure'); xlabel('Chamber Pressure (Pa)');
ylabel('Specific Impulse (s)');
```

Appendix E: Thermodynamics Computational Code for 0D Combustion Model (Cantera)

nh4clo4.py

```python
1  import cantera as ct
2  import numpy as np
3
4  soln=ct.Solution('input.cti')
5  soln.TPX = 500, 10e5, 'NH4CLO4:1.0'
6  soln.equilibrate('HP')
7  soln()
```

Appendix F: CO₂ Saturation Properties [50]

Temperature [K]	Pressure [MPa]	C_v [J/mol K]	C_p [J/mol K]
298.04	6.4179	47.012	280.72
297.64	6.359	46.685	267.64
297.23	6.3	46.388	256.06
296.83	6.2409	46.118	245.72
296.42	6.182	45.871	236.44
296	6.123	45.645	228.06
295.58	6.064	45.437	220.45
295.16	6.0049	45.245	213.5
294.74	5.946	45.067	207.13
294.31	5.8869	44.902	201.27
293.88	5.8279	44.748	195.86
293.45	5.7689	44.604	190.84
293.01	5.71	44.469	186.17
292.57	5.651	44.342	181.81
292.12	5.592	44.222	177.73
291.67	5.5329	44.108	173.91
291.22	5.4739	43.999	170.31
290.76	5.415	43.895	166.93
290.3	5.356	43.796	163.74
289.84	5.2969	43.701	160.72
289.37	5.2379	43.609	157.86
288.89	5.1789	43.52	155.16
288.42	5.1199	43.434	152.59
287.94	5.0609	43.351	150.15
287.45	5.0019	43.27	147.83
286.96	4.9429	43.192	145.62
286.47	4.884	43.115	143.51
285.97	4.8249	43.039	141.49
285.46	4.766	42.966	139.57
284.95	4.707	42.893	137.73
284.44	4.6479	42.822	135.97
283.92	4.589	42.752	134.28
283.4	4.5299	42.683	132.66
282.87	4.471	42.615	131.11
282.34	4.4119	42.548	129.61
281.8	4.3529	42.482	128.18
281.25	4.2939	42.416	126.79
280.7	4.235	42.351	125.46

280.14	4.1759	42.286	124.17
279.58	4.1169	42.222	122.93
279.01	4.058	42.159	121.73
278.44	3.999	42.096	120.57
277.86	3.94	42.034	119.45
277.27	3.881	41.973	118.37
276.68	3.8219	41.912	117.31
276.08	3.763	41.853	116.3
275.47	3.704	41.794	115.31
274.85	3.6449	41.736	114.35
274.23	3.5859	41.68	113.42
273.6	3.5269	41.624	112.51
272.96	3.4679	41.571	111.63
272.32	3.4089	41.518	110.78
271.66	3.35	41.468	109.95
271	3.2909	41.419	109.14
270.33	3.2319	41.373	108.35
269.65	3.173	41.329	107.58
268.96	3.1139	41.287	106.84
268.26	3.0549	41.248	106.11
267.55	2.996	41.211	105.4
266.83	2.937	41.178	104.7
266.1	2.878	41.148	104.03
265.36	2.819	41.12	103.36
264.6	2.7599	41.097	102.72
263.84	2.701	41.076	102.09
263.06	2.6419	41.06	101.47
262.27	2.583	41.046	100.87
261.47	2.5239	41.037	100.28
260.65	2.4649	41.031	99.701
259.82	2.4059	41.029	99.136
258.97	2.3469	41.03	98.582
258.11	2.2879	41.035	98.04
257.23	2.229	41.044	97.509
256.33	2.17	41.056	96.988
255.42	2.111	41.071	96.478
254.49	2.0519	41.09	95.977
253.53	1.993	41.112	95.487
252.56	1.9339	41.137	95.005
251.56	1.8749	41.164	94.533
250.54	1.8159	41.195	94.07

249.5	1.7569	41.229	93.616
248.43	1.6979	41.265	93.17
247.33	1.6389	41.304	92.733
246.21	1.58	41.346	92.304
245.05	1.5209	41.391	91.883
243.86	1.4619	41.439	91.471
242.63	1.403	41.49	91.066
241.36	1.344	41.544	90.669
240.06	1.2849	41.602	90.279
238.7	1.2259	41.664	89.898
237.3	1.1669	41.73	89.524
235.85	1.108	41.801	89.157
234.33	1.0489	41.876	88.798
232.75	0.98995	41.957	88.447
231.11	0.93095	42.044	88.103
229.38	0.87195	42.137	87.768
227.56	0.81295	42.238	87.441
225.64	0.75395	42.347	87.123
223.6	0.69495	42.465	86.815
221.43	0.63595	42.595	86.518
219.11	0.57695	42.737	86.232
216.59	0.51795	42.895	85.96

Appendix G: CO₂ Transient Flow Calculations MATLAB® Script

```matlab
close all; clear variables; clc;

%%%%%%%%%%%%%%%%%%%%%%%%%%%%%%%%%%%%%%%%%%%%%%%%%%%%%%%%%%%%%%%%%%%
% Common Variables

% Time Dependent
% gamma_co2   Specific weight CO2 [N/m^3]
% m_co2       Mass CO2 [g]
% rho_c       Density CO2 [kg/m^3]
% T_c         Temperature CO2 canister [K]
% Z           Compressibility Factor [unitless]

% Constant
% A_e         CO2 canister exit area [m^2]
% g           Acceleration due to gravity [m/s^2]
% R_co2       Gas constant CO2 [J/(kg*K)]
% rho_c0      Density CO2 initial [kg/m^3]
% T_c0        Temperature CO2 canister initial [K]
% V_c         Volume CO2 canister [m^3]
%%%%%%%%%%%%%%%%%%%%%%%%%%%%%%%%%%%%%%%%%%%%%%%%%%%%%%%%%%%%%%%%%%%
% Load CO2 Properties from NIST needed to calculate CO2 properties and
% compressibility factor, Z
load Cp_CO2.mat
load Cv_CO2.mat
load T_data.mat
load P_data.mat

% Constants / Initial Conditions
% Canister/ CO2
g = 9.81;                    % m/s^2
A_e = 1e-6;                  % m^2
T_c0 = 298;                  % KCp
V_c = 1.4e-5;               % m^3
P_atm = 101325;

m_CO2_0 = 12e-3;            % kg
MM_CO2 = 44.0095e-3;       % kg/mol
n_CO2 = m_CO2_0*(1/MM_CO2); % mol

% Calculate specific heat ratio using NIST properties
gamma_CO2 = Cp_CO2./Cv_CO2;
```

```matlab
% Convert Cp and Cv values into [J/kg K]
Cp_CO2_kg = Cp_CO2*(1/MM_CO2);
Cv_CO2_kg = Cv_CO2*(1/MM_CO2);

% Calculate gas constant using NIST data [J/kg K]
R_CO2 = minus(Cp_CO2_kg,Cv_CO2_kg);


P_c0 = 6.423e6;              % Pa
P_c0_bar = P_c0*1e-5;       % bar
P_data_bar = P_data*10;     % Convert NIST pressure data into bars


rho_c0 = m_CO2_0/V_c;       % kg/m^3

% Compressibility factor script courtesy of Chad Greene
Z = compressibility('carbon dioxide',T_data,P_data_bar);
% Set matrix of ones for case where Z = 1 for ODE
Z_1a = 1.*ones(length(1),101);
Z_1 = transpose(Z_1a);

% Critical Pressure Ratio Reached (update based on P_ratio and
% P_ratio_nocomp), x is where the ratio reaches 1.83
x=24;
x_nocomp=22;

% Pressure from ext. air on nose cone
P_nose = 140967;

% Time step
dt = 0.003;
dend = .3;
tspan = 0:dt:dend;

% Index
i = 1;
j = 1;
```

ODE Solver Z is transient

```
for time = tspan %Cycles through each deploy time
    %%Stage 1 Flow: Choked, Phase Change

    %Intial Conditions
    y0= [m_CO2_0];

    %Solves the system of equations during the time span
    [t1,y1] = ode45(@(t,y)
Canister_flow(t,y,A_e,T_c0,V_c,rho_c0,R_CO2(i),...
        gamma_CO2(i),Z(i)),tspan,y0);
i = i+1;
end
```

ODE Solver Z = 1

```
for time = tspan %Cycles through each deploy time
    %%Stage 1 Flow: Choked, Phase Change

    %Intial Conditions
    y0= [m_CO2_0];

    %Solves the system of equations during the time span
    [t2,y2] = ode45(@(t,y)
Canister_flow_nocomp(t,y,A_e,T_c0,V_c,rho_c0,...
        R_CO2(j),gamma_CO2(j),Z_1(j)),tspan,y0);
j = j+1;
end
```

Cartridge Properties

Isentropic Relations, Z is transient (Z accounted for in ode solver)

```
rho_c = y1(:,1)/V_c;
T_c = T_c0*((rho_c/rho_c0).^(gamma_CO2-1));
P_c = (((rho_c/rho_c0).^(gamma_CO2))*P_c0);
P_c_actual = P_c(1:x);

% Isentropic Relations, Z = 1 (no compressibility factor)
rho_c_nocomp = y2(:,1)/V_c;
T_c_nocomp = T_c0*((rho_c_nocomp/rho_c0).^(gamma_CO2-1));
P_c_nocomp = (((rho_c_nocomp/rho_c0).^(gamma_CO2))*P_c0);
P_c_nocomp_actual = P_c_nocomp(1:x_nocomp);
```

Tube Properties

Tube

```
gamma_air = 1.40;
R_air = 287.05;                     % J/(kgK)
V_t = 0.00494217463;                % m^3
T_t0 = 298;                         % K
rho_t0 = 1.184;                     % kg/m^3
m_t0 = rho_t0*V_t;                  % kg
P_t0 = (m_t0*R_CO2*T_t0)/V_t;       % Pa
m_air = m_t0;                       % kg
MM_air = 28.97e-3;                  % kg/mol
n_air = m_air*(1/MM_air);           % mol


% Average Tube Mixture Props
Cp_CO2_tube = 37.35/MM_CO2;         % J/kgK
Cp_air = 29.14/MM_air;              % J/(kg*K)
m_total = m_CO2_0/2 + m_air;        % kg
n_total = n_CO2/2 + n_air;          % mol
R = 8.314;                          % J/mol*K


% Molar Mass of Mixture [kg/mol]
MM_mix = ((n_CO2/2)*MM_CO2 + (n_air)*MM_air)/(n_total);
% Gas contant of mixture [J/kgK]
R_mix = R/MM_mix;
% Specific heat, cosntant pressure of mixture [J/molK]


% Specific heat ratio of mixture
gamma_mix = Cp_mix/(Cp_mix-R);


% Isentropic Relations, Z is transient
mdot_t = (m_t0+m_CO2_0) - y1(:,1);
rho_t = mdot_t(:,1)/V_t;
T_t = T_t0*((rho_t/rho_t0).^(gamma_mix-1));
P_t = R_mix*rho_t.*T_t;
P_t_actual = P_t(1:x);
P_t_psi = P_t*0.000145038;


% Isentropic Relations, Z = 1
mdot_t_nocomp = (m_t0+m_CO2_0) - y2(:,1);
rho_t_nocomp = mdot_t_nocomp(:,1)/V_t;
T_t_nocomp = T_t0*((rho_t_nocomp/rho_t0).^(gamma_mix-1));
P_t_nocomp = R_mix*rho_t_nocomp.*T_t_nocomp;
P_t_nocomp_actual = P_t_nocomp(1:x_nocomp);
P_t_psi = P_t_nocomp*0.000145038;


% Pressure Ratio (cartridge flow is choked when P_c/P_t > 1.83)
P_ratio = P_c./P_t;
P_c_crit = 1.002965100983579e+05*1.83;
P_ratio_nocomp = P_c_nocomp./P_t_nocomp;
```

Unchoked flow Estimate (Perfect Gas Law w/ isothermal assumption)

variable b indicates point at which Mach No < 0.3 and flow becomes incompressible. Using gamma_mix and the ratio of est. pressure to initial pressure on the Virginia Tech flow calculator, a pressure ratio of approx. 0.955 results in a Mach number of 0.3 If parameters are changed, run script and update value of b based on results of pressure ratio

```matlab
b = 65;

% Isothermal temp. pulled from the end of the choked flow regime
T_isothermal = T_t(x);

% Range of CO2 - air mixture amounts starting from the end of the
 choked
% flow regime to the end of the unchoked compressible regime (update
% interval of mdot_t to match with number of elements in tspan(x:b)

n_mix_1 = mdot_t(x):.000085:mdot_t(b);

% For loop to determined the estimated pressures in the unchoked
% compressible regime with changing gas amounts
matrix = [];
for y = n_mix_1

P_t_est = (y *R_mix*T_isothermal)/V_t;

matrix = [matrix; P_t_est];
end

% Pressure ratio of estimated pressure to initial pressure (need to
 change
% variable b based on this result)
P_t_est2P_t0 = P_t_est./P_t0;

% Pressure difference between ext. air on nose cone and in tube [Pa]
delta_P = P_t(x)-P_nose;
delta_P_psi = delta_P*0.000145038;
delta_P_unchok = P_t_est(end)-P_nose;
delta_P_unchok_psi = delta_P_unchok*0.000145038;

q = tspan(x:b);
```

```matlab
% Plot Pressure and Mass Changes in the Cartridge and Tube over time
figure(1)
title('Pressure and Mass Change in CO2 Cartridge')
subplot(211);plot(tspan(1:x),P_c(1:x),tspan(1:x),P_c_nocomp(1:x),'--');
ylabel('Pressure [Pa]');legend({'Z = transient','Z
 =1'},'Location','best');
subplot(212);plot(tspan(1:x),y1(1:x),tspan(1:x_nocomp),y2(1:x_nocomp),'--');
xlabel('Time [s]'); ylabel('Mass in Cartridge [kg]');
legend({'Z = transient','Z =1'},'Location','best');

figure(2)
title('Pressure in Rocket Tube vs Time')
subplot(211);plot(tspan(1:x),P_t(1:x),...
    tspan(1:x_nocomp),P_t_nocomp(1:x_nocomp),'--');...
    ylabel('Pressure [Pa]');...
    legend({'Z = transient','Z =1'},'Location','best');
subplot(212);plot(tspan(1:x),mdot_t(1:x),...
    tspan(1:x_nocomp),mdot_t_nocomp(1:x_nocomp),'--');...
    xlabel('Time [s]'); ylabel('Mass in Tube [kg]');...
    legend({'Z = transient','Z =1'},'Location','best');

% Plot change of pressure in tube with unchoked, compressible estimate
figure(3)
title('Pressure Change in Rocket Tube with Unchoked,'...
    'Compressible Regime Estimate');
plot(tspan(1:x),P_t(1:x),tspan(x:b),matrix,'--'); ylabel('Pressure
 [Pa]');...

   legend({'choked','unchoked'},'Location','best'); xlabel('Time
[s]');
```

Published with MATLAB® R2018b

ODE Function

```matlab
function ydot =
 Canister_flow(t,y,A_e,T_c0,V_c,rho_c0,R_CO2,gamma_CO2,Z)

%%%%%%%%%%%%%%%%%%%%%%%%%%%%%%%%%%%%%%%%%%%%%%%%%%%%%%%%%%%%

% r1 = dm_co2_dt          [kg/s]


ydot(1) = ((A_e*(Z*R_CO2*(y/V_c)*T_c0*(y/
(rho_c0*V_c))^(gamma_CO2-1)))/(sqrt(T_c0*(y/
(rho_c0*V_c))^(gamma_CO2-1))))*sqrt(gamma_CO2/
R_CO2)*((gamma_CO2+1)/2)*((1-gamma_CO2)/(2*(gamma_CO2-1)));

end
```

Appendix H: Electromagnetic Prototype Testing

Proper Lab Safety Procedures

There must be at least two people during electromagnet activation due to potentially dangerous amount of current and voltage.

Document any experiments on the Experiment Journal that can be found in the Google Drive.

Magnet Force Testing

Purpose:

By calculating the force measured, we can predict the force (against a theoretical flat plate) and determine the force coefficient. (WARRIORS found it to be 0.46)

Materials:

- Neodymium Boron Magnet

- Fish scale

- Steel cylinder of similar size

Procedure:

- Attach magnet to fish scale

- Connect metal to magnet

- Pull metal until separation, measure quantity

Electromagnet Activation

Purpose:

Test and analyze activation of one electromagnet. Successful separation requires timely and sufficiently powerful activation from the electromagnet. Test the range of capacitors and measure the magnetic field given from each. Test out fabrication methods for optimum efficiency.

Materials:

- Capacitor

- Resistors

- Magnet Wire

- Permanent magnet

- Current Oscillator

- Steel core

- Batteries

Procedure:

- Construct functioning circuit

    - When capacitor discharges, electromagnet exerts magnetic field

- Measure strength of different capacitors

    - Place permanent magnet above

- Choose the capacitor that exerts enough force

- Fabricate electromagnet for practice

Purpose:

Test an analyze separation of all electromagnets **simultaneously**.
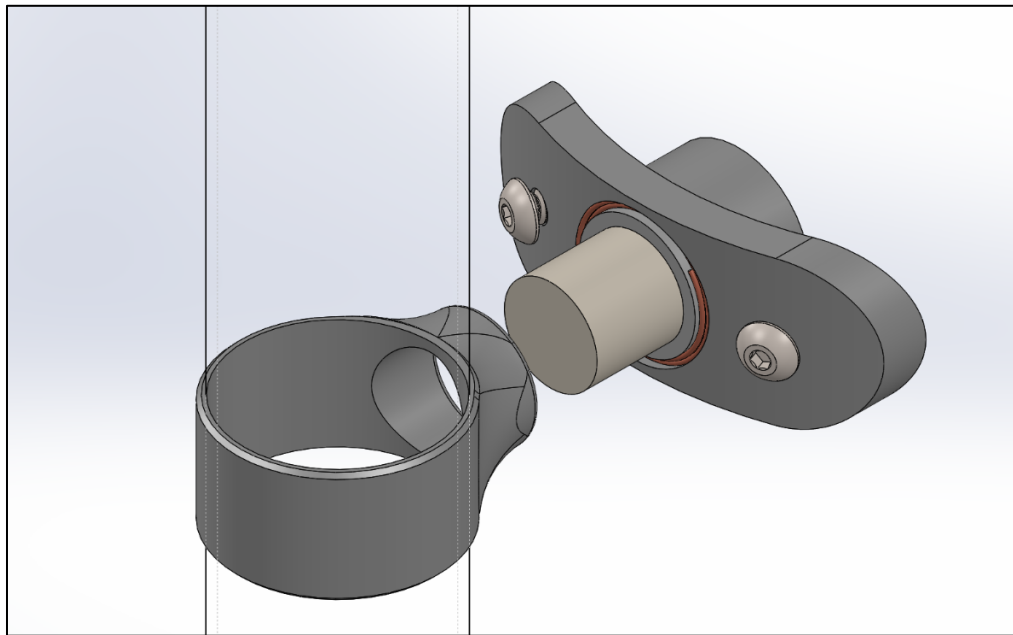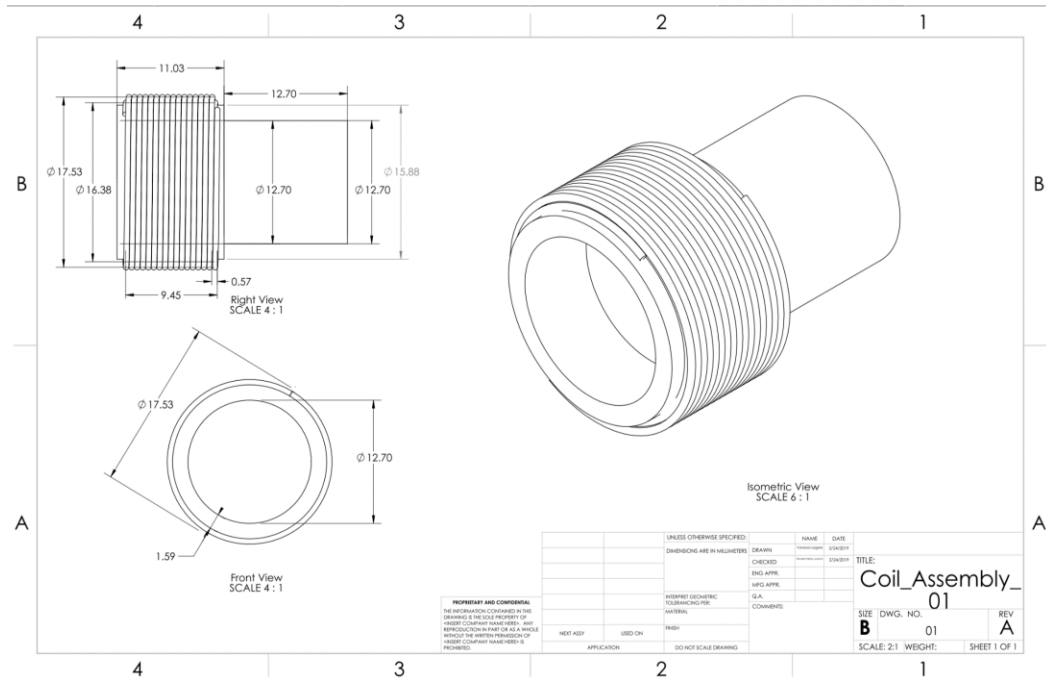
Materials:

- Capacitor

- Resistors

- Magnet Wire

- Permanent magnet

- Current Oscillator

- Steel core

- Batteries

Procedure:

After all of this testing we will begin implementation of the separation system on the main rocket.

Appendix I: CAD Model of Electromagnet Separation System

Appendix J: Autorotation Code

```matlab
clc; clear; close all;

%Given Properties
rho = 1.2;        %Kg/m^3 %air density at altitude (estimate)
W = 4.5;          %Weight of Rocket (kg current estimate)
Max_F = W*9.81;   %Force needed for zero accel (N)
c = .0838;        %Chord length (m)
R = 0.58;         %blade span (m or 22 in) (from what MSAT gave us)
r = 0.1:.01:0.58; %distance along span (per cm)
%because of the trig functions the equations go to infinity close to 0
mu = r./R;
A_D = pi*R^2;     %Area of disc
a_d = pi.*r.^2;   %differential area
dS = c*.01;       %differential area (per cm)
b = 3;            %number of blades
v_w = -6;         %Velocity of wind at equilibrium, descent velocity (m/s)

%Basic Properties
sigma = (b*c)/(pi*R); %Rotor solidity
Dl = W/A_D;       %Disk loading ratio
```

Wind Turbine Method to find desired Cl

```matlab
%First Cl estimate based on usual Cl for
Cl_0 = .5;

%Tip speed for equilibrium guess for helicopters
omega_Ri = sqrt((6*W)/(sigma*Cl_0*rho*A_D));

%Decide on OmegaR (faster is more stable and requires smaller Cls)
omega_R = 35;     %m/s
omega = omega_R/R;     %rad/s
omegadeg = omega*57.2958; %deg/s
rpm = omegadeg*60/360;
omega_r = omega.*r; %rad/s along blade length

%Indiced Velocity same as hover (possible calculations from Filiponne)
```

```matlab
vi = sqrt(W/(2*rho*A_D));
Pi = vi * W;
C_T = Max_F/(rho*A_D*(omega_R)^2);    %Coefficient of Torque
lamdas = (v_w+vi)/omega_R;

CD_avg = (-(v_w)/omega_R - sqrt(C_T/2))*C_T*8/sigma;
```

Using Wind turbine calculations (derived from Wind Turbine Handbook)

```matlab
%Equation in Wind Energy Handbook
lamda = omega_R/(-v_w);
%Angles and Wind
Vrel_r = sqrt(((omega.*r).^2) + v_w^2); %Relative wind velocity
phi = -asin(v_w./(omega_r));        %Relative wind angle
phi_deg = rad2deg(phi);

%General twist equation for wind turbine blades (possible guideline)
    %Can input custom twist configuration
inflow = atan((2/3)./(lamda.*mu.*(1+2./(3.*lamda.^2.*mu.^2))));
twist = inflow - phi;
twistdeg = -rad2deg(twist);
alpha = phi + twist;
alpha_deg = rad2deg(alpha);

figure
plot(mu,twistdeg, mu, alpha_deg);
xlabel('r/R & Alpha');
ylabel('Twist & AOA (degrees)');
title('Optimal Blade Twist');
legend('Twist', 'AOA');
```

Reynolds Numbers

```matlab
Re = (rho.*Vrel_r.*c)/(1.8*10^(-5));

figure
format long;
plot(mu,Re);
xlabel('r/R');
ylabel('Reynolds Numbers');
title('Reynolds Numbers at Speed');
figure
plot(mu,phi_deg);
xlabel('r/R');
ylabel('phi (degrees)');
title('Angle of Relative Wind Along the Span');
```

174

Calculate desired Cl & Cd along r

```matlab
%using real to eliminate immaginary component created in angle calcs
Cl = real((8/9)*1./(((b*c.*lamda)./(2*pi)).*sqrt((1-1/3)^2+lamda.^2.*mu.^2.*(1+2./(9.*lamda.^
2.*mu.^2)).^2)));
CD_r = real (Cl.*tan(alpha));

%if optimizing chord (?? still unsure how this helps)
c_opt = R*8./(9*lamda*0.8).*(2-(lamda.*mu)./(lamda*.8))*2*pi./(Cl.*lamda*b);

figure
plot(mu,Cl,mu,CD_r);
```

```matlab
xlabel('r/R');
ylabel('Coefficients');
title('Coefficient of Lift and Drag');
legend('Cl', 'Cd');

% Checking Final force created by each blade section
ftot_r = (.5*rho.*Vrel_r.^2 .* Cl).*cos(phi).*dS + (.5*rho.*Vrel_r.^2 .* CD_r).*sin(phi).*dS;
```

Does this equal the mass?

```matlab
Ftot_actual = 3*real(sum(ftot_r));
Ftot_new = Ftot_actual/9.81;

% Table to make blade
Boom = [mu; Cl; CD_r];
```

Calculate Drogue Force

```matlab
%Cd_drogue = (2*9.81*W)/(rho*S_drogue*v_w^2);
Cd_drogue = 1.2;
r_d = .22; %m
A_drogue = 4*Pi*r_d^2;
drag_chute = .5*Cd_drogue*rho*A_drogue*(v_w^2);
F_g = W*9.81;    %Force of gravity
V_i = 9.81*3; %Initial velocity of the nosecone when the parachute opens.
t_steps = 0:0.01:2;

for i=1:201

    dt = .01;
    F_d(i) = .5*rho*Cd_drogue*A_drogue*V_i(i).^2;
    a(i) = (F_d(i)-F_g)./W;
    V_f(i) = V_i(i)-a(i)*dt;
    V_i(i+1)=V_f(i);

end

figure
plot(t_steps,F_d)
title('Force on Nosecone Bulkhead vs Time');
xlabel('Time')
ylabel('Overall Force')
```

Calculate Starting Point forces

```matlab
vguess = -1;      %m/s
omegaguess = 1; %rad/s


Vrel_initial = sqrt(((omegaguess.*r).^2) + vguess^2); %Relative wind velocity
Re_initial = (rho.*abs(vguess).*c)/(1.8*10^(-5));
phi1 = -1.*real(asin(vguess./(omegaguess.*r)));
phi1_deg = round(rad2deg(phi1));

% Using Calculated Twist above find AOA
alpha1 = phi1 + twist;
alpha1_deg = real(round(rad2deg(alpha1)));

% Input Airfoil Data
filename = 'NACA 6420_T1_Re0.200_M0.00_N9.0.xlsx';
sheet = 1;
xlRange = 'A4:C75';
testdata = xlsread(filename,sheet,xlRange);
Adat = (testdata(:,1));
Cldat = testdata(:,2);
Cddat = testdata(:,3);
[~, index] = min(abs(alpha1_deg-Adat));
Cla = Cldat(index)';
Cda = Cddat(index)';
```

Set up rotation

```matlab
%Based on moments, Autorotative index, and rocket acceleration
density_cf = 1300;       %Density of kg/m^3
volume_blade = c*R*.005; %m^3
M = density_cf*volume_blade; %kg/blade
k = 1;                   %kg/m air resistance
t_to_splat = sqrt(1200/(k*9.81));
t_rec = 10;              %Est req recovery time (s)

%Torque Produced
Ti = ((.5*rho.*Vrel_initial.^2 .* Cla).*sin(alpha1).*dS - (.5*rho.*Vrel_initial.^2 .* Cda).*c
os(alpha1).*dS).*r;
Ti_tot = 3*real(sum(Ti)); %Nm
I = 3*(1/3)*M*R^2;        %Moment of Inertia assuming blade as a rod (kg*m^2/s)
ang_accel = Ti_tot/I; %Instantaneous Velocity (rad/s^2)
omega_new = omegaguess + ang_accel*.01; %(rad/s)
```

177

Set up falling

```
%Force up
Fi = (.5*rho.*Vrel_initial.^2 .* Cla).*cos(alpha1).*dS + (.5*rho.*Vrel_initial.^2 .* Cda).*si
n(alpha1).*dS;
Fi_tot = 3*real(sum(Fi));
F_tot = Fi_tot - 9.81*W;


accel = F_tot/W;
v_new = vguess + accel*.01;
%height to fall
h0 = 0;
t = .001; %time step
n = 1;
height = h0 + v_new*t + .5*accel*(t^2);
```

Time/Altitude/Acceleration to reach zero

```
height_of_deploy = 457; %m or 1500ft or height of recovery deployment

tfs = [];
heights = [];
v_news = [];
accels = [];
ang_accels = [];
omega_news = [];

 while height > -height_of_deploy
    Vrel_ri = sqrt(((omega_new.*r).^2) + v_new^2); %Relative wind velocity
    phi1 = -1.*real(asin(v_new./(omega_new.*r)));
    phi1_deg = round(rad2deg(phi1));

    % Using Calculated Twist above find AOA
    alpha1 = phi1 + twist;
    alpha1_deg = real(round(rad2deg(alpha1)));

    % Call data
```

```matlab
    [~, index] = min(abs(alpha1_deg-Adat));
    Cla = Cldat(index)';
    Cda = Cddat(index)';

    %Torque Produced
    Ti = ((.5*rho.*Vrel_ri.^2 .* Cla).*sin(alpha1).*dS - (.5*rho.*Vrel_ri.^2 .* Cda).*cos(alp
ha1).*dS).*r;
    Ti_tot = real(sum(Ti)); %Nm
    ang_accel = Ti_tot/I; %Instantaneous Velocity (rad/s^2)
    omega_new = omega_new + ang_accel*t; %(rad/s)

    %Force up
    Fi = (.5*rho.*Vrel_ri.^2 .* Cla).*cos(alpha1).*dS + (.5*rho.*Vrel_ri.^2 .* Cda).*sin(alph
a1).*dS;
    Fi_tot = 3*real(sum(Fi));
    %From Drogue
    Cd_drogue = 1;
    r_d = .22; %m
    A_drogue = 4*Pi*r_d^2;
    drag_chute = .5*Cd_drogue*rho*A_drogue*(v_new^2); %Drag produced by par
    %Total % add or remove chute drag
    F_tot = Fi_tot - 9.81*W;

    accel = F_tot/W;
    v_new = v_new + accel*t;
    %height to fall
    height = height + v_new*t + .5*accel*(t^2);
    n=n+1;
    tf = t*n;
```

```matlab
    tfs = [tfs tf];
    heights = [heights height];
    v_news = [v_news v_new];
    accels = [accels accel];
    ang_accels = [ang_accels ang_accel];
    omega_news = [omega_news omega_new];
  end

figure
plot(tfs, heights)
xlabel('Time (s)');
ylabel('Height(m)');
title('Height Fallen over Time');
legend('Rocket');

figure
plot(tfs, v_news)
xlabel('Time (s)');
ylabel('Velocity (m/s)');
title('Velocity Along Fall');
legend('Rocket');

figure
plot(tfs, accels)
xlabel('Time (s)');
ylabel('Acceleration (m/s^2)');
title('Rocket Acceleration');
```

```matlab
legend('Rocket');

figure
plot(tfs, ang_accels)
xlabel('Time (s)');
ylabel('Rotor Acceleration (rad/s^2)');
title('Rotor Acceleration');


figure
plot(tfs, omega_news)
xlabel('Time (s)');
ylabel('Rotor Velocity(rad/s)');
title('Rotor Rotational Velocity');


disp(tf)
disp(height)
disp(v_new)
disp(omega_new)
```

Appendix K: Parachute Load Code

```matlab
clear;
clc;
rho = 1.225; %Density of air,
C_d = 0.75;   %Coefficeint of drag for the parachute that is going to
 be put on the Mainbody
A   = 1.19;   %Area of the parachute that is going to be put on the
 Mainbody
g   = 9.81;   %gravity
m   = 3.5;      %mass of the Mainbody
F_g = m*g;    %Force of gravity

t_steps = 0:.01:2;
V_i     = g*5; %Initial velocity of the nosecone when the parachute
 opens.

for i=1:201

    dt = .01;
    F_d(i) = 1/2*rho*C_d*A*V_i(i).^2;
    a(i) = (F_d(i)-F_g)./m;
    V_f(i) = V_i(i)-a(i)*dt;
    V_i(i+1)=V_f(i);

end

figure
plot(t_steps,F_d)
title('Force on Main Body Bulkhead vs Time');
xlabel('Time')
ylabel('Overall Force')
```